Geobacter sulfurreducens microcolony growth and its single bionanowire conductivity
On potential and growth

Blom, C.J.

DOI
10.4233/uuid:aa098c5a-ce99-4426-bc22-8662f4083aab

Publication date
2024

Document Version
Final published version

Citation (APA)
Blom, C. J. (2024). *Geobacter sulfurreducens microcolony growth and its single bionanowire conductivity: On potential and growth*. [Dissertation (TU Delft), Delft University of Technology]. https://doi.org/10.4233/uuid:aa098c5a-ce99-4426-bc22-8662f4083aab

Important note
To cite this publication, please use the final published version (if applicable).
Please check the document version above.

Geobacter sulfurreducens microcolony growth and its single bionanowire conductivity. On potential and growth.

Blom, C.J.

Publication date
2024

Document Version
Final published version

Citation (APA)
Blom, C. J. (2024). *Geobacter sulfurreducens microcolony growth and its single bionanowire conductivity. On potential and growth.* [Dissertation (TU Delft), Delft University of Technology].

Geobacter sulfurreducens microcolony growth and its single bionanowire conductivity.

On potential and growth.

Proefschrift

ter verkrijging van de graad van doctor aan de Technische Universiteit Delft,
op gezag van de Rector Magnificus Prof. dr. ir. T.H.J.J. van der Hagen,
voorzitter van het College voor Promoties,
In het openbaar te verdedigen op
20 juni 2024.

door

Carsten Joram BLOM

Ingenieur in levenswetenschappen,
Technische Universiteit Delft, Nederland,
geboren te Voorburg, Nederland.

Dit proefschrift is goedgekeurd door de promotoren.

Samenstelling promotiecommissie bestaat uit:

Rector magnificus,	voorzitter
Prof. dr. ir. H.S.J. van der Zant	Technische Universiteit Delft, promotor
Dr. ir. L. Laan	Technische Universiteit Delft, promotor

Onafhankelijke leden:

Prof. dr. F.C. Grozema	Technische Universiteit Delft
Prof. dr. Y.M. Blanter	Technische Universiteit Delft
Prof. dr. F.J.R. Meysman	Universiteit Antwerpen
Dr. S.M. Depken	Technische Universiteit Delft

Keywords: microcolony, microscopy, nanowire, conductivity
Printed by: Ipskamp Printing
Cover by: Dr. L.L. Dreesens

ISBN: 978-94-6473-521-5
An electronic copy of this dissertation is available at http://repository.tudelft.nl/

Voor mijn ouders.

SUMMARY

The long-range electron transport of exoelectrogenic bacterium *G. sulfurreducens* was recently discovered to be facilitated by a network of conductive protein wires. In **chapter 1** we provide an overview of our current understanding of these protein wires. This newly discovered feature of the model organism for microbial fuel cells may provide new avenues for optimization of biological power generation.

In particular a characterization of the wires' effect on biofilm formation could provide approaches for increasing biofilm thickness and current density. Peripheral cells may depend more heavily on inner cells' properties than previously thought, since they are required to utilize the inner cells' conductive wires for electron transport to the electron acceptor. Such an effect is expected to be most visible in the early stages of biofilm formation where independent single cells grow to interdependent cells in microcolonies. Studies of early *G. sulfurreducens* microcolony growth are complicated by the toxic effect of oxygen on growth.

In **chapter 2** we describe a method for observing *G. sulfurreducens* early microcolony growth under agar pads. We show the method is able to spatially and temporally describe growth of single *G. sulfurreducens* cells into microcolonies and is able to discern differences between strains with or without wires. However, the significant variation in microcolony surface area between pads showed the method's lack in reproducibility. Future work should focus on maintaining equally anaerobic conditions between pads.

In addition to the potential for improving biological power generation, the poorly understood electron transport mechanism potentially defines a hitherto unknown class of electron transport proteins. Particularly the long range mechanism for efficient biological electron transport remains poorly understood. Some studies support the known mechanism of hopping along cytochromes, yet other studies in cytochrome-denaturing conditions show conductivity is maintained. Complicating full understanding further is the fact that most of these studies use conventional techniques for measuring biological electron transport, which happen to measure in bulk. To model an unknown mechanism of electron transport depends on well-defined systems, such as a single nanowire rather than an entire biofilm.

In **chapter 3** we describe a novel method for making electrical contact with such single nanowires. Using a stochastic deposition method, passive voltage imaging and atomic force microscopy we visually confirm and make electrical contact with single nanowires. We describe optimization of the sample preparation and chip design showing that chemically untreated samples performed best, while an interdigitated chip design improved the chances of making contact. Ultimately we demonstrate the ability to manipulate temperature, providing valuable characterization of the temperature-dependence of nanowires conductivity.

In **chapter 4** we apply this method to characterize the conductive properties of single nanowires. Current-voltage curves showed conductances in orders of magnitudes from 10^{-13} S up to 10^{-6} S. Measurements at varying temperatures identified activation energies from 0.36 eV to 0.41 eV. Arrhenius plots displayed features corresponding to a simple model where electron transport rate was limited by injection barriers as well as a model where electron transport rate is limited by intramolecular hopping. Future modeling is required to fully describe the electron transport.

In **chapter 5** we demonstrate the flexibility of the wire deposition method by mea-

suring another type of conductive biological wire. Cable bacteria are able to facilitate electron transport along their cell membranes across several millimeters. We image successful deposition of cable bacteria bundles and measure their conductance. Current-voltage curves showed conductance in the orders of magnitude from 10^{-10} S to 10^{-7} S. These initial proof-of-principle measurements can be followed up by further characterization of this poorly understood method of long-range biological electron transport.

SAMENVATTING

Het is recent ontdekt dat *G. sulfurreducens* elektronen over lange afstanden transporteert door een netwerk van geleidende eiwitdraden. In **hoofdstuk 1** geven we een overzicht van ons huidige begrip van deze draden. Deze nieuw ontdekte eigenschap van het modelorganisme voor microbiële brandstofcellen kan nieuwe mogelijkheden bieden voor optimalisatie van biologische stroomopwekking.

Met name een karakterisering van het effect van de draden op de biofilmvorming kan opties identificeren voor het vergroten van de biofilmdikte en de stroomdichtheid. Perifere cellen kunnen mogelijk meer afhankelijk zijn van de eigenschappen van de binnenste cellen dan eerder gedacht, omdat ze de geleidende draden van de binnenste cellen moeten gebruiken voor elektronentransport naar de elektronenacceptor. Dit effect wordt verwacht het meest zichtbaar te zijn in de vroege stadia van biofilmvorming, waar onafhankelijke enkele cellen groeien tot onderling afhankelijke cellen in microkolonies. Onderzoek van de vroege groei van *G. sulfurreducens* microkolonies wordt nog bemoeilijkt door het toxische effect van zuurstof op de groei.

In **hoofdstuk 2** beschrijven we een methode om de vroege groei van *G. sulfurreducens* microkolonies onder agar *pads* te observeren. We tonen aan dat de methode in staat is om de groei van enkele *G. sulfurreducens* cellen tot microkolonies spatieel en temporeel te beschrijven en verschillen kan onderscheiden tussen stammen met of zonder draden. Echter, de aanzienlijke variatie in oppervlakte van microkolonies tussen pads toonde het gebrek aan reproduceerbaarheid van de methode aan. Toekomstig werk moet zich richten op het handhaven van gelijkwaardige anaerobe omstandigheden tussen pads.

Naast het potentieel voor verbetering van biologische stroomopwekking, legt het slecht begrepen mechanisme voor elektronentransport mogelijk een tot nu toe onbekende klasse van elektronentransportproteïnen bloot. Met name het mechanisme voor efficiënt biologisch elektronentransport op lange afstand blijft slecht begrepen. Sommige studies ondersteunen het bekende mechanisme van hoppen langs cytochromen, maar andere studies in omstandigheden waarin cytochromen worden gedenatureerd tonen aan dat de geleidbaarheid behouden blijft. Verdere complicaties voor het volledige begrip zijn het feit dat de meeste van deze studies conventionele technieken gebruiken voor het meten van biologisch elektronentransport, die voornamelijk in bulk meten. Om een onbekend mechanisme van elektronentransport te modelleren is een gedefinieerd systeem van belang, zoals een enkele nanodraad in plaats van een hele biofilm.

In **hoofdstuk 3** beschrijven we een nieuwe methode om elektrisch contact te maken met dergelijke enkele nanodraden. Met behulp van een stochastische depositiemethode, passieve spanningsbeeldvorming en atomaire krachtmicroscopie bevestigen we visueel de aanwezigheid van enkele nanodraden en maken we elektrisch contact daarmee. We beschrijven de optimalisatie van de monster bereiding waarbij onbehandelde monsters het beste presteerden. Een chipontwerp gebaseerd op in elkaar grijpende vingers verbeterde de kans op contact. Uiteindelijk demonstreren we de mogelijkheid om de temperatuur te manipuleren. Dit levert waardevolle karakterisering van de temperatuur afhankelijkheid van geleidbaarheid op.

In **hoofdstuk 4** passen we deze methode toe om de geleidende eigenschappen van enkele nanodraden te karakteriseren. Stroom-spanningscurves toonden geleidbaarheden in grootteordes van 10^{-13} S tot 10^{-6} S. Metingen bij verschillende temperaturen

identificeerden activeringsenergieën van 0,36 eV tot 0,41 eV. Arrhenius-plots vertoonden kenmerken die overeenkomen met een eenvoudig model waarbij de snelheid van elektronentransport beperkt werd door injectiebarrières, evenals een model waarbij de snelheid van elektronentransport beperkt werd door intramoleculair hoppen. Verdere modellering is vereist om het elektronentransport volledig te beschrijven.

In **hoofdstuk 5** demonstreren we de flexibiliteit van de draaddepositiemethode door een ander type geleidende biologische draad te meten. Kabelbacteriën zijn in staat om elektronentransport langs hun celmembranen over meerdere millimeters te vergemakkelijken. We visualiseren de succesvolle depositie van bundels kabelbacteriën en meten hun geleidbaarheid. Stroom-spanningscurves toonden geleidbaarheid in grootteordes van 10^{-10} S tot 10^{-7} S. Deze initiële *proof-of-principle* metingen kunnen opgevolgd worden voor verdere karakterisering van dit andere slecht begrepen mechanisme van biologisch elektronentransport over lange afstand.

CONTENTS

1

INTRODUCTION

G. sulfurreducens *uses conductive protein nanowires to make electrical contact with extracellular insoluble electron acceptors. Electron transport through these nanowires is poorly understood. Further characterization of electron transport depends on current-voltage measurements of single wires at varying temperatures. The effect of wire conductivity on growth has been explored in bulk or full biofilms, its effect on early microcolony growth is unknown. This thesis describes a method for measuring single wire conductivity as well as a method for measuring early microcolony growth.*

1

1.1 ELECTRONS AND LIFE

Biological electron transport is fundamental to life as we know it. Both respiration and photosynthesis, nature's two main energy-capturing mechanisms, depend on the transport of electrons. Both processes enable efficient capturing of chemical energy by facilitating electron transfer from a high electrochemical potential to a low electrochemical potential ("potential" in short). An electron in a state with high potential tends to move towards a state with a lower potential when given the option. However, in order to do so it must transfer the difference in energy to something else, a fact that organisms readily utilize by capturing that energy in chemical bonds. In principle any pair of high and low potential states can be used by organisms. The only prerequisite is that both states occur in physiologically relevant conditions and that the unfacilitated transition rate in those conditions is relatively low. Organisms can then facilitate transition through a series of proteins capturing chemical energy in the process. Typically it is captured in the form of a covalent bond between phosphate and adenosinediphosphate (ADP) resulting in adenosinetriphosphate (ATP). ATP is the predominant biological short term energy storage molecule, upon dephosphorylation to ADP the chemical energy can be transferred to whatever metabolic reaction is required.

Non-photosynthetic organisms use pairs of molecules called electron donors and acceptors for energy capture. Electron donors are molecules of which electrons are in a state of higher potential than states available in the electron acceptor. Organisms can use a variety of electron donors and electron acceptors, micro-organisms in particular use a variety of electron acceptors. For humans the electron donors are a variety of sugars, while the electron acceptor is only one type of molecule: oxygen. Despite the variety of electron donors, one central series of proteins is used to transfer the energy of the potential difference to chemical energy. Regardless of the type of sugar we consume, our metabolism ensures that electrons are transferred from the sugar to a flavin molecule of slightly lower potential, either NADH or FADH. Those flavins then serve as the intermediate electron donor for a series of membrane-embedded proteins which facilitate electron transfer to the terminal electron acceptor, called the electron transport chain.

1.2 ELECTRON TRANSFER IN PROTEINS

The membrane proteins of the electron transport chain couple electron transport to proton translocation, resulting in a potential gradient build-up across the membrane. The potential gradient is subsequently utilized to phosporylate ADP to ATP. The electron and proton translocation are physically coupled due to the relevant proteins' structure.

The proteins in the electron transport chain consist mostly of proteins called cytochromes that contain metal ions (typically cations of Fe or Cu) fixed in a porphyrin ring, which together is called a heme group. The protein structure ensures that the metal ions are at slightly descending potential in the functional direction of electron transport.

Although the metal ions are in a decreasing series of potential electrons still need to overcome the space in between them, described by overcoming a potential barrier. In order to overcome the barrier the electrons will have to tunnel through or hop across the barrier to the next metal ion[1]. Hopping is an electron transport mechanism in which the electron coincidentally gains enough energy from the environment to overcome a

potential barrier, allowing it to transfer to the metal ion of lower potential. In contrast, tunneling is a process where the electron does not gain enough energy to overcome the potential barrier. Instead, due to overlap of the electrons wave function with another state of equal potential on the other side of the barrier it still has a certain probability to enter that state on the other metal ion, after which it might transfer energy to the environment, dropping to the state of lower potential.

As the electron moves towards states of lower potential, the resulting potential difference is used to facilitate the translocation of protons by the cytochrome[2]. Upon reduction of the initial metal ion, the cytochrome binds a proton on one side of the membrane. The directional movement of negative charge throughout the cytochrome either results in conformational shifts that physically translocate the protons or causes a series of protonation and deprotonation steps[3,4], both ultimately resulting in net transfer of protons to the other side of the membrane[2]. The series of cytochromes each facilitate translocation of protons via the transport of electrons. At each step a part of the energy associated with the remaining potential difference between the electron and the electron acceptor is transferred to the build-up of potential gradient[5], up to the point where there is little potential difference between electron and electron acceptor, and the electron is finally allowed to transfer to the electron acceptor.

The build-up of potential gradient caused by transfer of the protons is allowed to discharge via proton translocation through ATP-synthase, a protein with a waterwheel-like structure that ensures proton translocation is coupled to ADP phosphorylation[6]. The net result of electron transport, proton translocation, and potential gradient discharge is then the phosphorylation of ADP to ATP.

Our need for nearly constant access to our terminal electron acceptor shows how fundamental electron transport and electron acceptors are to life.

1.3 ELECTRONS OUTSIDE

Many organisms, like us, are able to import or allow access to the electron donor and acceptor into their cells, where the cytochromes embedded in the cell or organelle membrane ensure the transfer of electrons from one to the other. However, especially among anaerobic organisms, it may not be possible for an organism to import the terminal electron acceptor, requiring electron transport outside of the cell.

A model organism for these 'exoelectrogenic' bacteria is *Geobacter sulfurreducens*[7–9], a bacterium capable of using metal oxide particles[10] (here named 'iron particles' in short) and electrodes[11] as electron acceptors. When in direct contact with iron particles or electrodes, a *G. sulfurreducens* cell is capable of transferring electrons from the inside of the cell across the membranes to the outside through a series of membrane-embedded metal-ion containing proteins called cytochromes[9]. A reduced cytochrome in the outer membranes is then able to reduce the electron acceptor, completing the electron transport chain.

In order to grow biofilms thicker than a monolayer, a long-range electron transport mechanism is needed. Other exoelectrogenic bacterial species are known to achieve long-range electron transport through export of intermediate electron acceptors ('shuttles'). These intermediate electron acceptors diffuse and a fraction is oxidized upon contact with the electron acceptor[12]. Through diffusion of the intermediate electron accep-

tors back to the cell the process can repeat itself. *G. sulfurreducens* was shown not to depend on diffusion for its long-range electron transport[13], instead, *G. sulfurreducens* produces two types of conductive protein wires[14,15], although in early research these two types were thought to be only one type of wire since the second type was discovered only recently[15].

The first type of wire are called pili, which are a polymer of a 60 amino acid non-cytochrome monomer[14] which assembles into a helical pattern with several helices forming one wire as can be seen in figure 1.2a. Pili are typically used by bacteria for attachment and although cytochromes are known to be attached to the pili, the distance between them is more than 10 nm, severely limiting electron transport through hopping between cytochromes[16]. This type of wire was first considered to be the only type of wire present. Electron transport along the pili would have to occur either via hopping along an other type of redox site than heme groups, or by a different mechanism. The helical arrangement of closely-spaced aromatic amino acids as depicted by yellow groups in figure 1.2a might allow for electron delocalization to some extent, and thus might contribute to this mechanism. A role of aromatic amino acids in conductivity is supported by a study by Vargas *et al.*[16] showing a decrease in conductivity, iron reduction and current generation for a mutant in which the aromatic amino acids of pilA were replaced with alanine (figure 1.1).

The second type of wire are cytochrome wires consisting of stacked cytochromes[15] . Currently two cytochrome wires are identified, one consisting of OmcS[17] and the other of OmcZ[18] monomers, but the wire structures are similar. In figure 1.2b the heme groups in the OmcS wire are shown to be closely-spaced series. This series of cytochromes could allow for hopping similar to *S. oneidensis* wires albeit in a different form, namely an extracellular polymer rather than a membrane protrusion. The later discovery of these wires is in part due to the similar dimensions, with the pili being around 3 nm wide and the cytochrome wires around 4 nm wide, both micrometers-long. As such, a visual confirmation of wire presence via for example AFM provides no confirmation of wire identity. Since early studies, as well as ours, mostly relied on this visual confirmation it is often unclear which type was studied, including early conductivity measurements.

At first glance, the cytochrome wires seem a more likely candidate for high conductivity due to the series of redox sites known to be effective for long-range electron transport. However, even in cytochrome denaturing conditions, such as pH 4 or added β-mercaptoethanol[19,20], *G. sulfurreducens* wires were shown to remain conductive. If the cytochrome wires were indeed denatured, then the only wires left to conduct are the pili. Additionally, studies modifying the gene corresponding to the pili monomer protein (pilA) observed significant changes in conductivity of biofilms and wires[21]. As such, conductivity of pili can not be excluded, and its mechanism for long-range electron transport without heme groups remains unclear. In this thesis, as well as in early investigations, the wire identity (cytochrome stack or pilum) is often unconfirmed. We will use "wire" to refer to such cases and "pili" for cases where the wire is known to be a pilum.

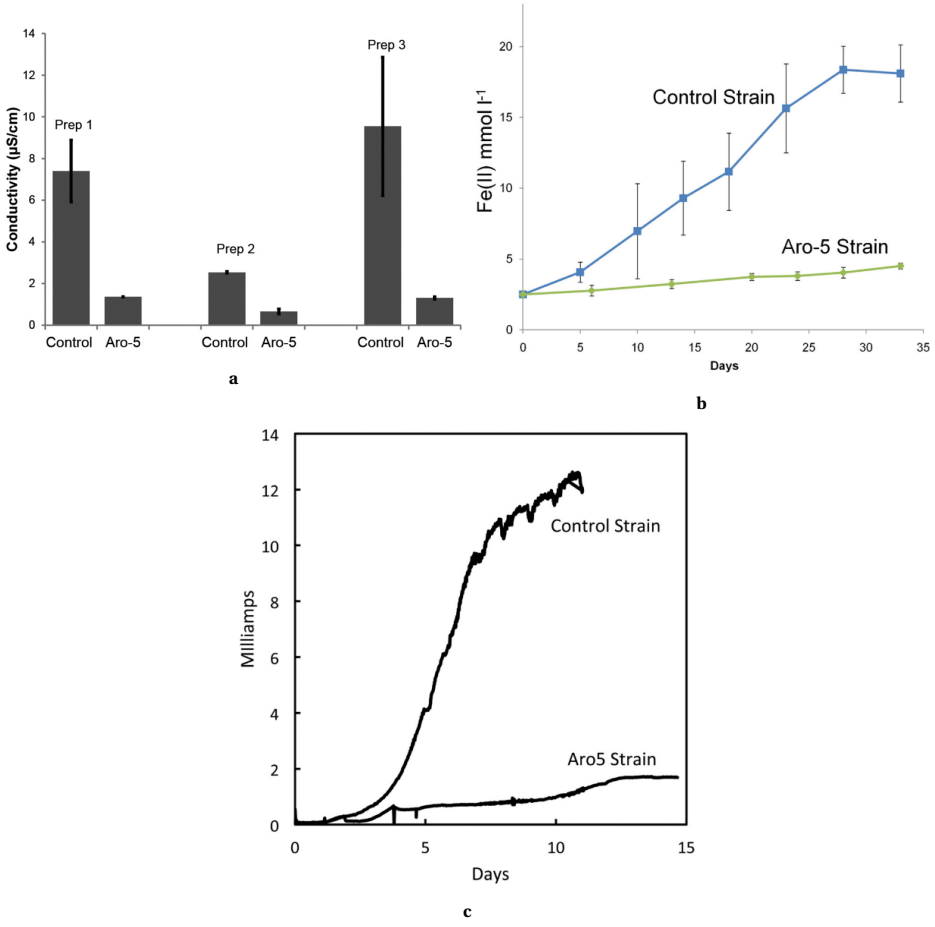

Figure 1.1: Conductivity (**a**) of filament preparations, iron reduction (**b**) and current production (**c**) of cultures of a mutant *G. sulfurreducens* strain (Aro-5) in which the pili were genetically modified by replacing codons for aromatic amino acids with codons for alanine, called Aro-5, compared to the wildtype ("Control Strain"), as reported by Vargas *et al.*[16]. The Aro-5 strain produces pili with lower conductivity within one order of magnitude, and cultures have lower iron reduction and current production rates.

1

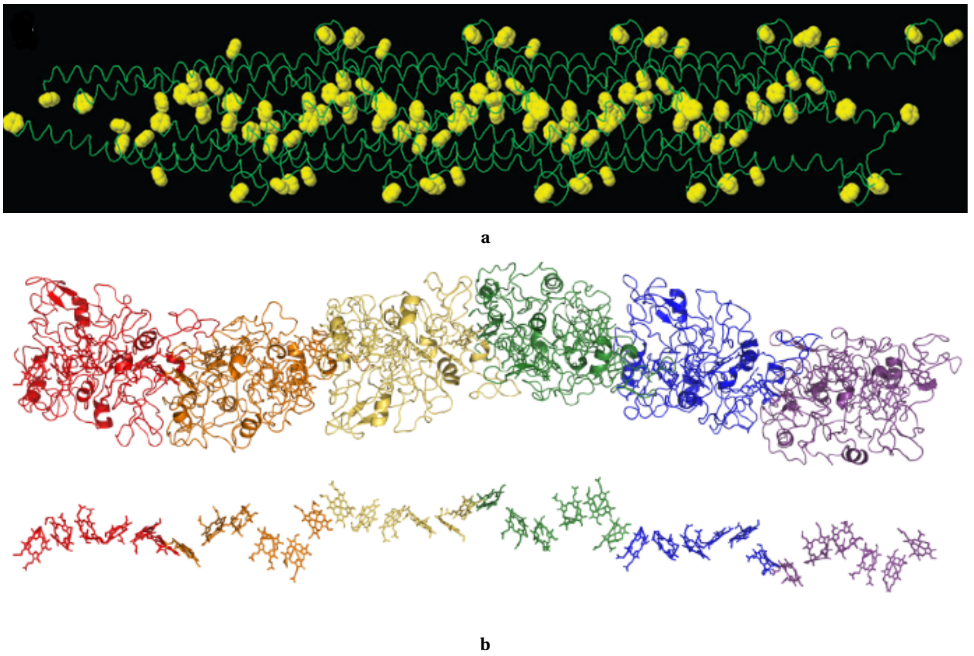

Figure 1.2: a) Predicted structure of a wire consisting of *G. sulfurreducens* pilA monomers based on NMR structure as reported by Malvankar *et al.* [22]. Aromatic amino acids are indicated in yellow. There are no heme groups present. The helical structure results in alignment of aromatic amino acids, typically with a distance between 3 to 4 angström between them. **b)** Structure based on cryo-electron microscopy of non-pili *G. sulfurreducens* wires, matching a series of stacked OmcS cytochromes, as reported by Filman *et al.* [15]. The heme group stacking is indicated on the bottom, with typical heme to heme distances between 3 to 4 angstrom.

1.4 COOPERATIVE CONDUCTIVITY.

The wires are the means for individual cells to access an insoluble electron acceptor over several micrometer. An effect of lowered conductivity on growth is surprising since the conductivity of only a single wire is more than required for a single cell to export its electrons. The wires possess conductivities up to 0.67 S/cm reported in this thesis. While cells have dozens of pili in addition to cytochrome wires, this means even a single conductive wire is able to conduct currents 100 times larger than those required for a single cell to grow[13]. Despite the "excess" conductivity for single cells a decrease in conductivity still has negative effects on population growth.

If the conductivity is higher than required for survival of a single cell but still affects growth, it may be due to a role in supporting growth of more than one cell. In a biofilm growing on an electrode the cells closest to the electrode need to conduct current of the entire biofilm, not just themselves.

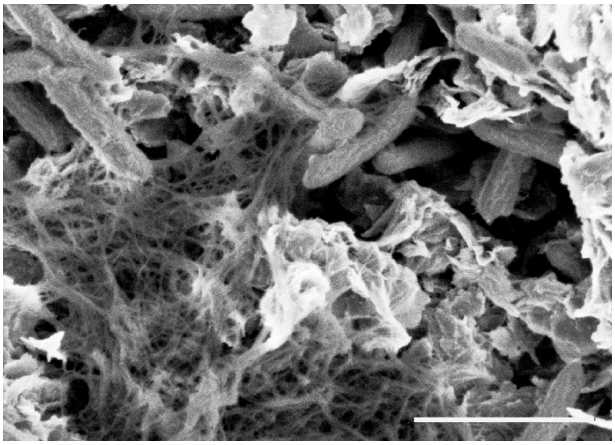

Figure 1.3: SEM image of *G. sulfurreducens* biofilms fixed with cationic dye safranin O grown on unpoised graphite electrodes, adapted from Rollefson *et al.*[23]. *G. sulfurreducens* form an extracellular network structure including pili filaments.

The production of an extracellular resource open for use by others implicates a level of cooperation of a species. Species utilizing shuttles for the final step in their metabolism are indirectly metabolically coupled through diffusion. The wires instead couple the oxidation states of cytochromes of one cell directly to another, and allow direct electron transfer between the two. Through a coupling of metabolic states, the cells' survival may become coupled as well, resulting in cooperation.

For cooperative traits to persist, they must be subject to selection pressures minimizing the fitness benefits of mutations resulting in a 'cheater' phenotype, i.e. a cell gaining the benefits from the cooperative trait without paying the cost. Such a cheater may be a cell producing very few wires, expending little energy on protein production and assembly while still being able to employ the other's wire network allowing long-range electron transport. Alternatively, the wire's conductive properties may allow cells to tune their level of cooperation. For example, wires with low iron-to-wire but high wire-to-wire con-

tact resistance would allow cells to export electrons to iron without allowing other cells to effectively employ that same wire. In either case, if the wire conductivity is shown to be crucial for group growth moreso than individual growth, its conductive properties must also be interpreted in the context of a cooperative trait. In that case conductivity may be expected to have little effect on single cell growth, but with increasing population size the conductivity may become a limitation on population growth.

Investigation of the transition from single cell to microcolony, and its dependence on high conductivity, can grant insight into the role of conductivity in *G. sulfurreducens* cell-to-cell dependency. If microcolony growth depends on the conductivity of wires it would highlight a hereto unexplored aspect of microcolony and ultimately biofilm ecology: the intercellular conductive network.

Previous studies of biofilm formation have been performed in bulk, or using confocal microscopy to investigate entire biofilms[24–28], one example of which is shown in figure 1.4. These studies have shown that the wires have a structural as well as conductive role in biofilm formation, but provide little insight in the transition from individual cells to microcolonies.

For a different species of bacteria called cable bacteria the cooperative nature of conductive protein fibres is clearer. These cable bacteria form centimeter long filaments with conductive protein fibres spanning the entire filament[29]. These fibres would provide little benefit to a separated individual but great benefit to an individual part of the filamentous group. Perhaps similarly to the *G. sulfurreducens* wires, the properties of these fibres may be tuned to their cooperative role. Given their different lifecycle the fibres may be tuned for fidelity rather than optimal conductivity in order to maintain a constant electrical connection across centimeters.

The characterization and comparison of the electronic properties of both *G. sulfurreducens* wires and cable bacteria fibres may provide insight into the connection between protein wire conductivity and cooperation. Alternatively, if the wires are already optimized for use in a network, they may provide avenues for designing and engineering bionanoelectrical circuits in the future. Within this context of possibly cooperative conductivity we describe in this thesis a method allowing the investigation of conductivity of both *G. sulfurreducens* and cable bacteria biological wires, as well as a method for investigating the role of *G. sulfurreducens* wire conductivity in individual versus group growth.

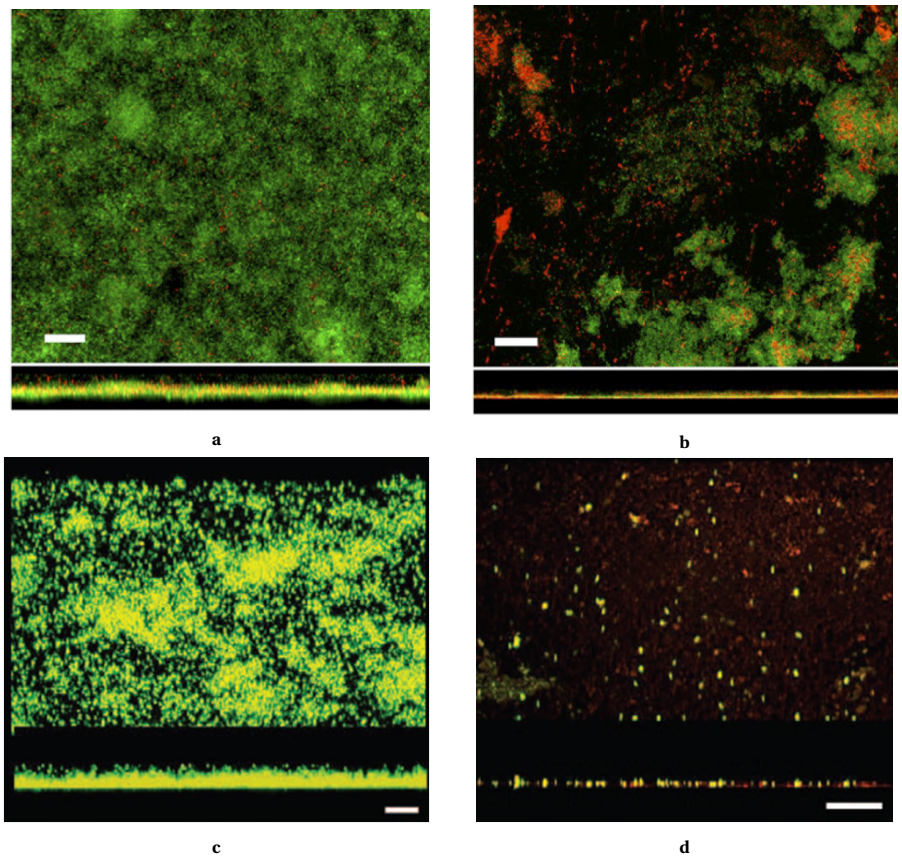

Figure 1.4: Confocal Laser Scanning Micrographs (CLSM) of biofilms grown with carbon source (**a**) or without (**b**) as reported by Speers and Reguera [27], and with an electron acceptor (**c**) or without (**d**), as reported by Reguera *et al.* [24]. Cells are stained with BacLight viability dyes with green indicating live cells and red indicating dead cells. Micrographs consist of a top view (center) and projections in x (on the bottom), scale bars equal 20 µm. Current biofilm growth studies predominantly use CLSM on anode biofilms at fixed timepoints for imaging growth. Despite a lack of carbon source or electron acceptor, slight microcolony growth is still visible in **b** and **d**.

1

1.5 IN THIS THESIS

In this thesis we will lay the necessary groundwork for future investigation of any cooperative role of conductivity. First, we need to be able to identify and then characterize whether conductivity affects growth as an individual cell different from growth as a group. We will specifically describe a method for the model organism *G. sulfurreducens* .

Ideally, we would like to be able to follow the growth process from individual to microcolony in an environment where growth is most likely to depend on conductivity. For distinguishing individual growth from group growth a microscopical approach is required, while following growth from an individual to a microcolony requires imaging the same location throughout time. The growth process of a single cell to a microcolony can be followed at a magnification of 40x.

Additionally, an environment where growth is most likely to depend on conductivity requires growth on either iron particles or electrodes. We would like to gain insight into the natural role of wires in cooperation and therefore will focus on growth on iron particles. In **chapter 2** we describe a method incorporating each of these features which can be applied to study individual-to-microcolony growth in the future, as well as some preliminary findings and recommended improvements.

Second, to investigate the relationship between electronic properties and the role of the conductive protein we need to be able to characterize the electronic properties. For a thorough characterization of the electronic properties the ability to determine bias-dependence and temperature-dependence of conductivity can help discriminate between various models for the electron transport mechanism. In particular, making electrical contact with a single conductive wire requires deposition on a chip optimized for successful electrical connections and confirmation of connection identity (i.e. confirming the electrical contact is due to the wire). In **chapter 3** we describe a method for contacting *G. sulfurreducens* wires, visually confirming the topological identity of the connecting element using Passive Voltage Contrast imaging and Atomic Force Microscopy, and allowing characterization of temperature and bias-dependence, which could be expanded in the future to enable four-probe measurements. In **chapter 4** we apply this method to characterize the electronic properties of single *G. sulfurreducens* wires, a few micrometers long and nanometers wide, and describe a simple model for an electron transport mechanism.

Finally, in **chapter 5** we show the flexibility of the described method enabling investigations of other biologically conductive wires by applying it to the centimeters long and micrometers wide cable bacteria.

Overall this thesis presents two methods, one for investigation of early microcolony growth, the other for investigation of the wires responsible for conductivity, and presents preliminary findings for both. Although currently the main focus in reported studies tends towards the electron transport mechanism of *G. sulfurreducens* wires, future interest may shift to other biowires, engineering biowires or studying the emerging network properties once the electron transport mechanism for the single wires has been elucidated. Here we provide the techniques to study a variety of those biowires as well as the ecological implications of conductivity, which in turn will allow for better understanding of the wire properties and potentially enable an evolutionary engineering approach to wire or network optimization.

REFERENCES

[1] M. W. Gray, J. Lukeš, and J. M. Archibald, *Irremediable complexity?* Science **330**, 920 (2010).

[2] J. E. Walker, *The Nadh: Ubiquinone oxidoreductase (complex I) of respiratory chains,* Quarterly Reviews of Biophysics **25**, 253 (1992).

[3] L. A. Sazanov, *A giant molecular proton pump: Structure and mechanism of respiratory complex I,* Nature Reviews Molecular Cell Biology **16**, 375 (2015).

[4] A. A. Mamedova, P. J. Holt, J. Carroll, and L. A. Sazanov, *Substrate-induced conformational change in bacterial complex I,* Journal of Biological Chemistry **279**, 23830 (2004).

[5] P. Hinchliffe and L. A. Sazanov, *Biochemistry: Organization of iron-sulfur clusters in respiratory complex I,* Science **309**, 771 (2005).

[6] I. N. Watt, M. G. Montgomery, M. J. Runswick, A. G. Leslie, and J. E. Walker, *Bioenergetic cost of making an adenosine triphosphate molecule in animal mitochondria,* Proceedings of the National Academy of Sciences of the United States of America **107**, 16823 (2010).

[7] S. Ishii, T. Shimoyama, Y. Hotta, and K. Watanabe, *Characterization of a filamentous biofilm community established in a cellulose-fed microbial fuel cell.* BMC microbiology **8**, 6 (2008).

[8] H. Yi, K. P. Nevin, B.-C. Kim, A. E. Franks, A. Klimes, L. M. Tender, and D. R. Lovley, *Selection of a variant of Geobacter sulfurreducens with enhanced capacity for current production in microbial fuel cells.* Biosensors & bioelectronics **24**, 3498 (2009).

[9] D. R. Lovley, *Bug juice: harvesting electricity with microorganisms.* Nature reviews. Microbiology **4**, 497 (2006).

[10] F. Caccavo, D. J. Lonergan, D. R. Lovley, M. Davis, J. F. Stolz, and M. J. Mcinerneyl, *Geobacter sulfurreducens sp. nov., a Hydrogen- and Acetate- Oxidizing Dissimilatory Metal-Reducing Microorganism,* Applied and environmental microbiology **60**, 3752 (1994).

[11] D. R. Bond and D. R. Lovley, *Electricity Production by Geobacter sulfurreducens Attached to Electrodes,* Applied and environmental microbiology **69**, 1548 (2003).

[12] K. Dolch, J. Danzer, T. Kabbeck, B. Bierer, J. Erben, A. H. Förster, J. Maisch, P. Nick, S. Kerzenmacher, and J. Gescher, *Characterization of microbial current production as a function of microbe-electrode-interaction.* Bioresource technology **157**, 284 (2014).

[13] X. Jiang, J. Hu, E. R. Petersen, L. a. Fitzgerald, C. S. Jackan, A. M. Lieber, B. R. Ringeisen, C. M. Lieber, and J. C. Biffinger, *Probing single- to multi-cell level charge transport in Geobacter sulfurreducens DL-1.* Nature communications **4**, 2751 (2013).

[14] P. N. Reardon and K. T. Mueller, *Structure of the Type IVa Major Pilin from the Electrically Conductive Bacterial Nanowires of Geobacter sulfurreducens.* The Journal of biological chemistry **288**, 29260 (2013).

[15] D. Filman, S. Marino, J. Ward, L. Yang, Z. Mester, E. Bullitt, D. Lovley, and M. Strauss, *Structure of a cytochrome-based bacterial nanowire,* bioRxiv , 492645 (2018).

[16] M. Vargas, N. S. Malvankar, P.-l. Tremblay, C. Leang, J. A. Smith, and P. Patel, *Aromatic Amino Acids Required for Pili Conductivity and Long- Range Extracellular Electron Transport in Geobacter sulfurreducens,* mBio **4**, 1 (2013).

[17] F. Wang, Y. Gu, J. P. O'Brien, S. M. Yi, S. E. Yalcin, V. Srikanth, C. Shen, D. Vu, N. L. Ing, A. I. Hochbaum, E. H. Egelman, and N. S. Malvankar, *Structure of Microbial Nanowires Reveals Stacked Hemes that Transport Electrons over Micrometers,* Cell **177**, 361 (2019).

[18] S. E. Yalcin, J. P. O'Brien, Y. Gu, K. Reiss, S. M. Yi, R. Jain, V. Srikanth, P. J. Dahl, W. Huynh, D. Vu, A. Acharya, S. Chaudhuri, T. Varga, V. S. Batista, and N. S. Malvankar, *Electric field stimulates production of highly conductive microbial OmcZ nanowires,* Nature Chemical Biology **16** (2020), 10.1038/s41589-020-0623-9.

[19] N. L. Ing, T. D. Nusca, and A. I. Hochbaum, *Geobacter sulfurreducens pili support ohmic electronic conduction in aqueous solution,* Physical Chemistry Chemical Physics **19**, 21791 (2017).

[20] N. S. Malvankar, M. T. Tuominen, and D. R. Lovley, *Biofilm conductivity is a decisive variable for high-current-density Geobacter sulfurreducens microbial fuel cells,* Energy & Environmental Science **5**, 5790 (2012).

[21] D. R. Lovley and D. J. Walker, *Geobacter Protein Nanowires,* Frontiers in Microbiology **10** (2019), 10.3389/fmicb.2019.02078.

[22] N. S. Malvankar, M. Vargas, K. Nevin, P.-l. Tremblay, K. Evans-lutterodt, and D. Nykypanchuk, *Structural Basis for Metallic-Like Conductivity in Microbial Nanowires,* mBio **6**, 1 (2015).

[23] J. B. Rollefson, C. E. Levar, and D. R. Bond, *Identification of genes involved in biofilm formation and respiration via mini-Himar transposon mutagenesis of Geobacter sulfurreducens.* Journal of bacteriology **191**, 4207 (2009).

[24] G. Reguera, R. B. Pollina, J. S. Nicoll, and D. R. Lovley, *Possible nonconductive role of Geobacter sulfurreducens pilus nanowires in biofilm formation.* Journal of bacteriology **189**, 2125 (2007).

[25] G. Reguera, K. P. Nevin, J. S. Nicoll, S. F. Covalla, T. L. Woodard, and D. R. Lovley, *Biofilm and nanowire production leads to increased current in Geobacter sulfurreducens fuel cells.* Applied and environmental microbiology **72**, 7345 (2006).

[26] Y. Tan, R. Y. Adhikari, N. S. Malvankar, J. E. Ward, K. P. Nevin, T. L. Woodard, J. A. Smith, O. L. Snoeyenbos-West, A. E. Franks, M. T. Tuominen, and D. R. Lovley, *The low conductivity of Geobacter uraniireducens pili suggests a diversity of extracellular electron transfer mechanisms in the genus geobacter,* Frontiers in Microbiology **7**, 1 (2016).

[27] A. M. Speers and G. Reguera, *Electron donors supporting growth and electroactivity of Geobacter sulfurreducens anode biofilms.* Applied and environmental microbiology **78**, 437 (2012).

[28] L. V. Richter, S. J. Sandler, and R. M. Weis, *Two isoforms of Geobacter sulfurreducens PilA have distinct roles in pilus biogenesis, cytochrome localization, extracellular electron transfer, and biofilm formation.* Journal of bacteriology **194**, 2551 (2012).

[29] F. J. Meysman, R. Cornelissen, S. Trashin, R. Bonné, S. H. Martinez, J. van der Veen, C. J. Blom, C. Karman, J. L. Hou, R. T. Eachambadi, J. S. Geelhoed, K. D. Wael, H. J. Beaumont, B. Cleuren, R. Valcke, H. S. van der Zant, H. T. Boschker, and J. V. Manca, *A highly conductive fibre network enables centimetre-scale electron transport in multicellular cable bacteria,* Nature Communications **10**, 1 (2019).

2

VISUALIZING MICROCOLONY GROWTH ON IRON PARTICLES

We describe a method for observing G. sulfurreducens*early microcolony growth under agar pads. We show the method is able to spatially and temporally describe growth of single* G. sulfurreducens*cells into microcolonies and is able to discern differences between strains with or without wires. However, the significant variation in microcolony surface area between pads showed the method's lack in reproducibility. Future work should focus on maintaining equally anaerobic conditions between pads.*

2.1 INTRODUCTION

Geobacter sulfurreducens, an exoelectrogenic bacterium model organism, is utilized in Microbial Fuel Cells (MFCs) to convert chemical potential into electrical energy. This conversion occurs through the metabolic coupling of acetate or succinate oxidation to the reduction of an electrode or iron. MFCs contribute to a bio-based economy by using plant waste for electricity generation [1], producing hydrogen from starch [2], or enabling in-situ power generation for marine monitoring equipment [3]. The power generation of the biofilm in MFCs partly limits their applicability. Research to enhance MFC performance has primarily focused on physicochemical aspects like electrolytes or fuel cell architecture, neglecting microbiological or ecological aspects of biofilms [4]. However, in 2010 the electron transport crucial for MFC performance was found to rely on protein wires, a previously unknown method for biological electron transport [5]. Exploring the properties of these wires and their impact on biofilm conductance might unveil new opportunities for MFC improvement.

The protein wires produced by *G. sulfurreducens* enable a conductive network that facilitates the necessary long-range electron transport from cells to the electrode [6]. A single such wire has a conductance exceeding the requisites for an individual single cell's current generation chapter 4. In early colonisation the metabolic flux of cells in microcolonies consisting of a few cells (early microcolony growth) may thus be independent of wire properties. However, as the microcolonies grow to multiple layers of cells (late microcolony growth) the peripheral cells also utilize the wire network of the inner cells for electrical contact to the electrode. These peripheral cells may experience decreased conductance due to a larger number of contact resistances between wires as well as the negative length-dependency of conductance associated with each electron transport mechanism.

The discovery of the protein wires raises questions about their impact on the microecological processes underpinning the growth of the biofilm. Biofilm thickness correlates with current density [7], if biofilm formation in turn depends on wire conductivity, the power generation of the MFC may depend on the protein wires. As peripheral cells increasingly depend on wires for metabolism a critically low conductance could limit metabolic flux, hindering their growth and division. This dependence of peripheral cells on inner cell wires may result in reduced surface area of microcolonies and changes in colony morphology. Microcolonies with high wire dependence may grow along the electron acceptor resulting in a lower mean distance from the electron acceptor. A lower mean cell distance from the electron acceptor would exhibit itself as a thinner biofilm on the electrode with adverse effects on MFC power generation.

Whether peripheral cell growth is truly dependent on wire properties is yet unexplored. Deeper understanding of the microecological impact of wire networks on microcolony growth may provide new avenues for MFC optimilisation. We can investigate wire dependency by examining microcolony morphology, particularly elongation, on an insoluble electron acceptor. In our study, we used amorphous iron oxyhydroxide particles ("iron particles") to mimic *G. sulfurreducens*' natural insoluble electron acceptor. Comparing the dynamics of colony morphology for the wild type and a strain lacking wires may reveal wire dependence. However, that would be insufficient to confirm that any observed wire dependence is due to their conductivity. In addition to conductance,

wires may affect microcolony growth through their role in adhesion.

In *G. sulfurreducens* two types of wires are present in the wire network: cytochrome wires[8] and pili lacking cytochromes[9]. Pili are used by other bacterial species to facilitate surface attachment or movement[10]. The pili of *G. sulfurreducens* are different since they lack a globular head[11] but still play a role in attachment[12]. The pili thus contribute to adhesion as well as conductivity of the wire network. The conductive network may depend on pili for their own supposed conductivity or as a scaffolding for conductive cytochrome wires[13]. The expected elongation described above may occur due to the pili's effect on conductance but may also result from their effect on adhesion. Duvernoy et al. showed that elongation of microcolonies of *Escherichia coli* and *Pseudomonas aerigunosa* grown under soft agarose pads depends on adhesion forces[14]. Their microcolonies first elongated due to cell-to-cell adhesion but ultimately attained an isotropic shape due to the increased forces of pad compression and cell-to-surface adhesion. To account for the effect of pili adhesion on colony formation we compare the dynamics of colony morphology between the wild type and a strain producing pili with lower conductivity[15]. In order to do so we must first be able to observe microcolony growth.

Other studies of microcolony morphology utilized agar pads to microscopically observe 2D growth[16]. Yet at time of research (2013) no method was reported specifically for observing 2D microcolony growth on iron particles of *G. sulfurreducens* from single cells up to multilayered colonies. Ultimately, we set up our own method which will be the focus of this chapter. The method needs to provide the following: Microscopic observation and spatial characterization of 2D growth of *G. sulfurreducens* single cells over a time period long enough for multilayered colonies to form on iron particles in an environment with minimal oxygen. Practically speaking, the minimal oxygen proves the greatest challenge.

To study wire dependence optimally the method should minimize the availability of oxygen as alternative electron acceptor. Although *G. sulfurreducens* is considered an anaerobic organism, Lin *et al.*[17] showed that they are able to utilize oxygen as electron acceptor at concentrations below 5 % and Engel *et al.*[18] reported that growth rates on low concentrations of fumarate (4 mM) supplemented with 3 % oxygen were higher than without oxygen. Since no long-range electron transport or adhesion is required for use of oxygen the growth of *G. sulfurreducens* on oxygen is unlikely to be wire dependent. As such any wire dependence would only be detectable if growth depends predominantly on iron particles as the main electron acceptor. Typically oxygen scavengers such as dithionite are used to remove oxygen from solution. Unfortunately, the use of oxygen scavengers also fully reduces iron particles to their soluble form. Instead we adapted a method described by Fievet *et al.*[19] in 2015, which utilized a gas flow to maintain an anaerobic environment for agar pads.

We have adapted this method of Fievet *et al.*[19] to provide for minimal oxygen conditions suited for studying wire dependence of microcolony growth. They used a custom transparent lid and coverslip to seal the agar pads. Bolts then sealed them to a metal microscope tray and the lid was connected to tubing via gaskets. Oxygen-free gas was flushed through the chamber, ensuring the anaerobic environment. The experiments were reported to last up to 700 minutes, which is shorter than the time required for observing early to late microcolony growth. Additionally, experiment times longer than

700 minutes result in desiccation of the pad due to the low humidity of the gas flow. Upon longer desiccation the agar pads deform and release from the glass making further microscopic observation impossible. Therefore we adapted this method by using a humidified flow setup to maintain a humid anaerobic environment. For observation the pad's flow chamber was temporarily sealed to be transferred to the microscope. The flow setup and transfer process were checked to see if they maintained a microaerobic or anaerobic environment.

To check whether minimal oxygen concentrations were maintained throughout this process we needed a microscopic method for measuring oxygen concentrations in agar pads. Fievet *et al.*[19] used the fluorescence of GFP which at oxygen concentrations lower than 0.025 ppm does not fluoresce, corresponding to 0.067% oxygen in a gas mixture with a temperature of 30 °C. Cells producing GFP were grown in the chamber, with fluorescence only visible in their aerobic conditions. A similar control could be performed in our setup using the *G. sulfurreducens* strain producing GFP reported in Franks *et al.*[20]. However, oxygen consumption by the cells would influence accuracy of the method. Instead we adapted a fluorometric assay of oxygen concentration in solution using (2,2'-bipyridine) dichlororuthenium(II) ($Ru(bpy)_3Cl_2$). In solution ($Ru(bpy)_3Cl_2$) disassociates to $Ru(bpy)_3^{2+}$ and Cl^{-2}.

We first used $Ru(bpy)_3^{2+}$ as a method for fluorometric determination of oxygen concentrations in liquids, then corrected the method for use in agar pads. $Ru(bpy)_3^{2+}$ is a fluorescent compound with an excitation peak and emission peak at wavelength of 450 nm and 605 nm respectively[21]. The fluorescence of $Ru(bpy)_3^{2+}$ is quenched by oxygen and the emission intensity is governed by the oxygen concentration according to

$$\frac{I_0}{I} = 1 + K_{SV} * [O_2]$$

where I is the intensity at the oxygen concentration $[O_2]$ expressed as partial pressure, I_0 is the intensity in the absence of oxygen and K_{SV} is the Stern-Volmer quenching constant. For $Ru(bpy)_3^{2+}$ the K_{SV} is determined by the nearly diffusion-controlled bimolecular rate constant[22]. We need to correct for the use of an agar pad rather than a solution since the associated difference in diffusion constant results in a different K_{SV}. To the best of our knowledge no K_{SV} for $Ru(bpy)_3^{2+}$ in agar has been published. Instead we based our correction on a comparison of K_{SV} in water and agar published for pyrene butyric acid (PBA), which is another oxygen-quenched fluorescent dye with a near diffusion-controlled rate constant. For PBA the K_{SV} in water is reported by Benson *et al.*[23] to be 1.5 atm^{-1} while for agar it is 1.18 atm^{-1}. Assuming the effect of agar on diffusion of PBA to be similar to the effect of agar on diffusion of $Ru(bpy)_3^{2+}$ we can calculate the expected fluorescence ratio in agar by

$$\frac{I_0}{I} = 1 + K_{SV_{H_2O}}^{Ru(bpy)_3} * f_{agar} * [O_2]$$

with $K_{SV_{H_2O}}^{Ru(bpy)_3}$ as the quenching constant for $Ru(bpy)_3$ in water, and

$$f_{agar} = \frac{K_{SV_{agar}}^{PBA}}{K_{SV_{H_2O}}^{PBA}}$$

as the ratio of quenching constants for PBA in agar ($K^{PBA}_{SV_{agar}}$) and water ($K^{PBA}_{SV_{H_2O}}$) . The quenching constant in agar would then equal 1.42 atm^{-1}, and the expected fluorescence ratio for 0 to 21 % oxygen is then calculated to be 1.3 atm^{-1}. Ultimately, a decrease in oxygen concentration from 21 % to 0 % should increase fluorescence in pads by 30 %, with the inverse relationship allowing for high signal-to-noise ratios. Besides quantification we can also use a qualitative measure of the biological impact of any remaining oxygen.

We can qualitatively assess the dependence on iron as electron acceptor in the presence of oxygen using our microcolony growth observations. In microaerobic environments exponential growth of *G. sulfurreducens* in the presence of oxygen was only observed when another electron acceptor was present. The absence of an alternative electron acceptor resulted in linear growth instead[18]. As such, if we observe linear growth this could indicate the use of oxygen as sole electron acceptor, while exponential growth would indicate the use of a second electron acceptor (presumably iron). Observations should focus on early growth since modeling of colony growth showed that colony surface area increases exponentially at first[24–26] but later stabilizes into linear growth over time[25–27] regardless of electron acceptor. Jiang *et al.*[28] showed that the same pattern holds for an insoluble electron acceptor, with *G. sulfurreducens* growth on electrodes stabilizing into linear growth between 40 and 60 hours. Thus, microcolony growth should be observed within 48 hours to identify whether growth on the available electron acceptors results in linear (oxygen as sole electron acceptor) or exponential (iron as primary electron acceptor) growth. If iron is used as the primary electron acceptor our method can be used to study wire dependence, depending on its overall performance in observing microcolony growth.

We assess the performance of our method for each of the separate criteria: morphological characterization, 2D growth, single cell identification in presence of iron particles, measurement period sufficient for growth to multilayer microcolonies, and anaerobicity. Additionally, we evaluate its overall performance in the context of a preliminary investigation. For the preliminary investigation we study whether growth of microcolonies in contact with iron particles differed in terms of microcolony shape or area from that of microlonies separate from the particles. If growth differs between the on or off iron particles, we consider whether the effect is dependent on pili, their conductivity, and time. Taken together, we will characterize the suitability of this method for its purpose of studying microcolony growth dependence on wires, taking into account any oxygen presence and the two types of conductive wires. Once an effective method has identified, future work can then focus on characterizing the impact of protein wires on biofilm formation as an avenue for MFC engineering.

2.2 METHODS

PRECULTURE GROWTH

wild type, ΔpilA and Aro-5 *G. sulfurreducens* strains were obtained from the Leibniz Institute DSMZ collection. Cultures were pre-grown in FreshWater medium with 40 mM Acetate and 10 mM Fumarate (FWAF medium, as reported in Reguera *et al.*[29]) in a 100 ml flask crimp-sealed with butyl rubber stoppers in which the headspace was replaced with a 80 % v/v nitrogen and 20 % carbondioxide gas mixture. To 38.6 ml FWAF medium 0.4 ml of 100 mM cysteine (an oxygen scavenger) and 1 ml of dense (OD_{600} of 4) stock culture was added immediately prior to incubation, followed again by replacement of the headspace, resulting in an initial OD_{600} of 0.04. Flasks were statically incubated at 30 °C for 54 hours in which an OD_{600} of at least 0.5 was reached. Grown cultures were diluted with FWA medium (FWAF medium lacking the electron acceptor fumarate) to an OD_{600} of 0.1 which was used for deposition for agar pads. Deposition of a culture with OD_{600} of 0.1 resulted in deposition of single cells, rather than clusters of cells (figure 2.1). All steps were performed in an anaerobic glove box through which nitrogen gas was continuously flushed and anaerobicity was regularly checked via 1 mM resazurin solutions which turn pink upon exposure to oxygen. Syringes used in transferring solutions were flushed several times with the nitrogen/carbondioxide gas mixture before use.

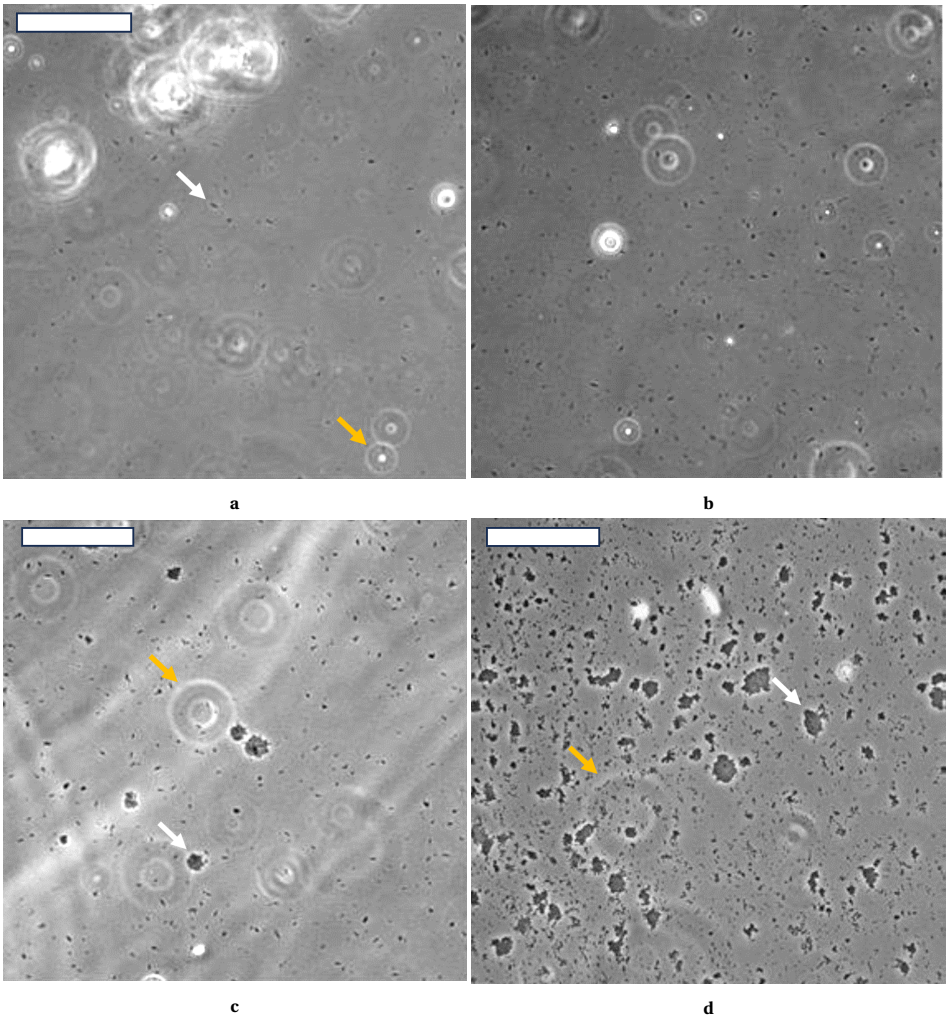

Figure 2.1: Phase-contrast micrographs at 20x magnification of 1 µl of *G. sulfurreducens* cultures of various optical densities deposited on an object slide and sealed with an agar pad. Cultures with optical densities measured at 600 nm (OD_{600}) of 0.1 (**a**), 0.2 (**b**), 0.5 (**c**) and 0.7 (**d**) were used. Deposition of a culture with an OD_{600} of 0.1 results in single separate cells (**a**), while higher optical densities result in cells in close proximity of each-other (**b**) or clusters of cells (**c** and **d**) Examples are indicated by white arrows, scalebar equals 100 µm. In this study cultures were deposited with an OD_{600} of 0.1. Bright rings are artefacts of phase-contrast microscopy due to out-of-focus objects, examples are indicated by orange arrows.

AGAR PADS

Agar pads were prepared using flow chambers attached to pre-cleaned object slides. Flow chambers (Grace Bio-labs SecureSeal Hybridization Chamber, see figure 2.2a) were cleaned with ethanol allowed to vaporize in an sterile environment. Object slides were thoroughly cleaned by sonicating the slides in a degassed 25 % KOH-ethanol solution for 5 minutes after which the slides were washed in degassed Milli-Q. The slides were then sonicated in another degassed Milli-Q container, washed with Milli-Q followed by ethanol, blown-dry with an air-gun and left to dry at 100 °C in an incubator for 20 minutes, after which the slides were kept in a sealed container.

Agar was prepared by adding 600 mg to 10 ml tubes which were subsequently autoclaved. To these tubes then 4 ml of previously prepared anaerobic FWA medium is added, mixed, and left to solidify resulting in 1.5% agar. Prior to use the agar is melted inside the tube in the microwave, after which it is transferred to eppendorfs in a heat block inside the glove box.

Amorphous Fe(III) oxyhydroxide was synthesized by adding NaOH to a 1 M solution of $FeCl_3$ until the pH was 7 as described by Lovley and Phillips [30]. Immediately before deposition of bacterial culture on object slides we added amorphous Fe(III) oxyhydroxide to bacterial culture in a 1:100 ratio.

Agar pads were shaped as follows. A flow chamber is attached to an object slide in the glove box and using a nitrogen-flushed syringe the molten agar is added to the flow chamber until it is full and left to solidify at the temperature at which the experiment will occur. After solidification the flow chamber is gently lifted from the object slide with the agar remaining on the object slide. Using a sterilized scalpel the pad is shaped to a 2 x 1.5 cm rectangular shape after which the pad is ready for immediate use.

Amorphous Fe(III) oxyhydroxide was then added to the pre-grown culture, the culture was mixed, and 1 µl of that mixture was dropped on another object slide. The agar pad was then gently transferred to the object slide, sealing cells and iron particles between the agar pad and the object slide. Finally, a new chamber with two stoppered needles connected to the chamber via Microbore PRFE tubing (0.55 mm inner diameter, 1.07 mm outer diameter) and a press-fit tubing connector was placed upon the object slide. This setup resulted in pads sealed at the top by the flow chamber but with its sides exposed to the chamber volume. The chamber volume was only exposed to air via the needles if the stopper is removed. The flow chamber pad was then transferred to an incubator where the stoppers were quickly removed and the needles connected to a flow system located inside the incubator.

The flow system consisted of a gas cylinder containing a gas mixture of 80 % nitrogen and 20 % carbondioxide gas with less than 1 p.p.m oxygen connected with butyl rubber tubing to 5 sparging bottles filled with Milli-Q. These bottles were followed by a sparging bottle without a sparging head (see figure 2.2b). In the final bottle the lack of a sparging head resulted in single large bubbles (rather than dozens of small bubbles), allowing for empirical determination of flow rate based on the bubble rate. Flow was then tuned using a flow valve on the gas cylinder while setting the bubble rate to two bubbles per second. For a rough estimate of the flush rate of the chambers we used the diameter of the bubble which was approximately 1 centimeter. This results in an approximate flow rate of 1 ml/sec, while each flow chamber with an agar pad has an approximate

headspace volume of 0.7 ml. With 6 flow chambers connected to the flow that results in each chamber's headspace being flushed every 4.2 seconds.

The final bottle was connected to a 3D-printed flow splitter in the form of a hexagonal chamber with one tube connector in the bottom and six squeeze connectors for needles on the top (see figure 2.2c). Besides distributing one gas flow to six flow chambers the splitter chamber also served to prevent any condensation from affecting the flow rate, since droplets would accumulate in the chamber more than the tubing.

For sealing pads we used a mixture of equal volumes Vaselin, Lanolin and Paraffin (VALAP). The pad was prepared as above and cells were sealed between the pad and object slide, but instead of a flow chamber the pad was covered by a rectangular subject slide larger than the pad. Liquid VALAP was injected underneath the overhanging edges of the subject slide and left to rapidly solidify, creating an airtight seal around the pad. Sealed pads were incubated inside an incubator oven situated in the glovebox.

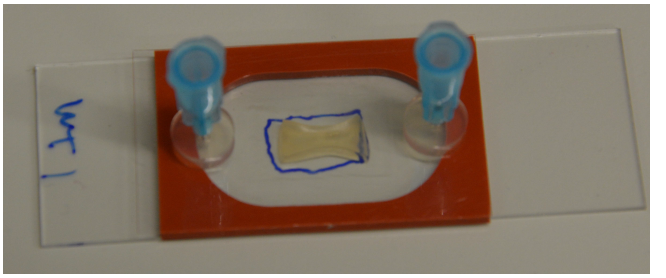

a

b

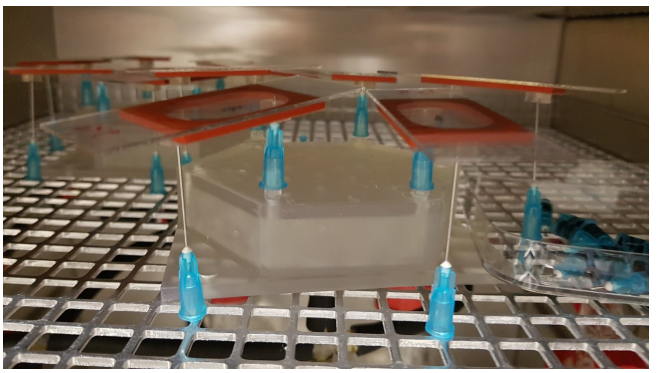

c

Figure 2.2: Flow setup used for incubation of agar pads in flow chambers. (**a**) A flow chamber forms an airtight seal with an objective slide and contains an agar pad of 2 by 1.5 cm (indicated by blue outline) past which gas is flushed through the needles connected via a press-fit tubing connector, if the gas is not humidified the pads will rapidly desiccate and shrink as shown. (**b**) In order to flush humidified oxygen-free gas past the agar pad a gas mixture of 80% nitrogen and 20% carbondioxide with less than 1 ppm oxygen was flushed through a series of sparging bottles containing Milli-Q connected via butyl rubber tubing and glass connectors located in an incubation oven. The final bottle lacks a sparging head resulting in bubbles with an approximate diameter of 1 cm, the rate of which was used to estimate gas flow rate and set flow rate to 1 ml/sec. (**c**) The final bottle is connected to a 3D printed flow splitter consisting of a hollow chamber with one tubing connector below and six needle connectors above (two flow splitters are shown, in practice only one flow splitter was connected). Flow chambers were connected to the flow splitter with the needle connector on one end, while the other end is connected to the atmosphere through a needle.

MICROCOLONY IMAGING

To ensure that we were able to capture particles and microcolonies representative of general growth we chose to image the whole pad. Pads were typically imaged in a 20 x 20 grid of overlappig images at 20x magnification using phase contrast microscopy at 0, 1, 2 and 6 days of incubation. To acknowledge the uneven distribution of time points we define growth occurring from day 0 to day 1 to day 2 as "early growth" while growth from day 2 to day 6 is termed "late growth".

Microscope table movements between images resulting in the overlapping grid were controlled by the built-in montage function of the microscope, after selecting the appropriate corner coordinates. The overlapping images were stitched together using ImageJ to create one full view of the pad (figure 2.3a). From this full view representative regions were selected on day 6 (see example in figure 2.3b) for analysis based on a visual estimate of the distribution of particles, i.e. capturing only regions where particles were present. In each region all iron particles and associated visible microcolonies were manually selected as Regions of Interest (RoI) in ImageJ, each RoI representing one "on-iron" microcolony. For each region an "off-iron" microcolony was selected in a RoI as close to the particle as possible but at least 40 µm separate from the particle. For each microcolony the selection outline was matched as close as possible and holes in microcolonies were not included in microcolony area.

A history of each microcolony was determined by selecting microcolonies in images of days 0, 1 and 2 that lay within the microcolony RoI of day 6 mapped on to the same location. These colonies from earlier days of incubation are termed "ancestral microcolonies", in case multiple microcolonies were present each is a separate ancestral microcolony. However, in the history analysis of surface area the sum of those ancestral microcolonies' surface area is used to represent the surface area at each day. In case no ancestral microcolony or cell could be distinguished from the iron we approximated its area by using the mean surface area of single cells.

When comparing multiple pads of one strain we imaged the growth of a batch of 6 pads. Three of those six pads were selected for analysis based on flow chamber integrity (i.e. no desiccation or visible leaks in chamber adhesion occurred) and image quality (i.e. majority of particles in focus, for each time point). For detailed analyses one of those pads was randomly selected. From that pad 24 on-iron microcolonies were identified from the images taken at day 6. Those microcolonies were associated with 13 particles across 6 locations on the pad. Additionally, for each location we identified one off-iron microcolony.

To describe the shape of microcolonies we determined the length, width and aspect ratio of on-iron and off-iron microcolonies as follows. All distances were first determined in pixels, then multiplied by the actual width of one pixel which was 0.4 µm. Off-iron microcolony length and width were defined as the major and minor axis of an ellipse fit to the RoI. For on-iron microcolonies the microcolony contour was first divided in an "inner edge" and "outer edge". The inner edge is the section of the microcolony contour that is in contact with iron, i.e. the section where the microcolony contour overlapped with the particle contour(figure 2.4a). The outer edge is the rest of the contour, i.e. the section of microcolony contour that did not overlap with the particle contour. The inner edge RoI was determined by expanding the RoI of the iron particle by 1 pixel and taking

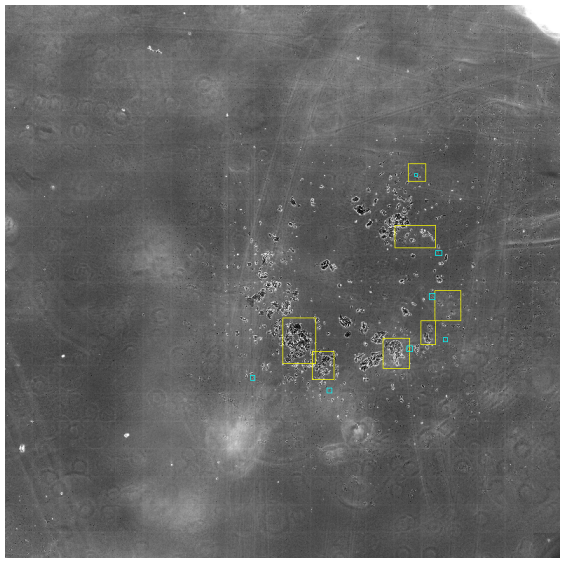

a

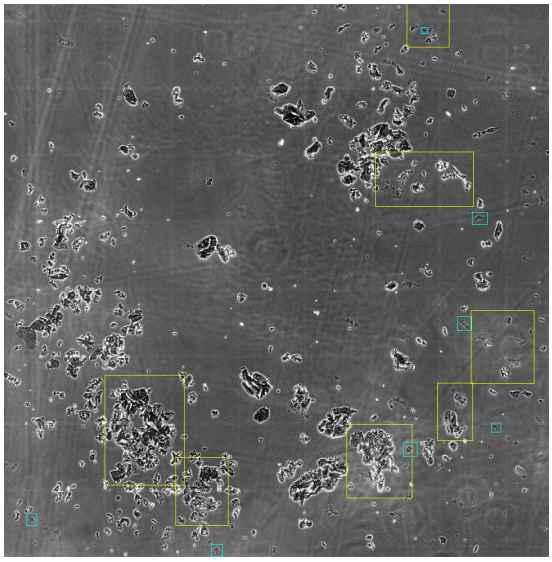

b

Figure 2.3: Stitched 20x magnified phase-contrast micrograph of a full agar pad (**a**) and a zoomed-in section (**b**) on the region containing iron particles . The full image is stitched together from separate slightly overlapping images taken in a grid of typically 20 by 20 images. From the general area containing iron particles a number of regions were selected in a spread-out pattern (regions indicated in yellow). In each region all microcolonies in contact with iron particles were manually selected and analyzed ("on-iron" microcolonies). For each region the closest microcolony separated at least 40 µm from iron (an "off-iron" microcolony) was selected from within the region or as close as possible to the region as reference point for general growth in that region, called an off-iron microcolony.

the overlap of expanded particle RoI and microcolony RoI. The outer edge RoI was determined by shrinking the RoI of the entire microcolony by 1 pixel and substracting both the shrinked RoI and inner edge RoI from the microcolony RoI leaving only the outer edge RoI.

On-iron microcolony length was defined as the length of the inner edge. On-iron microcolony width was defined as the mean distance from the outer edge to the inner edge termed the mean peripheral distance. The mean peripheral distance was determined by calculating the distance of each pixel in the outer edge to the nearest pixel of the inner edge and taking the mean. For this we made a Euclidian Distance Map (EDM) based on the inner edge RoI using ImageJ (see example in figure 2.4b). The intensity of this EDM equals the distance in pixels to the nearest pixel of the base of the EDM with the inner edge set as the base. The mean peripheral distance to iron was then determined as the mean EDM intensity of all pixels in the outer edge RoI multiplied. The aspect ratio of both on-iron and off-iron microcolonies is used as measure of elongation and is defined as the ratio of microcolony length to width, i.e. Aspect Ratio = $\frac{\text{Microcolony Length}}{\text{Microcolony Width}}$, using the on-iron and off-iron specific definitions of microcolony length and width described above.

The results are analysed using the non-parametric Anderson-Darling and Kolgorov-Smirnov tests. The Anderson-Darling test determines whether the data follows a normal distribution by determining the integral of the distance between the cumulative distribution function of a normal distribution to the empirical distribution function of the data. In case the data was not normally distributed the two-sample Kolgorov-Smirnov test was used to determine whether two data sets belonged to the same distribution based on the maximal difference between their empiricial distribution functions. The one-tailed two-sample Kolgorov-Smirnov test was used to determine whether one of the two data sets tended towards larger values than the other based on the maximal positive and negative difference between their empirical distribution functions.

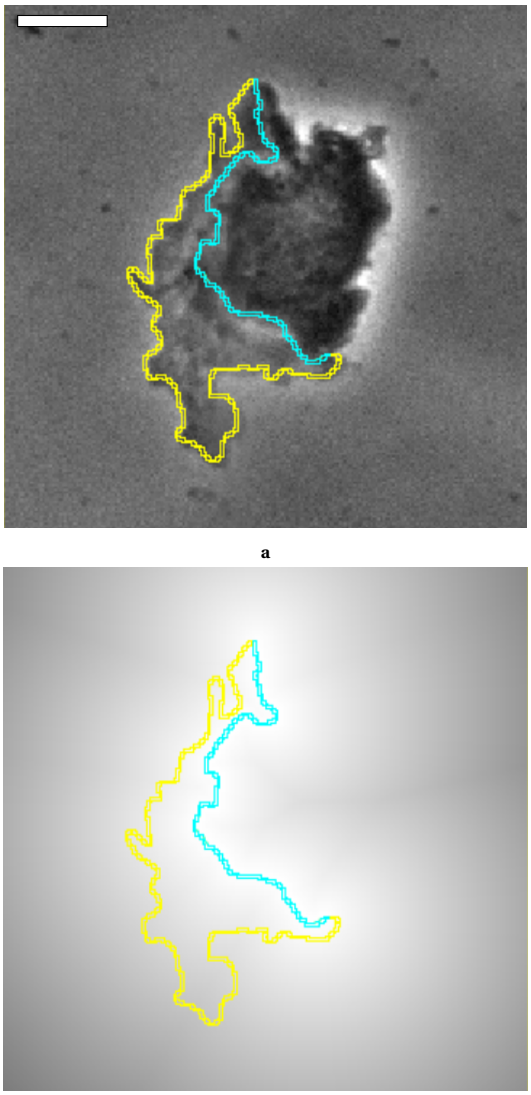

a

b

Figure 2.4: Microcolony morphology was characterized by the microcolony length and width, defined for on-iron microcolonies as the stretch of iron the microcolony is in contact with and the mean outer distance to iron of microcolonies respectively (**a**). The size of each was determined using the inner edge (blue) and outer edge (yellow) regions of interest mapped onto a Euclidian Distance Map (**b**). The inner edge is defined as the contour section of the microcolony which overlaps with the contour of the iron particle, i.e. the length of iron that is contacted by the microcolony, whereas the outer edge is the rest of the microcolony contour. For cells in the outer edge the minimum distance across which electrons must be conducted (the peripheral distance) is approximated by the minimum euclidian distance between that point and the inner edge. Microcolony length is equal to the number of pixels in the inner edge, while microcolony width is then equal to the mean value of the outer edge pixels in a euclidian distance map based on the inner edge (both multiplied by the actual size of one pixel of 0.4 µm). Scalebar equals 10 µm.

OXYGEN MEASUREMENT

To quantify the oxygen concentration inside the pads we used a 0.2 mM (2,2'-bipyridine) dichlororuthenium(II) ($Ru(bpy)_3Cl_2$) solution. $Ru(bpy)_3{}^{2+}$ is a fluorescent compound with an excitation peak at a wavelength of 450 nm, and an emission peak at a wavelength of 605 nm[21]. The fluorescence of $Ru(bpy)_3{}^{2+}$ is quenched by oxygen and the emission intensity is governed by the oxygen concentration according to

$$\frac{I_0}{I} = 1 + K_{SV} * [O_2]$$

where I is the intensity at the oxygen concentration $[O_2]$ expressed as partial pressure, I_0 is the intensity in the absence of oxygen and K_{SV} is the Stern-Volmer quenching constant which for $Ru(bpy)_3{}^{2+}$ is determined by the nearly diffusion-controlled bimolecular rate constant[22]. A decreasing oxygen concentration will increase the fluorescent signal according to the Stern-Volmer equation and should allow high signal-to-noise ratios even at low oxygen concentrations. As a control for whether the $Ru(bpy)_3{}^{2+}$ is suited for use in FWA medium we performed measurements in a spectrofluorometer with atmospheric control. First we removed the majority of oxygen in the solution by adding sodium dithionite and quickly placing the sample in the spectrofluorometer under a nitrogen gas flow, allowing us to set the oxygen at 0%. Fluorescence was measured at an excitation of 450 nm and emission of 600 nm, after which the gas flow was switched to air and fluorescence was continuously measured.

For oxygen measurements inside pads we constructed agar pads as described above, except no cells were included in order to gauge the effectiveness of the method regardless of oxygen consumption by cells. Subsequentely we defined two samples as reference points for 21% oxygen and 0% oxygen inside the pad respectively. For the 21% oxygen reference pad we prepared sealed agar pads in an aerobic environment. For the 0% oxygen reference pad we prepared pads that would be as close to anaerobic as possible: sealed agar pads with dithionite prepared in an anaerobic chamber. The sealed dithionite pad is similar to the reference sample used in the spectrofluorometer, both are dithionite exposed samples kept under an anaerobic atmosphere. Since we were setting up the method to measure oxygen concentration in a pad we did not have an independent measurement of the oxygen concentration inside these pads to confirm the zero oxygen concentration. We consider these samples as similar to the reference samples used in bulk measurements, and as such will treat them as reference points for the pads with the caveat that the lower limit is expected to be close to zero but is not confirmed to be zero.

2.3 RESULTS

METHOD VIABILITY

OXYGEN CONTENT

To study the 2D growth of microcolonies on iron we sealed the cells under an agar pad with iron particles in a flow chamber. Oxygen-free gas was flowed past the agar pad to maintain an anaerobic or microaerobic environment in which we can observe microcolony growth on iron particles. For maximum wire dependence the oxygen concentration in the pad should be zero but any concentration below 5 % should allow for microcolony growth observation. In order to check whether the pads were indeed anaerobic (or microaerobic) we measured oxygen concentration through its quenching effect on $Ru(bpy)_3^{2+}$ fluorescence. First we examined the sensitivity of this method in liquid FWA medium in a controlled atmospheric environment. The fluorescence at 0 % oxygen was 1.40 ± 0.01 times higher than fluorescence at 21 % oxygen, as seen in figure 2.5. Since the oxygen scavenger dithionite is added before the 21 % measurement, we checked for the possibility that dithionite affects subsequent $Ru(bpy)_3^{2+}$ sensitivity. After exposing a dithionite sample to air for an extendend amount of time (thus allowing all dithionite to react with oxygen) we used the atmosphere control to switch back to nitrogen. Upon continued exposure to a nitrogen atmosphere a similar ratio of fluorescence between the oxygen-rich and oxygen-poor conditions as caused by dithionite treatment were found (1.37 ± 0.014). With the Stern-Volmer equation and K_{SV} for $Ru(bpy)_3^{2+}$ being 1.81 atm^{-1} reported by Oter and Ribou [31] we can calculate that the ratio should equal 1.38, close to our observed values.

After showing the consistent sensitivity of the dye in liquid medium we performed a similar experiment on pads. The 0 % reference pads prepared with dithionite in the glove box had 1.29 ± 0.05 times the fluorescence of the 21 % reference pads prepared in aerobic conditions. We used this as reference for the performance of our flow setup. For pads prepared in aerobic conditions and subsequently placed in the flow setup for one day had the final fluorescence was 1.28 ± 0.05 higher than initial fluorescence. The expected fluorescence ratio for 0 to 21 % oxygen was calculated to be 1.3, which is close to our observed value of 1.28 ± 0.05. There are too few measurements to reliably determine the confidence interval of the oxygen concentration in the pad. However, the lowest fluorescence ratio of 1.16 corresponds to an oxygen concentration of 10 %, which should still be toxic to *G. sulfurreducens* , while the other two pads had fluorescence ratios slightly higher than the reference pads (1.34 and 1.33), corresponding to zero oxygen. It is possible that these measurements represent two different states of the system with values around 10% indicating the presence of a leak, while those around 0 % represent a sealed system.

Since the fluorescence ratios of pads exposed to the flow system are very similar to the reference and calculated values, we can conclude that in those cases our flow setup was able to set and maintain pad oxygen concentrations similar to those in pads prepared with dithionite in an anaerobic atmosphere, but not in all cases. We are unable to prove whether that condition is indeed 0% oxygen until we perform a check of the reference pads using another verified method for measuring oxygen in pads.

MICROCOLONIES

The relatively low level of oxygen inside pads allows us to check whether microcolony growth was now possible under these anaerobic/microaerobic conditions. In a typical growth experiment the pads were fully imaged at the start of incubation and again after 24, 48 and 144 hours (i.e. 1, 2 and 6 days). Under these conditions microcolonies were able to grow on iron particles, as is clear from the typical growth process displayed in figure 2.6.

Notably, cell growth separate from the iron particles also occurred. Since the iron particles are the only intentionally included electron acceptor, there appears to be a secondary unintentional electron acceptor present. At low but non-zero oxygen concentrations it is possible that oxygen serves as electron acceptor. In this micro-aerobic environment we would still expect the iron particles to be a relevant electron acceptor since oxygen is only poorly available but growth will not be completely dependent on access to iron particles. Although further improvements can be made we also evaluated the current ability of the method for characterizing microcolony growth on iron particles.

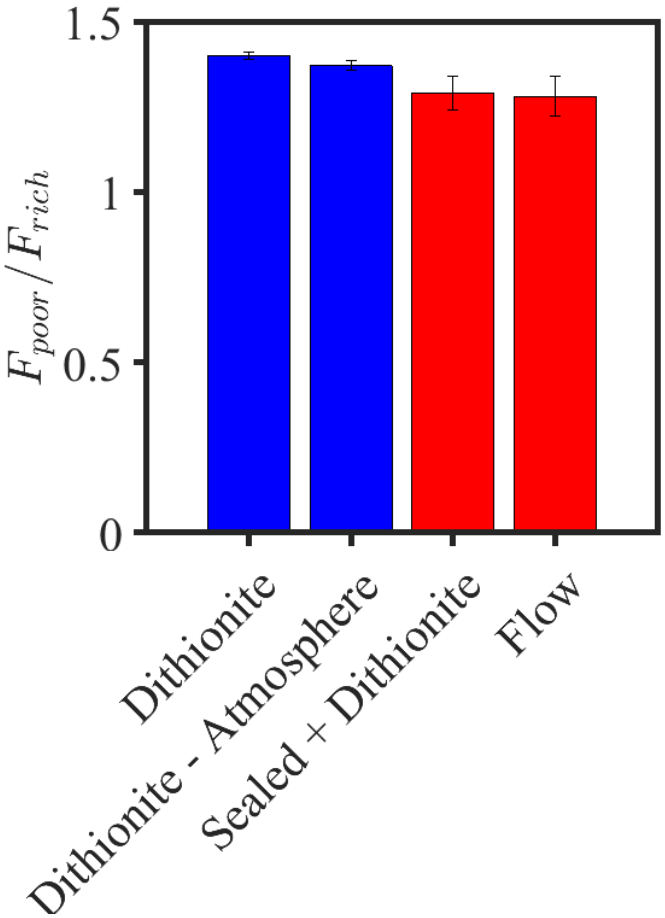

Figure 2.5: Ratio of fluorescence at oxygen-poor (F_{poor}, close to 0%) or oxygen-rich (F_{rich}, 21 %) conditions for liquid medium (Blue bars) or agar pads (Red bars) containing 0.2 mM (2,2'-bipyridine) ruthenium(II) ($Ru(bpy)_3^{2+}$). For the $Ru(bpy)_3^{2+}$ solutions the fluorescence was determined before and directly after adding the oxygen scavenger sodium dithionite to a concentration of 0.1 mM ("Dithionite"), as well as after first exposing the same solution to air followed by pure nitrogen ("Dithionite-Atmosphere"). For the agar pads the fluorescence was determined in an oxygen-poor and oxygen-rich condition in two different situations, of which the ratio between oxygen-poor and oxygen-rich fluorescence is depicted. In the first situation ("Sealed + Dithionite") we added the dithionite solution to molten FWA agar containing $Ru(bpy)_3^{2+}$ and prepared three agar pads in an anaerobic (oxygen-poor) and three agar pads in an aerobic (oxygen-rich) environment after which each chamber was sealed . In the second situation ("Flow") three agar pad were prepared with the $Ru(bpy)_3^{2+}$ solution in aerobic conditions (oxygen-rich), without dithionite, and then maintained under an anaerobic flow for one day (oxygen-poor). Error bars indicate standard error of the mean for triplicates. The ratio between fluorescence in oxygen-poor and oxygen-rich conditions behave as expected according to the Stern-Volmer equation, with an expected ratio of 1.4 for solutions and 1.3 for agar.

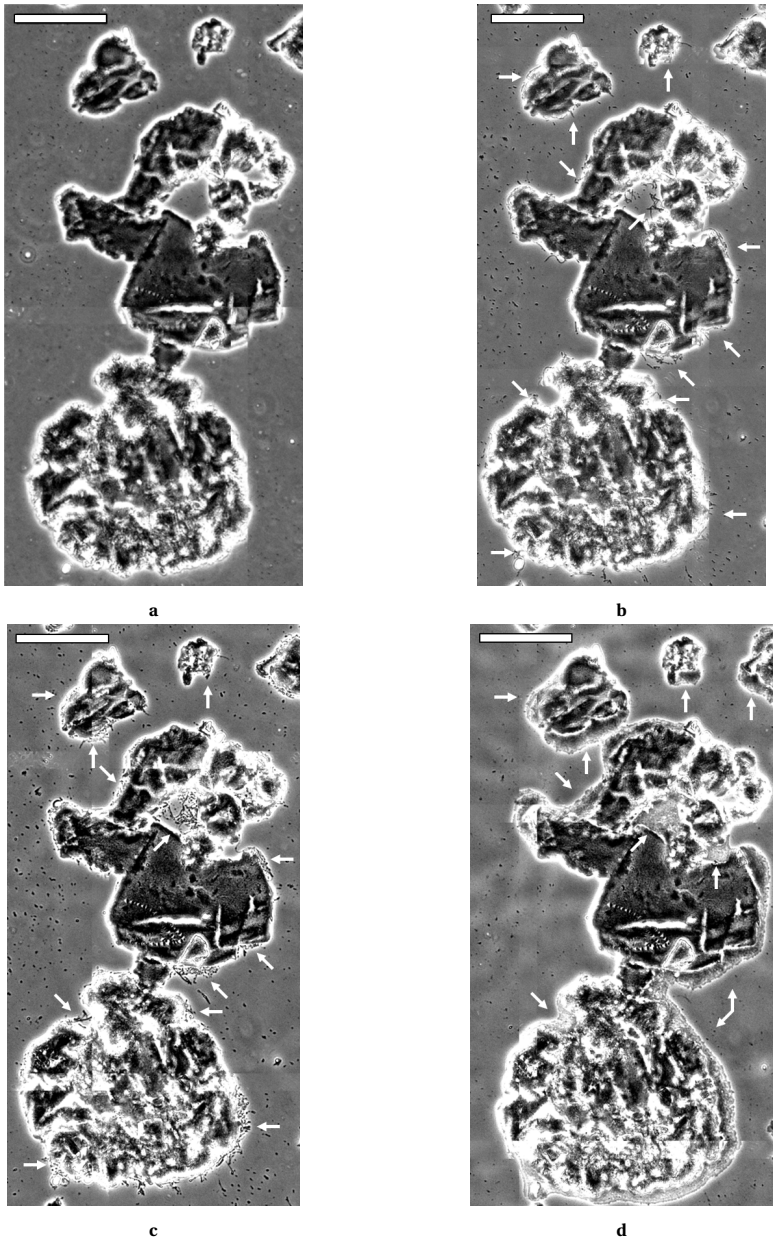

Figure 2.6: Section of stitched 20x magnified phase-contrast micrograph depicting typical wild type microcolony growth on iron particles after 0 (**a**), 1 (**b**), 2 (**c**), and 6 (**d**) days of incubation at 30° C on micro-/anaerobic agar pads. Microcolonies visible after 6 days to be comprised of more than 1 layer of cells, they can also be comprised of agglomerates of multiple early growth (1 or 2 days) microcolonies. microcolony growth tends to follow the iron particle edge. Bright areas around object edges are an artefact of phase-contrast microscopy. Scalebar equals 100 µm, white arrows indicate visible microcolony growth when compared to the particle after 0 days of growth.

MICROCOLONY CHARACTERISTICS

SURFACE AREA

Having shown that we can grow microcolonies on agar pads in the presence of iron particles we can start to quantify key characteristics of that growth. In particular, we investigated whether growth of microcolonies in contact with iron particles differed in terms of microcolony shape or area from that of microlonies separate from the particles.

A typical growth process is visible in figure 2.6, where one large particle as well as a midsized and small particle are seen with numerous microcolonies growing along the edges of those particles. On day 0 it is not possible to identify single cells on the particles, while at day 1 and 2 it is possible to discriminate individual cells comprising a microcolony. The separation of time points into "early growth" (day 0 to day 1 to day 2) and "late growth" (day 2 to day 6) is reflected in a change in microcolony structure from day 2 to day 6. Microcolonies in close proximity at day 2 have agglomerated at day 6 into single large microcolonies that possess a grainy texture, seemingly due to dense stacking of cells with no clear delineation between one cell or another. At day 6 it seems that microcolonies are no longer a monolayer but have increased in height in addition to length and width. Notably, off-iron microcolony growth appears to occur isotropically as can be seen in figure 2.7, while on-iron microcolonies instead appear to grow along the iron particle edge as seen in figure 2.6. Additionally, despite the lack of access to an iron particle the surface area of off-iron microcolonies appears to be within the same order of magnitude of on-iron microcolonies.

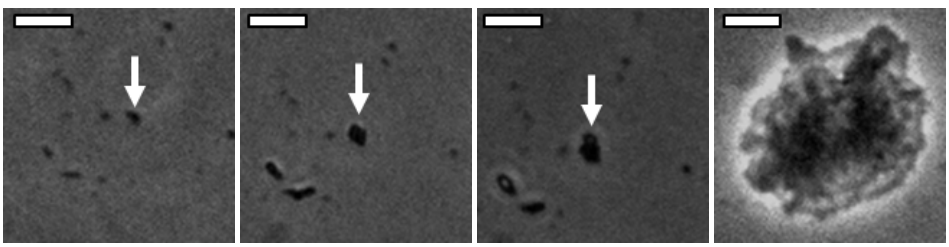

a **b** **c** **d**

Figure 2.7: Section of stitched 20x magnification phase-contrast micrograph depicting typical wild type microcolony growth at least 40 µm away from iron particles after 0 (**a**), 1 (**b**), 2 (**c**), and 6 days (**d**) of incubation at 30° C on micro-/anaerobic agar pads respectively. Microcolonies visible after 6 days to be comprised of more than 1 layer of cells, they can also be comprised of agglomerates of multiple early growth (1 or 2 days) microcolonies. Microcolony growth off iron appears to generally result in a circular microcolony shape. Bright areas around object edges are an artefact of phase-contrast microscopy. Scalebar equals 10 µm, white arrows indicates ancestral microcolony or cell.

To quantify the qualitative observations we manually selected each identified day 6 on-iron microcolony. Additionally we selected the associated iron particle and reference off-iron microcolony. These selections provide a measure of microcolony area which we will discuss in its interpretation as growth. Microcolonies ranged in size from 63 μm^2 up to 3526 μm^2, with 75 % between 500 and 2000 μm^2, as can be seen in the histogram depicted in figure 2.8, and a median size of 1167 μm^2. For off-iron microcolonies 85% grew to a size between 500 and 2000 μm^2 with a median size of 1069 μm^2. The on-iron microcolonies did not stem from the same distribution as off-iron microcolonies, but did

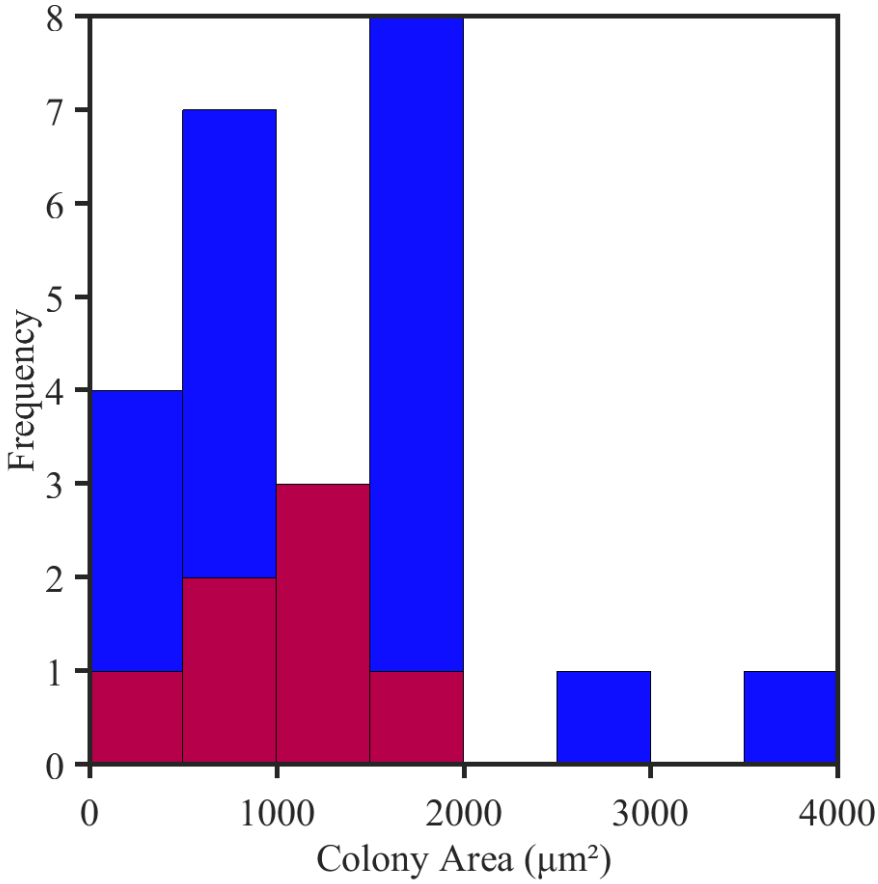

Figure 2.8: Distribution of area of on-iron (blue) and off-iron (transparent red, overlapping on-iron and off-iron bars appear dark-red) wild type microcolonies grown on agar pads containing iron particles after 6 days of incubation. Area was determined by manually selection microcolonies on 20x phase-contrast micrographs with a resolution of one square pixel of 0.16 μm^2. Neither on-iron or off-iron microcolony areas were normally distributed (Anderson-Darling test, $A^2 = 3.91$, critical value = 0.73, and $A^2 = 0.74$, critical value = 0.65 respectively, $p < 0.025$ for both). The median on-iron microcolony size is 1167 μm^2 and median off-iron microcolony size is 1069 μm^2. Considering the average imaged size of single cells was 4.1 $\pm$0.5 μm^2, the median microcolony sizes for on-iron and off-iron microcolonies correspond to a minimum of 284 and 260 cells in a median microcolony.

not significantly tend towards larger values than off-iron microcolonies (Kolmogorov-Smirnov test, D = 0.91, p < 0.01 for both) despite the slightly higher median. The similar range and median area of off-iron and on-iron microcolonies supports the qualitative observation that a lack of direct access to iron as electron acceptor does not necessarily limit microcolony area. The quantitative analysis can provide more detailed information on the general microcolony growth process, whether occurring on or off iron.

The average area of a single cell (A_{cell}) was determined to be 4.1 ±0.5 μm^2 using the single cells identified as ancestral cells for all selected wild type off-iron microcolonies. If we assume the average imaged area of a single cell to be constant in time, we can take the area of a microcolony as proportional to the number of cells in it and estimate the number of cells in the microcolony by dividing microcolony area by the average imaged area of a single cell. Note that the assumption of a constant average imaged area of a single cell is less likely to hold for large microcolonies (typically present on day 6) where cells are closely packed and multiple layers of cells may arise, resulting in the same imaged area containing more cells than estimated here. Keeping this limitation in mind, the number of cells in a microcolony at day 6 to range from 15 to 860 with a median of 284.

GROWTH DYNAMICS

If growth on pads within 6 days occurs exponentially the large range of cell number could be explained by variations in growth rate. Additionally, exponential growth would indicate that cells have access to an electron acceptor other than oxygen since growth solely on oxygen occurs linearly. To investigate whether microcolony growth is best described by an exponential or linear relationship we determined the history of each microcolony by identifying the ancestral microcolonies on the images made on days 0, 1, and 2. The smallest microcolony identified was 8.3 μm^2, corresponding to two cells.

From the microcolony histories in figure 2.10 it appears that an exponential relationship between time and median microcolony area described by $A(t) = A_0 * e^{\mu t}$ results in a higher coëfficient of determination than a linear relationship described by $A(t) = A_0 * \mu t$ with $R^2 = 0.96$ compared to $R^2 = 0.85$ respectively, where A(t) is microcolony area after t hours, A_0 is starting microcolony area and μis the growth rate. As a descriptor of median growth the exponential relationship therefore seems to represent growth better than a linear relationship. From the fit of an exponential relationship the growth rate is determined to be 0.040 h^{-1}, which is lower than reported[32] for growth on dissolved iron (0.07 h^{-1}), but close to the growth rate reported[33] for other *Geobacter* species grown on iron oxide particles (0.037 h^{-1}).

One advantage of single cell imaging over bulk experiments is the ability to visualize cell or microcolony heterogeneity. When performing fits on the combined data of all microcolonies (instead of just the median values) an exponential fit is still the better fit but the coëfficient of determination is lower for both, with a $R^2 = 0.75$ versus $R^2 = 0.50$ for exponential versus linear relationship respectively. The inability for an exponential relationship to describe more than 90 % of the per microcolony variance is in part due to non-constant growth rates. Heterogeneity in onset of growth and a decrease in growth rate after onset results in non-constant growth rates per microcolony. With regards to heterogeneous onset of growth, at day 1 there are 10 out of 24 microcolonies of which

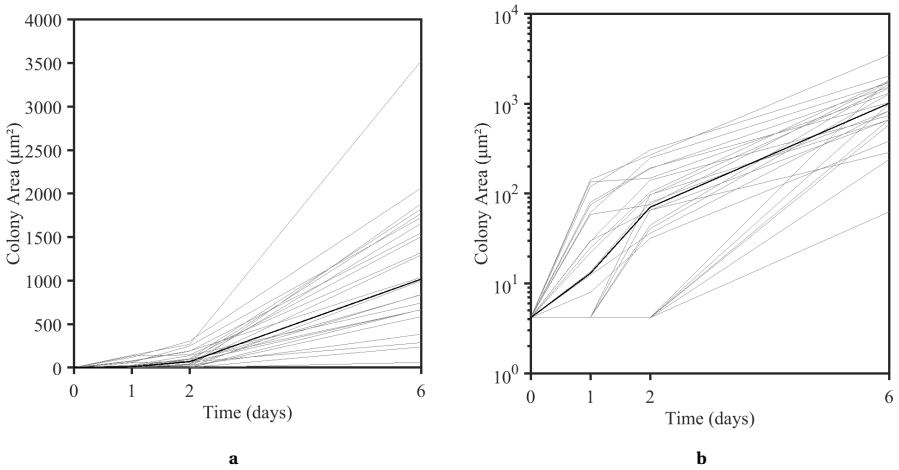

Figure 2.9: Area of on-iron microcolonies after 1, 2 and 6 days of incubation depicted on a linear (**a**) and logarithmic scale (**b**). microcolonies were identified on day 6, and corresponding ancestral microcolonies were then identified on day 2, day 1 and day 0 images. In case multiple ancestral microcolonies were identified we used the total area of those microcolonies. When ancestral microcolonies were not yet distinguishable from the particle we used the average area of day 0 off-iron microcolonies, i.e. the average area of a single cell, as an estimate. The median area at each time is represented by a thick black line. Onset of growth is heterogeneous with 10 out of 24 visibly grown on day 1, another 8 on day 2, with the last 6 only visible on day 6. Comparing the graphs plotted on a linear and logarithmic scale the median growth appears to be best described by an exponential relationship rather than a linear relationship (e.g. the exponential fit is expected to result in the highest coëfficient of determination).

the ancestral microcolony can not yet be distinguished from the particle (i.e. have not or barely grown). These cells likely remain in the "lag phase" known to occur at the start of growth. At day 2 another 8 have grown to a distinguishable size. By definition all microcolonies are distinguishable on day 6 since they were identified on that day. As such, at day 6 the remaining 6 microcolonies have grown.

The observation that growth rate is not constant is best evidenced by the microcolonies that started growing between day 0 and day 1, which had a growth rate of 0.094 ± 0.010 h^{-1} in that period, while the same microcolonies had a significantly lower growth rate of 0.043 ± 0.005 h^{-1} from day 1 to day 2 (Student's t-test, $p < 0.05$).

On a time scale of several days a simple exponential growth model with a growth rate of 0.040 h^{-1} can be a suitable model for the median size of microcolonies but is a poor descriptor of individual microcolony growth. Microcolonies might still have an exponential growth phase within one day, but a higher time resolution is required to confirm it. Having shown the ability of the method to characterize the microcolony growth process, we then investigated the ability to describe microcolony morphology by describing the effect of iron particles on microcolony shape.

MORPHOLOGY

A clear qualitative difference between on-iron and off-iron microcolonies visible on the micrographs is the non-isotropic growth of on-iron microcolonies. Having identified an effect of iron on microcolony growth, quantification of the effect and its dependence on pili conductivity may shed light on the ecological relevance of conductive properties of pili separate from their structural properties. On-iron microcolonies appear to have grown along the edge of iron particles, resulting in elongated microcolonies. To quantify this elongated growth we determined the length and with of the microcolonies based on the selections for microcolony area (see methods for a detailed definition of length and width).

The width of on-iron microcolonies tended towards smaller width than off-iron microcolonies (Kolmogorov-Smirnov test, $D = 0.83$, $p < 0.01$). The median on-iron microcolony length was 10 μm and median off-iron microcolony length was 30.4 μm. The length of on-iron microcolonies tended towards larger length than off-iron microcolonies (Kolmogorov-Smirnov test, $D = 0.73$, $p < 0.01$). The median on-iron microcolony length was 108.6 μm and median off-iron microcolony length was 41.6 μm. On-iron microcolony length tended towards larger values than on-iron microcolony width (Kolmogorov-Smirnov test, $D = 0.91$, $p < 0.001$). Their median values differed by an order of magnitude (108.6 and 10 μm for length and width respectively). For off-iron microcolony width and length are within the same order of magnitude (30.4 μm and 41.6 μm respectively).

It is clear that on day 6 the on-iron microcolonies have grown more in length along the iron than in width away from the iron. To quantify the elongation of the microcolonies in a single parameter we calculate the 'aspect ratio' as the ratio of microcolony length and width. For on-iron microcolonies an aspect ratio larger than one indicates that microcolony growth has been non-isotropic with the length of the microcolony along the iron larger than the width of the colony from the iron, with a larger number indicating a more elongated microcolony. For off-iron microcolonies an aspect ratio larger than one indicates how much larger the major axis is relative to the minor axis, i.e.

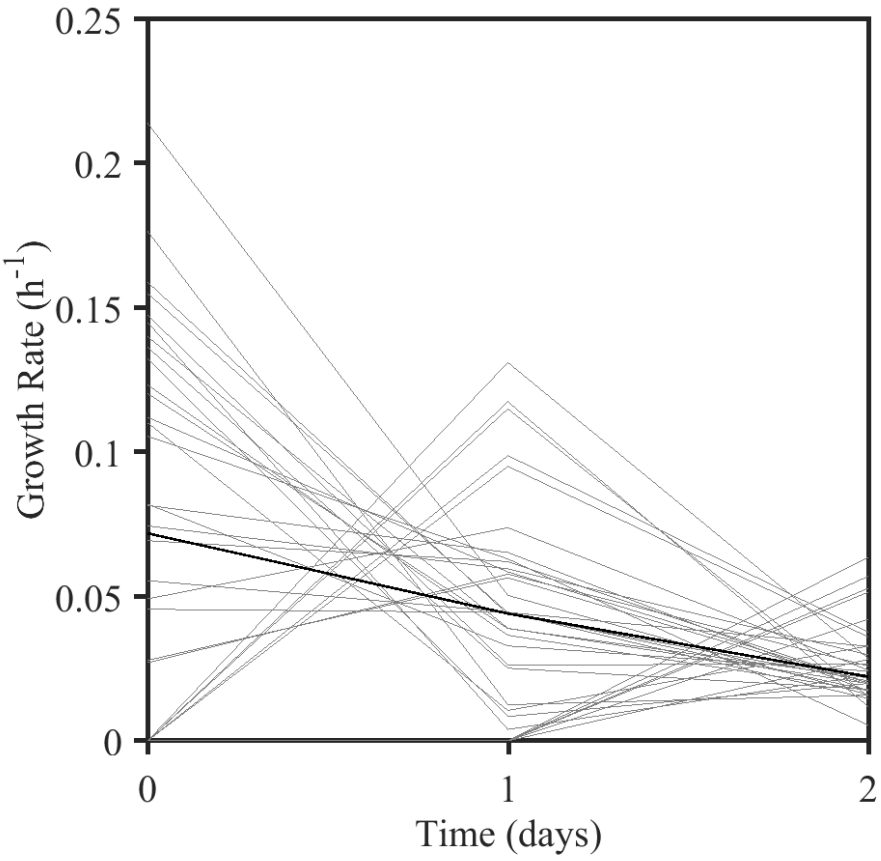

Figure 2.10: Calculated growth rate of microcolonies based on microcolony area increase from day 0 to day 1, day 1 to day 2 and day 2 to day 6 shown as growth rate on the previous time-point (i.e. growth rate on day 0 indicates growth rate based on area increase from day 0 to day 1). Growth rate was calculated based on $A(t) = A_0 * e^{\mu t}$ where A_0 is the area on the first time-point, A_t is the area on the second time-point, t is the time in between in hours, and μ is the growth rate. Median growth rate at each time-point is depicted by the thick black line, and decreases over time. Growth rate per microcolony is not constant and for microcolonies having grown from day 0 to day 1 the growth rate decreased from day 1 to day 2 from 0.094 ±0.010 h^{-1} to 0.043 ±0.005 h^{-1}.

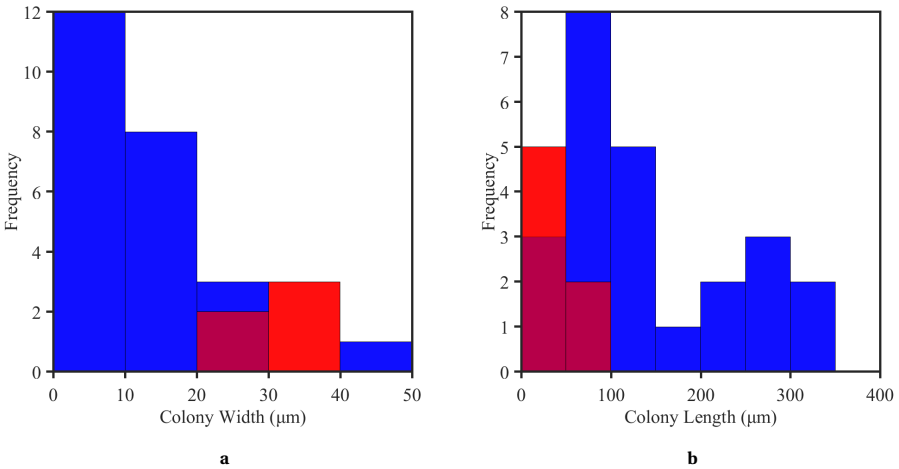

Figure 2.11: Distribution of width (**a**) and length (**b**) of on-iron (blue) and off-iron (transparent red, overlapping on-iron and off-iron bars appear dark-red) wild type microcolonies grown on agar pads containing iron particles after 6 days of incubation. Selections were made manually on 20x phase-contrast micrographs with a pixel width of 0.4 μm. For off-iron microcolonies an ellipse was fit, and microcolony length and width were defined as the major and minor axis of the ellipse respectively. For on-iron microcolonies the microcolony contour was divided in two sections: the section where the microcolony contour overlapped with the particle contour (the "inner edge"), and the section of microcolony contour not overlapping with the particle contour (the "outer edge"). The on-iron microcolony length was then defined as the length of the inner edge, and width was defined as the mean distance of the outer edge from the inner edge. The median width for on-iron microcolonies is 10 μm and off-iron microcolonies is 30.4 μm, while median length for on-iron microcolonies was 108.6 μm and off-iron microcolonies was 41.6 μm. As such, for on-iron microcolonies length is typically an order of magnitude higher than width, while for off-iron microcolonies they are of the same order of magnitude.

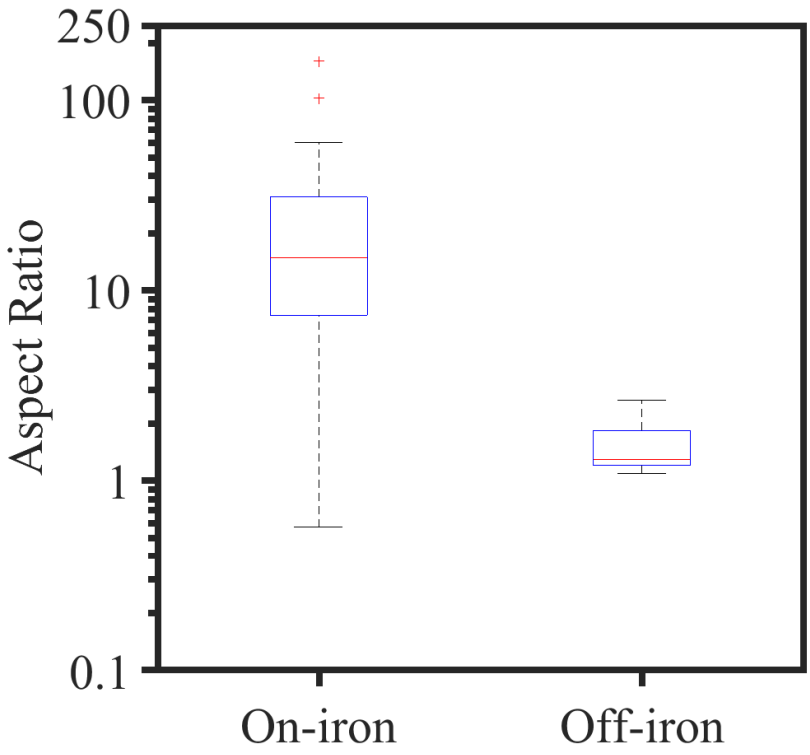

Figure 2.12: Aspect ratio of on-iron and off-iron microcolonies after 6 days of incubation. Aspect ratio is calculated as the ratio of microcolony length to microcolony width. For on-iron microcolonies an aspect ratio larger than one indicates a larger length of the microcolony along the iron than the average distance of the microcolony from the particle edge, i.e. how elongated the microcolony is along the iron edge. For off-iron microcolonies an aspect ratio larger than one indicates how much larger the major axis is relative to the minor axis, i.e. how elongated the overall shape of the microcolony is. Data is represented in a box-plot, with the red center line indicating the median value, the upper and lower limit indicating the edges of third and first quartile respectively, the caps on dashed lines indicating the maximum and minimum values, excluding the data points identified as outliers indicated by red crosses. Outliers are values lying below the first quartile minus 1.5 times the interquartile range, or above the third quartile plus 1.5 times the interquartile range. On-iron microcolonies have a median aspect ratio of 12.8, confirming the order of magnitude difference in microcolony width and length, while off-iron microcolonies have a median aspect ratio of 1.29 which is close to one, confirming the generally isotropic shape of off-iron microcolonies.

how elongated the overall shape of the microcolony is. On-iron microcolonies tended to higher aspect ratios than off-iron (Kolgorov-Smirnov test, D = 0.91, $p < 0.01$), with a median on-iron microcolony aspect ratio of 12.8 compared to a median off-iron microcolony aspect ratio of 1.29. Aspect ratio tended to increase over time (figure 2.13). The microcolonies with aspect ratio close to one or below consisted of a few cells in for example a L-shaped microcolony configuration.

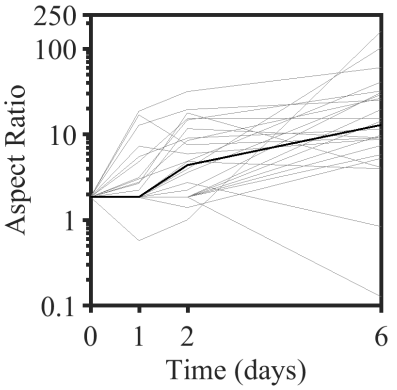

Figure 2.13: Aspect ratio of on-iron microcolonies after 1, 2 and 6 days of incubation depicted on a logarithmic scale. Microcolonies were identified on day 6, and corresponding ancestral microcolonies were then identified on images of day 0, 1 and 2. In case multiple ancestral microcolonies were identified we used the mean aspect ratio of those microcolonies. When ancestral microcolonies were not yet distinguishable from the particle we used the average aspect ratio of a single cell as an estimate. The median aspect ratio at each time is represented by a thick black line, which tends to increase with time. As such, microcolonies appear to tend to become more elongated over time. The microcolonies with aspect ratio close to or below one were microcolonies consisting of a few cells in for example a L-shaped microcolony configuration.

In summary, we found that microcolonies grew exponentially with growth rates of 0.04 h^{-1} up to a median size of 1176 μm^2. Due to growth along the iron particle edge the on-iron microcolonies were more elongated than off-iron microcolonies with a median aspect ratio of 12.8 for on-iron microcolonies compared to 1.29 for off-iron microcolonies.

While an effect of iron particles has been identified in a preferred direction of growth along their edge it is unclear whether this effect is due to the physical presence of iron, e.g. enhanced attachment or deformation of the agar pad, or due to spatial metabolic constraints caused by distance-dependent conductance of the pili. To investigate the role of conductivity we repeated the experiments with a strain producing no pili (ΔpilA) or less conductive pili (Aro-5).

WIRE DEPENDENCE

Microcolony growth of a strain without pili (ΔpilA) differed from wild type in the microcolony structure and size, while a strain producing less conductive pili (Aro-5) did not. A typical microcolony growth process for the mutant strain lacking pili (ΔpilA) is visible in figure 2.14. A notable difference between wild type and ΔpilA microcolonies is the

presence of holes in the microcolonies. Cells within the microcolonies appear to be less closely attached to each other, possibly due to the lack of attachment normally facilitated by the pili. Additionally, the selection area center of mass of certain microcolonies was observed to change over time, possibly due to cells in one area of the microcolony dying while those in another part continued to divide. The shift in center of mass could theoretically be due to a shift in the particle, but comparing the relative position of other nearby notable features with earlier images does not seem to support a relative shift of the particle in those cases. For the strain producing less conductive pili (Aro-5) the microcolonies appear similar to wild type, except both on-iron and off-iron microcolonies are noticeably larger than wild type with some even enveloping iron particles as can be seen in figure 2.15d.

The 23 on-iron ΔpilA microcolonies tended toward smaller values than wild type with a median of 154 μm^2 compared to 1167 μm^2 respectively (Kolmogorov-Smirnov test, $D = 0.63$, $p < 0.01$). In contrast, 38 Aro-5 on-iron microcolonies had a median area of 1393 μm^2 and did not stem from a significantly different distribution than wild type (Kolmogorov-Smirnov test, $D = 0.31$, $p > 0.05$). The lack of a significant difference between wild type and Aro-5 is unexpected considering the microcolonies are expected to have less effective access to the iron as electron acceptor. As such, either the Aro-5 does not have less effective access to the iron, or it is not a limiting factor in the microcolony growth described here. With regards to off-iron microcolonies, as visible in figure 2.14, they appear to have a more erratic shape than wild type off-iron microcolonies on day 6. Additionally, there seems to be general growth of the majority off-iron microcolonies from day 0 to day 1, while on day 6 only a minority have ultimately grown into large microcolonies. The fact that the off-iron microcolonies area tend to be of the similar order of magnitude of the on-iron microcolonies for any strain seems to support the idea that iron access had little effect on microcolony area.

Despite differences in structure and size between ΔpilA and wild type the preferred growth along the edge of iron seems to persist even in the absence of pili (ΔpilA) or lower conductivity (Aro-5), indicating the process to be independent from pili or conductivity. The elongated shape of microcolonies characterized by an aspect ratio larger than 1 persists in both ΔpilA and Aro-5 with a median aspect ratio of 7.6 for ΔpilA and 12.4 for Aro-5 respectively, compared to 14.7 for wild type, although neither came from a distribution significantly different from wild type (Kolmogorov-Smirnov test, $D = 0.30$ for ΔpilA and $D = 0.14$ for Aro-5, with $p > 0.05$ for both after Bonferroni correction).

Ultimately the only quantitative difference found between strains was only between wild type and ΔpilA in terms of microcolony surface area. As such, the presence of pili seems to affect microcolony growth independent from their conductivity. However, given the earlier described presence of minor concentrations of oxygen as possible alternative electron acceptor we considered that unintended variation in oxygen levels between pads may result in variations of overall microcolony area. To explore the between-pad variation in microcolony area we identified additional day 6 microcolonies from 2 more pads for each of the strains.

REPRODUCIBILITY

So far we have confirmed the method's ability to quantify microcolony growth characteristics, as well as its ability to discern between wild type and a mutant strain. Having

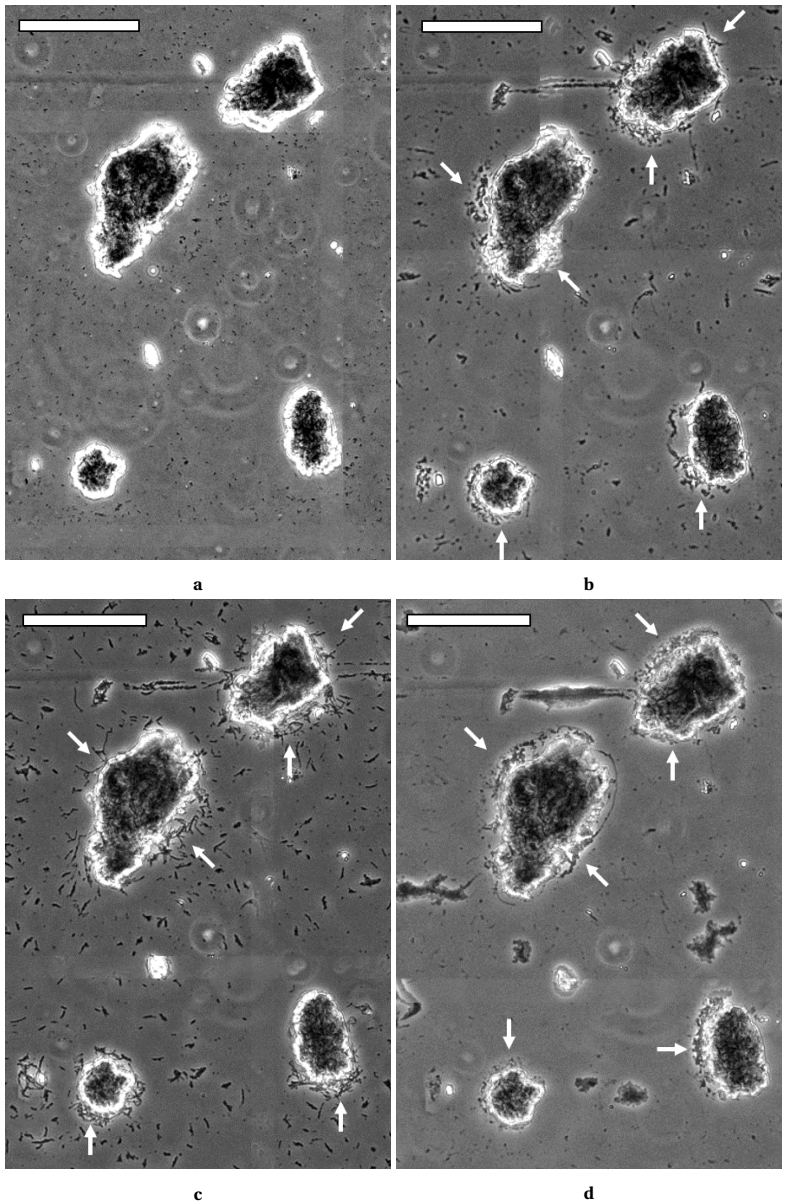

Figure 2.14: Section of stitched 20x magnification phase-contrast micrograph depicting typical ΔpilA microcolony growth at least 40 µm away from iron particles after 0 (**a**), 1 (**b**), 2 (**c**), and 6 days (**d**) of incubation at 30° C on micro-/anaerobic agar pads respectively. Microcolonies visible after 6 days to be comprised of more than 1 layer of cells, they can also be comprised of agglomerates of multiple early growth (1 or 2 days) microcolonies. Off-iron microcolony growth seems to result in a circular microcolony shape and ΔpilA off-iron microcolonies appear to have a more erratic shape than wild type. Bright areas around object edges are an artefact of phase-contrast microscopy. Scalebar equals 10 µm, white arrows indicates ancestral microcolony or cell.

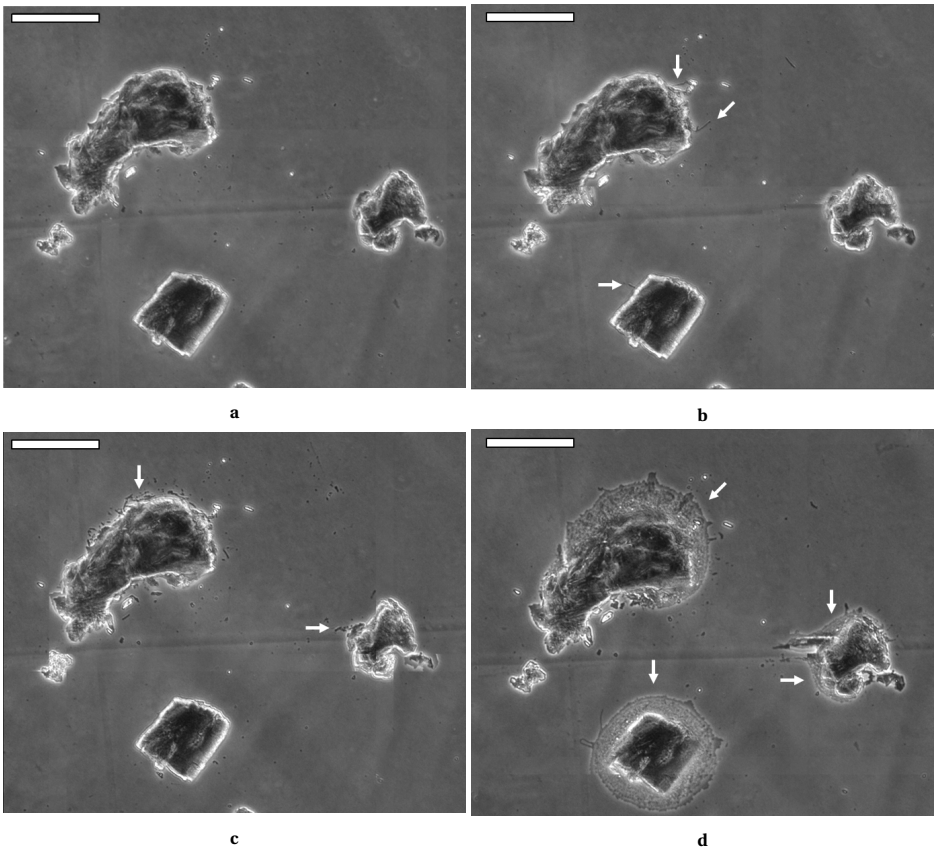

Figure 2.15: Section of a stitched 20x magnification phase-contrast micrograph depicting typical Aro-5 microcolony growth on iron particles after (**a**) 0, (**b**) 1, (**c**) 2, and (**d**) 6 days of incubation at 30° C on micro-/anaerobic agar pads. Microcolonies rapidly grew between 2 and 6 days, with a rare case of one microcolony fully encircling a particle, even where no significant growth was visible at 2 days (although slight growth was visible at 1 day of growth). Microcolonies visible after 6 days to be comprised of more than 1 layer of cells, they can also be comprised of agglomerates of multiple early growth (1 or 2 days) microcolonies. Microcolony growth tends to follow the iron particle edge. Bright areas around object edges are an artefact of phase-contrast microscopy . Scalebar equals 100 µm, white arrows indicate visible microcolony growth when compared to the particle after 0 days of growth.

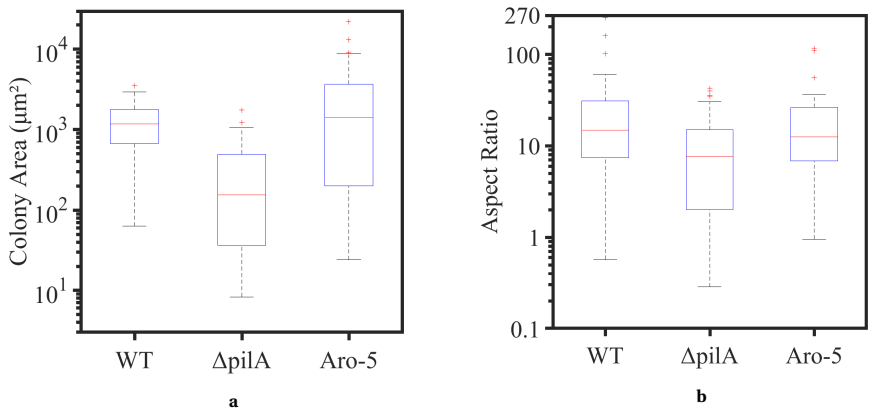

Figure 2.16: Comparison of microcolony area (**a**) and aspect ratio (**b**) of wild type, a strain producing no pili (ΔpilA) and a strain producing poorly conductive pili (Aro-5). There is no significant difference in distribution between wild type and Aro-5 microcolonies, both in area and aspect ratio. The distribution for ΔpilA microcolony area was significantly different from wild type, while the aspect ratio was not. As such all strains, despite differences in pili production and conductivity, are all similarly elongated along the iron particles. In contrast, ΔpilA microcolonies were significantly smaller, indicating at least a negative effect on growth due to the absence of pili.

confirmed its ability to do so, we must now investigate whether it can do so reliably. To investigate the reproducibility of the observed growth from pad to pad we expanded our dataset to two more pads of each strain, to a total of three pads per strain. The pads described above are called pad 1 for each strain, while the additional pads are termed pad 2 and 3. For each additional pad we selected 17 microcolonies from across at least 4 locations.

For wild type, pad 2 and 3 had a median area of 138 μm^2 and 2045 μm^2 respectively, comparing the distribution of values to that of pad 1 with a median of 1167 μm^2 shows a significant difference from pad 1 for both pad 2 and 3 (Kolmogorov-Smirnov test, D = 0.84 and D = 0.45 for pad 2 and 3 respectively, $p < 0.025$ for both). For ΔpilA the medians of both pad 2 and 3 were higher than the 154 μm^2 of pad 1, with 330 μm^2 and 2511 μm^2 respectively, and the distributions of both pad 2 and 3 were significantly different from pad 1 (Kolmogorov-Smirnov test, D = 0.37 and D = 0.89 for pad 2 and 3 respectively, $p < 0.025$ for both). Finally, for Aro-5 the medians of pad 2 and 3 were 2432 and 3300 μm^2 compared to 1393 μm^2 for pad 1, but only pad 2 was significantly different from pad 1 (Kolmogorov-Smirnov test, D = 0.52, $p < 0.025$ for pad 2 and D = 0.27 with $p > 0.025$ for pad 3).

It appears that between-pad variation often results in significant differences in microcolony area, with only one pad of Aro-5 not significantly different from the pads described in detail earlier. However, despite the significant variation in microcolony area between pads, the effect of iron on microcolony shape persists. For each pad of every strain the median on-iron microcolony aspect ratio is above 7, as seen in figure 2.17, indicating elongated microcolonies in each case.

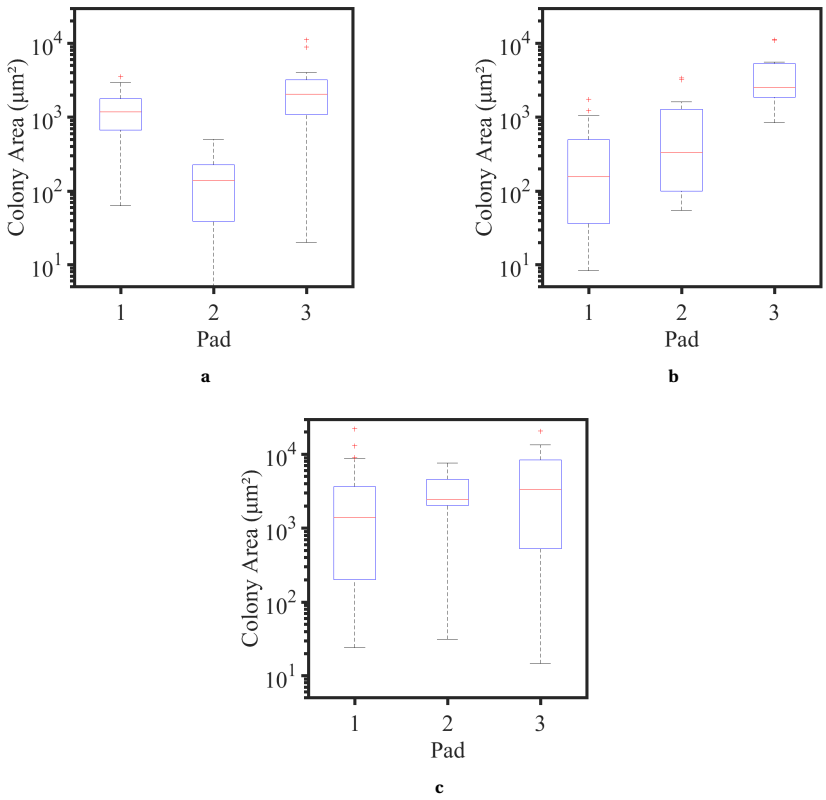

Figure 2.17: Variation in on-iron microcolony area between pads for wild type (WT, **a**), a strain producing no pili (ΔpilA, **b**) and a strain producing poorly conductive pili (Aro-5,**c**). For each strain pad 1 was described in detail with 24, 23 or 38 identified microcolonies for WT, ΔpilA and Aro-5 respectively, while pad 2 and 3 have 17 identified microcolonies for each strain. Every pad 2 and 3 was significantly different from the corresponding pad 1, except for pad 3 of Aro-5 ((Kolmogorov-Smirnov test, $D = 0.84$ and $D = 0.45$ for wild type pad 2 and 3 respectively, $p < 0.025$ for both, $D = 0.37$ and $D = 0.89$ for ΔpilA pad 2 and 3 respectively, $p < 0.025$ for both, and $D = 0.52$, $p < 0.025$ for pad 2 and $D = 0.27$ with $p > 0.025$ for pad 3). As such, there is significant variation in microcolony area from pad to pad, for each strain.

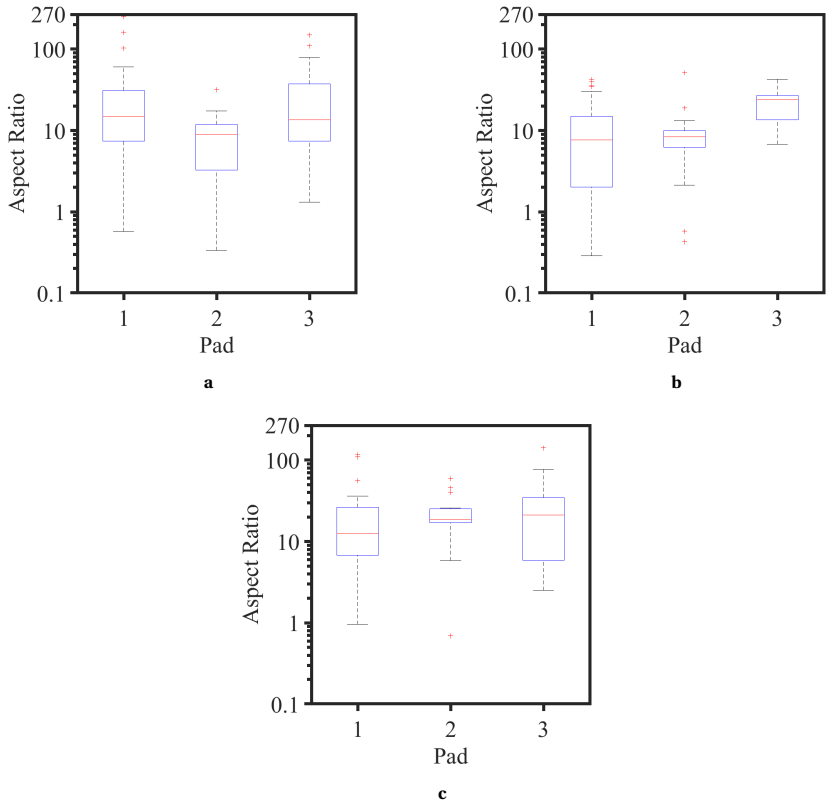

Figure 2.18: Variation in on-iron microcolony aspect ratio between pads for wild type (WT, **a**), a strain producing no pili (ΔpilA, **b**) and a strain producing poorly conductive pili (Aro-5,**c**). For each strain pad 1 was described in detail with 24, 23 or 38 identified microcolonies for WT, ΔpilA and Aro-5 respectively, while pad 2 and 3 have 17 identified microcolonies for each strain. In contrast to on-iron microcolony area, there was no significant difference in aspect ratio between pad 1 and pad 2 or 3 for wild type (Kolmogorov-Smirnov test, $D = 0.35$ and $D = 0.20$ for pad 2 and 3 respectively, $p > 0.05$ for both pads). For ΔpilA only pad 3 was significantly different from pad 1 (Kolmogorov-Smirnov test, $D = 0.22$ and $D = 0.55$, with $p < 0.01$ and $p > 0.05$ for pad 2 and 3 respectively), and for Aro-5 only pad 2 was significantly different from pad 1 (Kolmogorov-Smirnov test, $D = 0.43$ and $D = 0.28$, with $p < 0.025$ and $p > 0.05$ for pad 2 and 3 respectively). Microcolony aspect ratio remains above 7 for all pads, showing that on-iron microcolonies grow elongated along the iron particle regardless of pad to pad variation in microcolony area.

2.4 DISCUSSION

We have set up a method for growth of *G. sulfurreducens* cells on agar pads in the presence of iron particles to allow a microscopically observable situation where growth can depend on conductivity. The method needed to provide microscopic observation and spatial characterization of 2D growth of *G. sulfurreducens* single cells over a time period long enough for multilayered colonies to form on iron particles in an environment with minimal oxygen.

MICROSCOPIC OBSERVATION

Our method provided microscopic observation of microcolony growth on iron particles up to magnification of 40x. The 20x magnification we used provided sufficient resolution to distinguish on-iron microcolonies down to 8 μm^2 in size as well as off-iron single cells. Although a magnification of 20x was used to allow for full imaging of the pad, one can choose to use a 40x magnification to investigate particular regions of the pad. A magnification higher than 40x results in practical limitations since oil has to be used during imaging and afterwards the flow chamber has to be thoroughly cleaned from oil residue to not limit later imaging resolution. Touching the center of the flow chamber applies pressure to the agar pad which shifts the cells and particles. Cleaning the flow chamber without touching it is difficult which makes cleaning an extremely impractical step. As an alternative, one could install the full flow chamber setup at the microscope and leave the oil in contact with the chamber while limiting evaporation of oil or regularly replenishing oil, or employ a cleaning technique that does not involve touching the flow chamber. For our purposes of spatially characterizing microcolony growth the 40x magnification proved sufficient .

SPATIAL CHARACTERIZATION OF 2D GROWTH

Microcolonies were visible within two days and appeared to consist of a monolayer of cells. After six days of incubation the microcolonies appeared closely-packed and multilayered. The image analysis of the presented method resulted in edge selection of particles and microlonies. The edge characteristics were used to describe microcolony area as well as growth of the microcolonies along the edge of the iron particle.

With regards to microcolony area the on-iron and off-iron colonies differed in distribution although their median and range were similar. The on-iron colonies seemed to consist of a set of colonies smaller than 1000 μm^2 and a set of colonies larger than 1500 μm^2, while off-iron colonies appeared to consist of a single set centered around the median. To which extent these sets are due to physiological differences would require further investigation though they may signify the use of different electron acceptors, with use of one resulting in a higher growth rate than another. Upon onset of growth wild type microcolonies could continue to grow up to an area of 3526 μm^2 for the largest identified microcolony, with a median area of 1167 μm^2 . With the average imaged area of a single cell being 4.1 μm^2 the largest microcolony would correspond to an approximate minimum of 860 cells, and the median microcolony an approximate 284 cells. Considering that after six days of growth most microcolonies appeared to be multilayered, the actual number of cells is likely higher. With regards to elongation, the off-iron microcolonies typically grew into microcolonies with an aspect ratio close to one. This isotropic growth

is in contrast to the on-iron microcolonies whose length along the iron particle exceeded their width by one order of magnitude. Future research using our methods ability to describe microcolony shape could provide further insight into the causes of on-iron colony elongation. In addition to spatial characterization our method also allowed for temporal characterization.

TEMPORAL RESOLUTION

Experiments could last up to 6 days without desiccation of the pads. Microcolonies could be observed multiple times in this time interval, in our case after 0, 1, 2, or 6 days of incubation. The microcolonies continued to grow during this period. This temporal resolution allowed for the characterization of growth throughout time describing its exponential nature, varying growth rate and the presence of a lag phase. Confocal microscopy studies of early biofilm formation showed that ΔpilA had lower viability and produced smaller 3D protrusions from the biofilm[34]. This low viability may be reflected in the increased lag phase observed here. As the rise of single-cell investigations of microorganisms has shown, heterogeneity in cell division onset is not uncommon[35], although to the best of our knowledge it has not yet been reported for *G. sulfurreducens*. Having identified the phenomenon, future research could investigate relevant factors affecting the onset of growth. The possibly toxic influence of oxygen should then also be taken into account.

MINIMAL OXYGEN ENVIRONMENT

The method was able to provide a low oxygen environment, though its consistency needs to be improved. To assess the anaerobicity of the flow system we developed an oxygen assay using (2,2'-bipyridine) dichlororuthenium(II) ($Ru(bpy)_3^{2+}$) for agar pads which showed sensitivity for oxygen levels in agar pads similar to that in bulk assays. A quantitative calibration of the agar pad oxygen assay sensitivity would require a second independent agar pad assay. The fluorescence of oxygen-quenched dyes did indicate that oxygen levels in agar pads were similar to that of pads that were prepared in an anaerobic glove box and exposed to an oxygen scavenger in two cases, i.e. close to zero. However, in the third case oxygen concentration was around 10%. Exposure to oxygen concentrations higher than 5% is toxic[17] to *G. sulfurreducens*. Despite the occasionally high oxygen concentration microcolonies grew in all cases indicating that effective oxygen concentration during growth is lower than 10%.

It seems unlikely that oxygen concentrations were truly zero, since consistent growth of microcolonies not in contact with iron particles showed that some alternative dissolved electron acceptor was present, which we would expect to be low levels of oxygen. In previous reports microcolonies also grew in the absence of a carbon source[32] or electron acceptor[36]. As such, the microcolony growth despite lack of access to the insoluble electron acceptor is a limitation of the current method, though it may not be a unique limitation.

OUTLOOK

Even in the presence of oxygen the iron particle is likely to affect growth since it provides a secondary electron acceptor source. Iron as secondary electron acceptor becomes in-

creasingly relevant when local oxygen concentration becomes diffusion dependent and cells' access to iron remains while access to oxygen decreases. *G. sulfurreducens* is known to prefer Fe(III) reduction over fumarate as electron acceptor in the presence of both[37], although the same preference for Fe(III) in presence of oxygen has not yet been investigated. As such, presence of oxygen does not necessarily invalidate wire dependence of growth, although a minimized oxygen concentration remaines preferred.

The method described here was proposed as a way to study the impact of protein wire properties on early biofilm formation in order to identify avenues for future MFC engineering. However, before such investigations can be performed the method as is still needs to be improved. We observed significant between-pad variation within one strain and further improvements in reproducibility are required before specific conclusions on the effect of pili on microcolony area can be made. From analysis of the pad-to-pad variation in microcolony area for a single strain it is clear that even in a single batch of pads significant variation in microcolony area can occur. Imperfect division of gas flow or poor connection to the flow splitter may result in variations in flow along the pads. The variations in flow may explain the variations in measured oxygen concentrations in pads exposed tov that flow. This between pad variation severely limits our ability to draw conclusions from our exploratory data. It is advised that investigating the nature of the variation and ensuring equal flow distribution are the first improvements to be made to the method.

Although specific conclusions are limited with the method at its current stage, general insight was gained into the range of microcolony area, growth rate and shape on iron particles. The range of microcolony sizes can be used as a reference point for future studies, while studies on microcolony structure and dependence on pili are likely to benefit from the characterization of microcolony shape rather than size. This method has the ability to characterize growth of microcolonies in an environment with minimal oxygen over several days, thus allowing imaging of two-dimensional colony characteristics for investigation of spatial patterns of growth and its dependence on proximity to an iron particle.

REFERENCES

[1] O. Guadarrama-Pérez, A. Carolina Guevara-Pérez, V. Hugo Guadarrama-Pérez, V. Bustos-Terrones, J. Hernández-Romano, R. Angélica Guillén- Garcés, and G. Eleonora Moeller-Chávez, *Bioelectricity production from the anodic inoculation of Geobacter sulfurreducens DL-1 bacteria in constructed wetlands-microbial fuel cells,* Bioelectrochemistry **154** (2023), 10.1016/j.bioelechem.2023.108537.

[2] I. Ochiai, T. Harada, S. Jomori, A. Kouzuma, and K. Watanabe, *Bioaugmentation of microbial electrolysis cells with Geobacter sulfurreducens YM18 for enhanced hydrogen production from starch,* Bioresource Technology **386**, 129508 (2023).

[3] A. E. Franks and K. P. Nevin, *Microbial fuel cells, a current review,* Energies **3**, 899 (2010).

[4] P. Mukherjee, S. Pichiah, G. Packirisamy, and M. Jang, *Biocatalyst physiology and interplay: a protagonist of MFC operation,* Environmental Science and Pollution Research **28**, 43217 (2021).

[5] Z. M. Summers, H. E. Fogarty, C. Leang, A. E. Franks, N. S. Malvankar, and D. R. Lovley, *Direct exchange of electrons within aggregates of an evolved syntrophic coculture of anaerobic bacteria.* Science (New York, N.Y.) **330**, 1413 (2010).

[6] P. S. Bonanni, G. D. Schrott, and J. P. Busalmen, *A long way to the electrode: how do Geobacter cells transport their electrons?* Biochemical Society transactions **40**, 1274 (2012).

[7] L. Robuschi, J. P. Tomba, G. D. Schrott, P. S. Bonanni, P. M. Desimone, and J. P. Busalmen, *Spectroscopic slicing to reveal internal redox gradients in electricity-producing biofilms.* Angewandte Chemie (International ed. in English) **52**, 925 (2013).

[8] D. Filman, S. Marino, J. Ward, L. Yang, Z. Mester, E. Bullitt, D. Lovley, and M. Strauss, *Structure of a cytochrome-based bacterial nanowire,* bioRxiv , 492645 (2018).

[9] N. S. Malvankar, M. T. Tuominen, and D. R. Lovley, *Biofilm conductivity is a decisive variable for high-current-density Geobacter sulfurreducens microbial fuel cells,* Energy & Environmental Science **5**, 5790 (2012).

[10] L. Craig, N. Volkmann, A. S. Arvai, M. E. Pique, M. Yeager, E. H. Egelman, and J. a. Tainer, *Type IV pilus structure by cryo-electron microscopy and crystallography: implications for pilus assembly and functions.* Molecular cell **23**, 651 (2006).

[11] G. T. Feliciano, G. Reguera, and E. Artacho, *Molecular and Electronic Structure of the Peptide Subunit of Geobacter sulf urreducens Conductive Pili from First Principles,* Journal of Physical Chemistry B **116**, 8023 (2012).

[12] L. V. Richter, S. J. Sandler, and R. M. Weis, *Two isoforms of Geobacter sulfurreducens PilA have distinct roles in pilus biogenesis, cytochrome localization, extracellular electron transfer, and biofilm formation.* Journal of bacteriology **194**, 2551 (2012).

[13] Y. Ye, X. Liu, K. H. Nealson, C. Rensing, S. Qin, and S. Zhou, *Dissecting the Structural and Conductive Functions of,* mBio **13**, 1 (2022).

[14] M. C. Duvernoy, T. Mora, M. Ardré, V. Croquette, D. Bensimon, C. Quilliet, J. M. Ghigo, M. Balland, C. Beloin, S. Lecuyer, and N. Desprat, *Asymmetric adhesion of rod-shaped bacteria controls microcolony morphogenesis,* Nature Communications **9**, 25 (2018).

[15] R. Y. Adhikari, N. S. Malvankar, M. T. Tuominen, and D. R. Lovley, *Conductivity of individual Geobacter pili,* RSC Adv. **6**, 8354 (2016).

[16] A. Ducret, E. Maisonneuve, P. Notareschi, A. Grossi, T. Mignot, and S. Dukan, *A microscope automated fluidic system to study bacterial processes in real time.* PloS one **4**, e7282 (2009).

[17] W. C. Lin, M. V. Coppi, and D. R. Lovley, *Geobacter sulfurreducens Can Grow with Oxygen as a Terminal Electron Acceptor,* Applied and environmental microbiology **70**, 2525 (2004).

[18] C. E. Engel, D. Vorländer, R. Biedendieck, R. Krull, and K. Dohnt, *Quantification of microaerobic growth of Geobacter sulfurreducens,* bioRxiv , 1 (2019).

[19] A. Fievet, A. Ducret, T. Mignot, O. Valette, L. Robert, R. Pardoux, A. R. Dolla, and C. Aubert, *Single-cell analysis of growth and cell division of the anaerobe Desulfovibrio vulgaris hildenborough,* Frontiers in Microbiology **6**, 1 (2015).

[20] A. E. Franks, R. H. Glaven, and D. R. Lovley, *Real-time spatial gene expression analysis within current-producing biofilms.* ChemSusChem **5**, 1092 (2012).

[21] H. Zheng and Y. Zu, *Emission of tris(2,2'-bipyridine)ruthenium(II) by coreactant electrogenerated chemiluminescence: From O2-insensitive to highly O2-sensitive,* Journal of Physical Chemistry B **109**, 12049 (2005).

[22] M. G. Sasso, F. H. Quina, and E. J. H. Bechara, *Ruthenium(II) Tris(bipyridyl) Ion as a Luminescent Probe for Oxygen Uptake,* Analytical biochemistry **156**, 239 (1986).

[23] D. M. Benson, J. A. Knopp, and I. S. Longmuir, *Intracellular oxygen measurements of mouse liver cells using quantitative fluorescence video microscopy,* BBA - Bioenergetics **591**, 187 (1980).

[24] L. Ma, J. Yi, N. Wisuthiphaet, M. Earles, and N. Nitin, *Accelerating the Detection of Bacteria in Food Using Artificial Intelligence and Optical Imaging,* Applied and Environmental Microbiology **89**, 1 (2023).

[25] Y. Cao, J. Neu, A. E. Blanchard, T. Lu, and L. You, *Repulsive expansion dynamics in colony growth and gene expression,* PLoS Computational Biology **17**, 1 (2021).

[26] K. S. Korolev, M. J. Müller, N. Karahan, A. W. Murray, O. Hallatschek, and D. R. Nelson, *Selective sweeps in growing microbial colonies,* Physical Biology **9** (2012), 10.1088/1478-3975/9/2/026008, arXiv:1204.4896 .

[27] J. Nijjer, C. Li, Q. Zhang, H. Lu, S. Zhang, and J. Yan, *Mechanical forces drive a reorientation cascade leading to biofilm self-patterning,* Nature Communications **12** (2021), 10.1038/s41467-021-26869-6.

[28] X. Jiang, J. Hu, E. R. Petersen, L. a. Fitzgerald, C. S. Jackan, A. M. Lieber, B. R. Ringeisen, C. M. Lieber, and J. C. Biffinger, *Probing single- to multi-cell level charge transport in Geobacter sulfurreducens DL-1.* Nature communications **4**, 2751 (2013).

[29] G. Reguera, K. D. McCarthy, T. Mehta, J. S. Nicoll, M. T. Tuominen, and D. R. Lovley, *Extracellular electron transfer via microbial nanowires.* Nature **435**, 1098 (2005).

[30] D. R. Lovley and E. J. Phillips, *Organic matter mineralization with reduction of ferric iron in anaerobic sediments.* Applied and environmental microbiology **51**, 683 (1986).

[31] O. Oter and A. C. Ribou, *Quenching of long lifetime emitting fluorophores with paramagnetic molecules,* Journal of Fluorescence **19**, 389 (2009).

[32] A. M. Speers and G. Reguera, *Electron donors supporting growth and electroactivity of Geobacter sulfurreducens anode biofilms.* Applied and environmental microbiology **78**, 437 (2012).

[33] D. E. Holmes, L. Giloteaux, M. Barlett, M. A. Chavan, J. A. Smith, K. H. Williams, M. Wilkins, P. Long, and D. R. Lovley, *Molecular analysis of the In situ growth rates of subsurface geobacter species,* Applied and Environmental Microbiology **79**, 1646 (2013).

[34] G. Reguera, K. P. Nevin, J. S. Nicoll, S. F. Covalla, T. L. Woodard, and D. R. Lovley, *Biofilm and nanowire production leads to increased current in Geobacter sulfurreducens fuel cells.* Applied and environmental microbiology **72**, 7345 (2006).

[35] S. F. Levy, N. Ziv, and M. L. Siegal, *Bet hedging in yeast by heterogeneous, age-correlated expression of a stress protectant,* PLoS Biology **10** (2012), 10.1371/journal.pbio.1001325.

[36] G. Reguera, R. B. Pollina, J. S. Nicoll, and D. R. Lovley, *Possible nonconductive role of Geobacter sulfurreducens pilus nanowires in biofilm formation.* Journal of bacteriology **189**, 2125 (2007).

[37] A. Esteve-Núñez, C. Núñez, and D. R. Lovley, *Preferential Reduction of Fe(III) over Fumarate by Geobacter sulfurreducens,* Journal of Bacteriology **186**, 2897 (2004).

3

MEASURING ELECTRICAL PROPERTIES OF SINGLE CONDUCTIVE PROTEIN WIRES

Using a stochastic deposition method, passive voltage imaging and atomic force microscopy we visually confirm and make electrical contact with single nanowires. We describe optimization of the sample preparation and chip design showing that chemically untreated samples performed best, while an interdigitated chip design improved the chances of making contact. Ultimately we demonstrate the ability to manipulate temperature providing valuable characterization of the temperature-dependence of nanowires conductivity.

Chips manufactured by Nandini Muthusubramian and Jacqueline A. Labra Muñoz.

3.1 INTRODUCTION

Exoelectrogenic bacteria export electrons to extracellular electron acceptors, effectively generating a current. The biofilm of one such exoelectrogenic bacterium *G. sulfurreducens* was shown[1] to conduct around 2 μA at 0.2 V corresponding to a conductance of 5 μS. Between -0.4 V and +0.4 V there even was a linear dependence of current on applied bias voltage, sparking discussion of an electron transport mechanism similar to metallic conductance[2]. In order to investigate any claims on electron transport the conducting element had to be identified first. The observed conductance persisted while flushing media, excluding diffusive processes such as ionic currents or redox shuttles. Upon closer investigation the presence of wire networks between cells were identified[1]. Measurements[3] of the wire networks in which cytochromes were denatured resulted in measured conductivities of 6 μS/cm . In 2015 Adhikari *et al.*[4] were able to measure conductivity across an isolated single wire. These measurements again showed a linear relationship between -0.4 V and + 0.4 V but with even higher conductivity of 51 mS/cm. Having confirmed single wire conductivity, further investigations into the characteristics of electron transport mechanism were conducted. However, a reliable method for contacting single wires and measuring under a wide range of conditions proved to be lacking.

The primary methods used in investigations[4–6] are a custom-made "Low-noise Nanoelectrode Measurement Platform" (LNMP), Conductive Probe Atomic Force Microscopy (CP-AFM), and Scanning Tunneling Microscopy (STM). Each method has its strengths and weaknesses and they are best used in conjuction in order to gain a full characterization of the electron transport mechanism. The LNMP allows for stable high-resolution current measurements[4], CP-AFM is excellent in providing distance dependence measurements, and STM can be used to probe the density of states along a wire, even at various temperatures (as demonstrated by Lampa-pastirk *et al.*[5]). On the other hand, CP-AFM is limited in its environmental control and can only measure one wire at a time, STM was only demonstrated for transaxial measurements, and the LNMP was not demonstrated to possess any environmental control. The ability to control environmental parameters such as atmosphere, temperature and illumination is crucial for a full characterization of electron transport through the wire.

We describe here in detail the design of a method able to perform these measurements. Our results include high-resolution current measurements, temperature control, atmosphere control and investigation of back-gate effects as proof-of-principle. Additionally we describe design changes that could allow for measurements of distance dependence and note the easily implementable option of illumination. In order to provide others the option to adjust this method to their own studies we include the design considerations and results of adjusting various parameters. The method section of this chapter is positioned at the end to serve as summary of the designed method. Ultimately, the adaptability of the method is further demonstrated in chapter 4 and chapter 5 by measuring conductivity of two different types of biowires.

3.2 RESULTS

WIRE DEPOSITION

To perform a variety of measurements on the same wire in various conditions we require a stable sample with a long degradation time. To create such a stable sample, the wires are allowed to adsorb to a surface. Proteins adsorbed to a surface are known[7] to be stable, maintaining structure and even catalytic function at temperatures up to 100°C.

The type of surface will determine the type of measurements that can be performed. Mica is an accessible substrate for making atomically flat sheets, allowing for optimal topography studies using AFM. However, it is non-conductive, limiting conductivity investigations. Highly Oriented Pyrolithic Graphite is an atomically flat conductive substrate which allows for transaxial measurements of conductance using CP-AFM. A silicon-oxide surface allows for the deposition of gold layers, either before or after wire deposition, allowing advanced designs for combinations of non-conductive and conductive surfaces in various topologies. Additionally, p-doped silicon is conductive beneath the silicon-oxide surface, allowing for the investigation of field effects by applying a back-gate voltage.

STANDARD PROTOCOL

At time of development the protocols for isolation of *G. sulfurreducens* wire extracts were based on pili purification protocols for *Neisseria meningitidis*[8]and *Pseudomonas syringae*[9]. We based our standard protocol for sample preparation on these protocols, the details of which are described in section 3.4. In short, the standard protocol consisted of the following steps: A cell culture was centrifuged after which the pellet was resuspended in ethanolamine buffer at pH 10.5. Then cells were sheared by repeated passes through a needle, after which the cells were vortexed, releasing the wires from the cells. This solution was centrifuged again, this time keeping the supernatant. To concentrate the sample and separate the wires from smaller proteins the supernatant was exposed to an ultracentrifugation step. The supernatant was removed and the pellet resuspended, aliquots were subsequently flash frozen with liquid nitrogen. For deposition one such aliquot was allowed to melt after which 1 µl droplets were deposited on each device, left to adsorb for 20 minutes, after which the sample was blown dry with an air gun.

SUBSTRATES

As described above, the surface material affects resolution of topological investigations and the ability to investigate conductivity. To enable investigations of both topology and conductivity, wires are deposited on Mica, HOPG, SiO_2 and SiO_2 with Au surfaces (chips) . As can be seen in the AFM images in figure 3.1 each of the substrates shows separate wires typically 1 µm long and 2 to 4 nm wide.

These dimensions correspond well with those reported in literature and the theoretical width of the wires based on low-energy atomic modeling[10]. The wires were not seen in samples prepared from cultures of mutants in which the gene encoding the pilA protein is disabled. As such we have established deposition on various experimentally relevant substrates. Notably, deposition on SiO_2 with Au was achieved, which could facilitate cisaxial conductance measurements. Such measurements could be performed

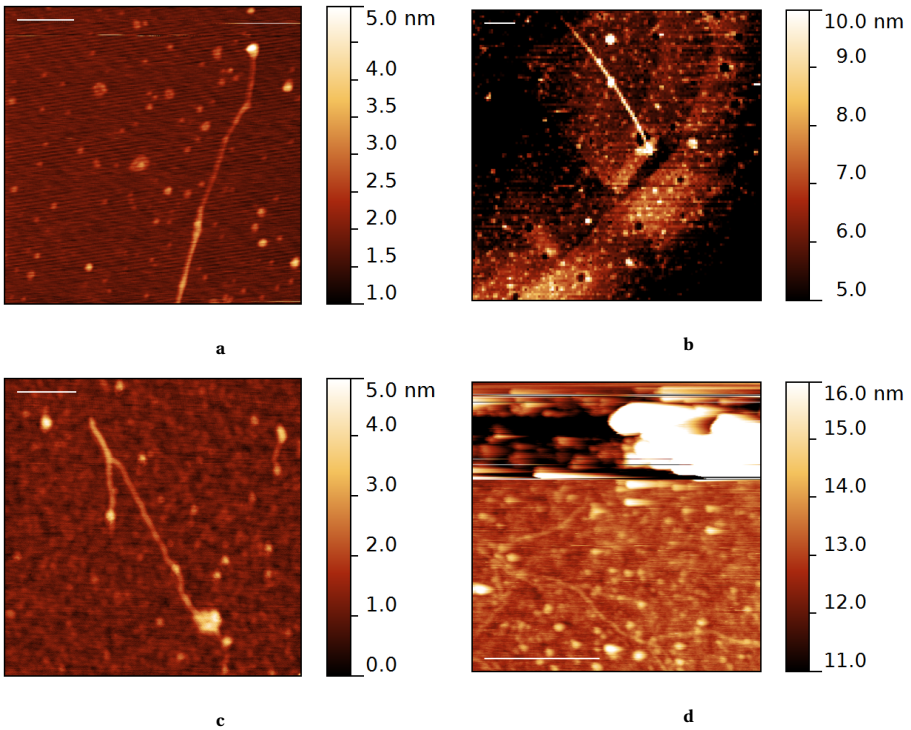

Figure 3.1: An extracellular protein extract containing wires from *G. sulfurreducens* was deposited on four different types of surfaces. Using Atomic Force Microscopy each surface was shown to adsorb wires contained in the extract, although visibility varies depending on surface roughness. Each surface is suited for different types of investigation. **a** Mica is an atomically flat surface that does not conduct. **b** Highly Oriented Pyrolithic Graphite (HOPG) is an atomically flat surface that does conduct. **c** Silicon-oxide wafers can be modified with a variety of metals, and p-doped silicon contains a conductive inner layer which can be used for applying a back-gate. **d** Chips made of gold layered on silicon-oxide wafers allow for custom designed gold surfaces, in this case used to facilitate electrical contact with the wires.

by depositing wire on chips, with the particular chip design determining the measurement conditions and limitations. We will now discuss the design of those chips.

CHIP DESIGN

The chip design should include a non-conductive gap between two gold surfaces, which a deposited wire can bridge, resulting in a electrical connection between the gold surfaces. Based on reported values the conductivity of a single wire is assumed to be less than the gold surface. The conductivity of the connection is then determined by the wire and its contact with the gold. Each patch of gold should then in turn be connected to a patch of gold large enough to make contact with a mechanical probe. To reliably contact the gold with the mechanical probe a 200 × 200 µm gold square called a "(contact) pad" is needed. The rest of the design depends on the approach for having a wire cross the gap.

Wires might be physically manipulated and placed across the gaps, or wires could be deposited at random locations with a certain fraction bridging a gap by chance. Given the difficulty of manipulating nanometer-wide wires while maintaining wire integrity we instead decided to optimize the chance of wires bridging a gap upon deposition. We deposited an extracellular wire-containing extract on multiple gaps and relied on the probability that one of the wires happens to bridge the gap and make electrical contact. Once the gap is electrically bridged by a wire we can apply a bias across the gap and measure the current through the wire.

To apply a bias across the gap each side of the gap is associated with a different contact pad, as can be seen in the schematic chip layout in figure 3.3. One side is connected to the main contact pad, while the other side is connected to a side pad. We then apply a bias between the main and corresponding side pad, resulting in a bias across the gap and allowing us to measure the current across the probes. We perform this measurement for each of the side pads until a level of current significantly higher than the noise level is detected, a process here called "connection finding". Once we have found a bridged gap, we can move to identification of the bridging element (the "connection").

We topologically identify the connection to confirm that it corresponds to a wire by imaging the entire potential contact area using Atomic Force Microscopy (AFM). In contrast to the report by Adhikari *et al.*[4] we did not experience that the presence of a wire bridging a gap guarantees a detectable current, or that the conducting elements were certain to be wires. It seems that either a certain fraction of the deposited wires are non-conductive or that these do not make a proper electrical contact with the gold.

Other conducting elements than wires were identified as can be seen in figure 3.2. Given the topology reflecting an agglomerate of bulbous structures we presumed these conducting elements to be protein aggregates possibly containing wires or a high density of cytochromes. Protein aggregates can form or deposit in the gaps and in the case where both a wire and aggregate are bridging a gap the possibility that the aggregate is responsible for the conductance can not be excluded. In the case that only an aggregate is bridging the gap we are unable to ascertain whether that aggregate contains a wire or that the aggregate conducts due to other unknown factors. As such, it is imperative to locate any and all particles bridging the gap and confirm their identity and responsibility for the observed conductance, this process is here called "connection identification".

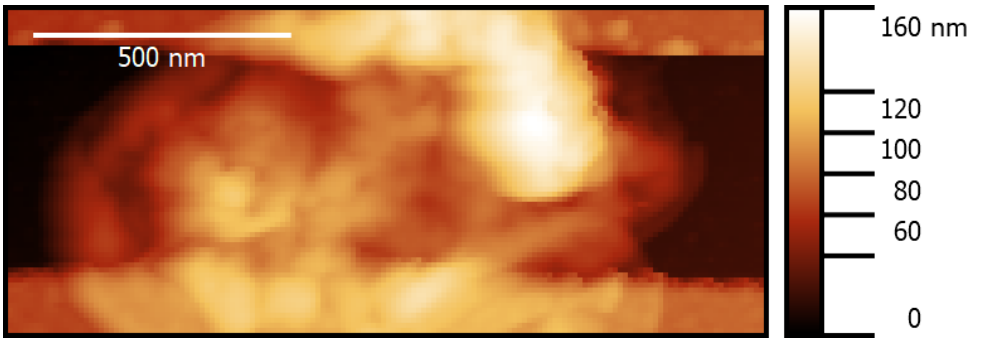

Figure 3.2: Atomic Force Microscopy image of an aggregate that was shown to conduct currents above noise level. Top and bottom sections are gold, aggregate is bridging the 500 nm gap between the gold. Connection identification is crucial to determine whether measurements are performed on a single wire, or on an aggregate of several proteins, possibly containing a wire.

The combined process of connection finding and connection identification is laborious and time-consuming. As such the minimization of non-wire bridging elements is crucial for achieving a practical method for contacting single wires. This chapter focuses on various efforts aimed towards optimizing the probability of having a connection consisting of only wires bridging the gap (an "only-wire connection"). Additionally we ease and accelerate the gap-finding and connection identification processes. First, we will discuss how the chips were designed with these factors in mind, while noting trade-offs in chip design due to this focus.

To start, we can minimize the number of non-wire bridging elements by choosing an appropriate gap size. The wire extract contains an abundance of proteins, but only few are large enough to match the length of a wire. With a 500 nm gap only the wires, large protein aggregates and debris are able to form a bridge. Thus one can exclude the many other single proteins present in the sample. It should be noted that one could instead choose a variety of gap sizes to investigate distance dependence. However, both increasing and decreasing gap size affects the probability of having an only-wire connection. A smaller gap size increases the probability of aggregates or even single proteins bridging the gap. A larger gap size reduces the probability of any bridging element, including wires. Although gap size is the only factor directly affecting the probability of having an only-wire connection, the chip layout can affect the gap-finding and connection identification as well. Ultimately, we employed three additional designs meant to optimize these two processes.

CHIP CONFIGURATION

We employed four different chip designs, varying in configuration of the lead and main electrodes. The first design depicted in figure 3.3 served as a proof-of-principle device (Device 1). It consisted of a main electrode of 0.1 × 2.2mm flanked by lead electrodes of 20 × 80 µm, resulting in several 0.5 × 20 µm gaps. With this proof-of-principle device we confirmed that in one of the electrical contacts the only bridging element between main and lead electrodes was a single wire. That sample was damaged in operation before a

thorough characterization could occur but it did show the potential of the method. With that potential in mind we first need to minimize the labor involved in finding a wire. The apparent low probability of any gap being bridged results in a low probability of any probe manipulation making contact with a bridged gap.

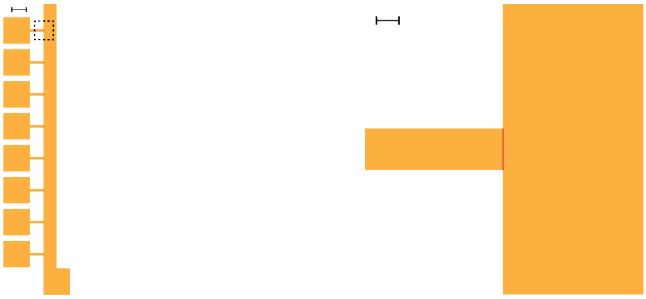

Figure 3.3: Schematic of chip design 1 employed for deposition and adsorption of wires resulting in an electrical connection that can be contacted by probes in a probe station. The overall device architecture (**a**) consists of a single long electrode flanked by smaller electrodes. The L-shaped area ('main lead') ends in a square ('main pad') which is contacted by a mechanical probe. Each square on the side ('side pads') is then contacted in turn by another mechanical probe, applying a bias voltage in order to measure the current between them. The current would be limited by any conductive elements bridging an insulating 500 nm SiO_2 gap in the potential contact area (dashed square, detail shown in **b**). Gold is depicted in yellow, scale bars are 100 µm and 10 µm for overall device architecture or potential contact area respectively, gap is indicated in red.

Increasing the number of gaps connected to each pad will increase the probability of finding a bridged gap per probe manipulation. We increased the number of gaps corresponding to a pad in two ways. In one design (Device 2) depicted in figure 3.4a we used an array of pads, each of which had two lead electrodes (5 × 80 µm) on the right side, one lead electrode on the top and bottom side, and one extending lead electrode (5 × 200 µm) on the left side. In this device each side of the pad could be connected to a neighbouring pad, while the extended lead allowed for diagonal contact, further maximizing the number of possible connections.

The other design used to increase the number of gaps per pad (Device 3) used a chip structure similar to device 1. However, instead of one gap per side pad the device 3 depicted in figure 3.4b employed an interdigitated design with two sets of ten "fingers", with each set connected via a lead electrode to either the main lead (the "main fingers") or the side pad (the "side fingers"). This results in twenty gaps per side pad, thus twenty times the probability of finding a connection per probe manipulation, as well as increasing gap density per chip, reducing the number of required chips and the associated fabrication time and resources. This twenty-fold increase in probability has the trade-off of increasing the connection identification time, since all twenty gaps would need to be fully imaged. Note that even with this trade-off this design saves time. Although per found connection twenty probe manipulations are much faster than fully imaging twenty gaps, in practice one has to perform twenty probe manipulations for each potential connection, which in total is much slower than fully imaging twenty gaps.

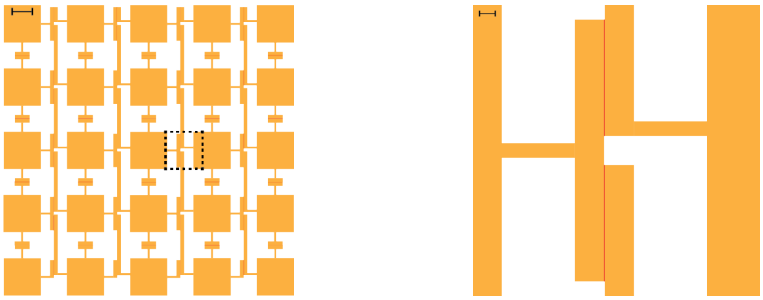

Figure 3.4: Schematic of chip design 2 employed for deposition and adsorption of wires resulting in an electrical connection that can be contacted by probes in a probe station. The overall device architecture (**a**) consists of an array of square pads flanked on four sides by smaller electrodes. Each pad can be contacted by a mechanical probe, upon which another probe would be used to contact any neighbouring pad (including diagonal neighbors). By applying a bias voltage we can then measure the current between these two pads. The current would be limited by any conductive elements bridging an insulating 500 nm SiO_2 gap in the potential contact area (dashed square, detail shown in **b**). Gold is depicted in yellow, scale bars are 100 µm and 10 µm for overall device architecture or potential contact area respectively, gap is indicated in red.

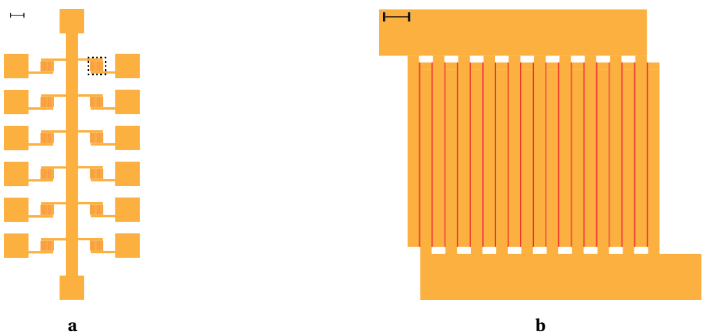

Figure 3.5: Schematic of chip design 3 employed for deposition and adsorption of wires resulting in an electrical connection that can be contacted by probes in a probe station. The overall device architecture (**a**) consists of an I-shaped area ('main lead') that ends in two squares ('main pads'), one of which is contacted by a mechanical probe. Each square on the side ('side pads') is then contacted in turn by another mechanical probe, applying a bias voltage in order to measure current between them. The current would be limited by any conductive elements bridging one or more of nineteen insulating gaps in an interdigitated potential contact area (dashed square, detail shown in **b**). The potential contact area consists of nineteen 500 nm gaps of SiO_2 between two sets of 10 fingers. One set of fingers is connected to a side pad, while the other set is connected to the main lead. Gold is depicted in yellow, scale bars are 100 µm and 10 µm for overall device architecture or potential contact area respectively, gap is indicated in red.

CHIP DESIGN FOR PASSIVE VOLTAGE CONTRAST IMAGING

We can further reduce the time required for imaging if we are quickly able to identify which of the "fingers" are connected to each-other by a conducting element. In that case it is not necessary to fully image all gaps, only the gap between connected fingers. Effectively this adds a second step to the connection-finding process. As long as this step is faster than fully imaging twenty gaps, it saves time. This second connection-finding step can be considered analogous to the common task of finding the location of a fault in a semiconductor device, in the sense that one is searching for a small electrical connection between chip elements at an unknown location. Therefore we explored techniques typically used for that purpose, and found Passive Voltage Contrast (PVC) imaging[11] to be an appropriate tool.

In PVC imaging the buildup of charge on the surface is inversely correlated to brightness when imaging with a Focused Ion Beam (FIB). In brief, the positive ion beam causes the surface to become positively charged except for areas where an electron sink is able to annul that charge (i.e. a grounded area). Any positively charged surface will attract the secondary electrons responsible for image intensity, preventing them from reaching the detector. In our case, if the main electrode were to be grounded there would be a large difference in charge build-up between fingers connected to the main pads and fingers connected to the side pad. On the fingers connected to the main pad any build-up of charge can flow away towards the ground, while charge would continue to build-up on fingers connected to the side pads unconnected to the ground. The fingers connected to the grounded main pad would then become bright, while those connected to the side pad would be dark. The exception occurs when fingers from the side pad set are connected via some conducting element to fingers connected to the main pad, in which case charge build-up on the side pad can also flow to the grounded main and would also appear bright. This principle is demonstrated in figure 3.6, in which only one the gold in contact with the grounded main gold is bright.

We used PVC imaging to identify which fingers are connected, as demonstrated in figure 3.6. First, the gold connecting each of the side fingers to the side pad is cut (the process of which is explained below), and the brightness of each finger then depends only on its connection to the main fingers. Only the connected side fingers are bright, which is particularly clear for the top finger which has some easily visible debris connecting it to the main fingers. Note that even poorly conductive materials (such as typical debris) can facilitate charge flow, and PVC is useful for identifying conductive elements, but not necessarily for discriminating between low or high conductivity of those elements.

The cuts between the connected side fingers are then restored (explained below) to still allow for electrical measurements, and now only the gaps between connected fingers are fully imaged with AFM as described previously. Finally, imaging with ions is a destructive technique, and imaging an area containing a wire is likely to degrade the wire. As such, all imaging is performed near the connections between fingers and leads, where there is a 5 μm gap unlikely to contain the connecting element.

The process of cutting and then restoring cuts between fingers and leads is performed by the FIB using ion beam milling followed by platinum deposition. The FIB can be used for milling away a strip of gold from the lead electrode, disrupting the contact to

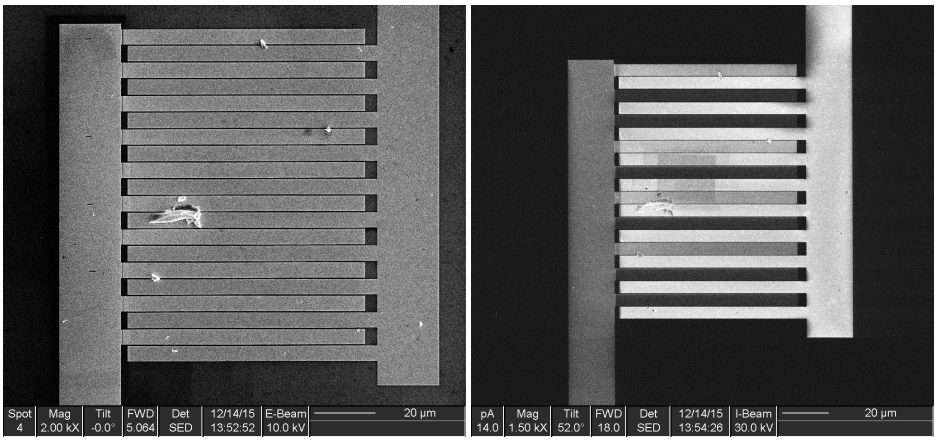

a **b**

Figure 3.6: Scanning Electron Microscopy (**a**) and Focused Ion Beam (**b**) micrographs of the same set of interdigitated electrodes. Passive Voltage Contrast Imaging was used to identify electrical connections between main and side pads. Imaging with a Focused Ion Beam (FIB) is particularly susceptible to charging effects, which can be used to identify in which imaged parts charge is able to flow to a ground. A grounded gold surface will allow charge to flow away from the surface to the ground, preventing charge build-up and maintaining a high intensity, while surfaces where charge can not flow to a ground will be darker (i.e. non-grounded surfaces). Here the right lead is connected to the main lead which is grounded, while the left lead is connected to a non-grounded side pad. As such, all main fingers are grounded. All connections from the side pad to the fingers have been cut via Focused Ion Beam milling, no charge can flow from side finger to side pad. The only option for charge to dissipate from the side fingers is if it is in electrical contact with the main fingers. While the cuts can be seen in a Scanning Electron Microscope image (**a**), the ability to dissipate charge is only clearly visible in the Focused Ion Beam image (**b**). Side fingers connected to main fingers via visible pieces of debris are brighter than those without a connection. The principle that connected fingers are bright can be used to identify the gaps potentially containing the electrically connecting elements, although care should be taken not to fully image the gap due to the destructive nature of FIB imaging. Note that non-connected side fingers are darker than the side pad. Charge on connected fingers can distribute itself over the relatively large side pad, resulting in their higher intensity.

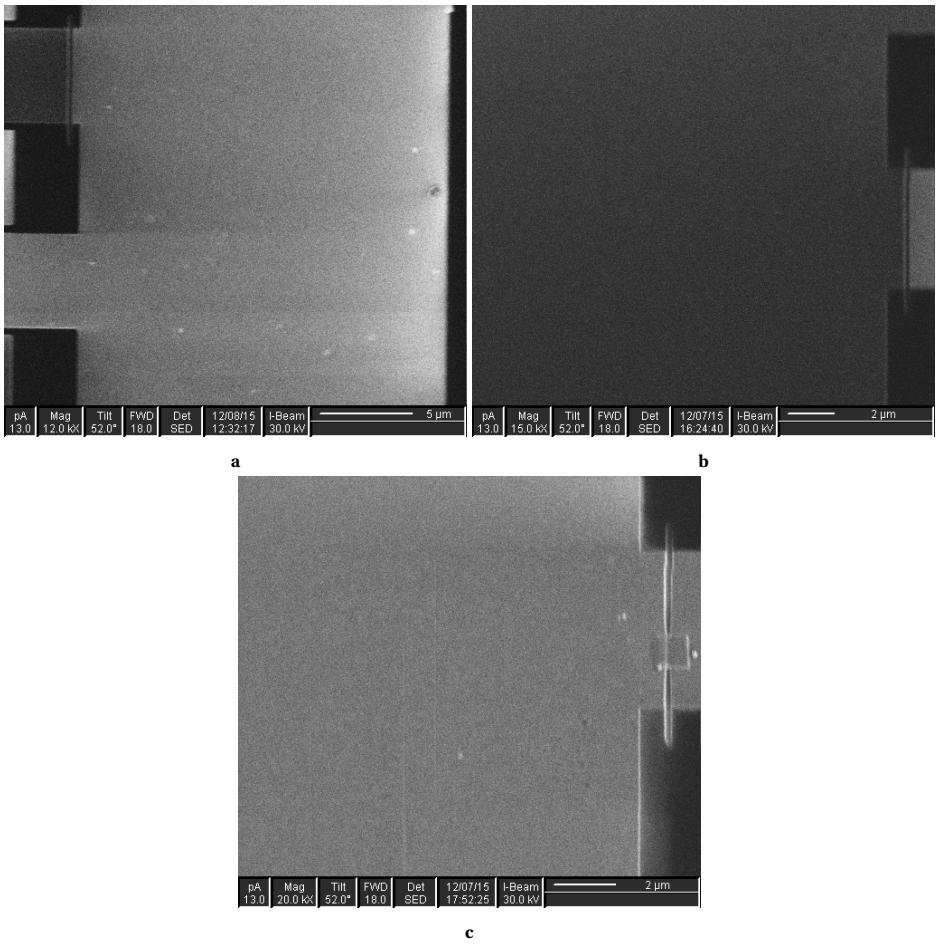

Figure 3.7: Connections between electrode "fingers" and their associated contact platform ("pad") can be disrupted ("cut") by Focused Ion Beam milling. By repeated exposure to an intense ion beam the gold is removed from a particular targeted strip, thus severing the connection between pad and finger. Cutting can be used in a case where the side pad is known to be connected to the main pad, but it is unknown through which gap and which associated finger. Upon cutting the connection between finger and pad, if the finger was connected it will remain bright, while if it was not it will turn dark (**a**). If the finger was solely responsible for the connection, the lead for the side pad will turn dark (**b**). When cutting a main finger the intensity change in its neighboring side fingers will indicate whether that particular main finger was responsible for the connection. After identification of the connecting fingers, the electrical connection between finger and lead can be restored via platinum deposition of a square of platinum contacting both sides of the cut (**c**).

the lead pad ("cutting"). Applying this to an interdigitated design allows one to cut each of the finger electrodes to see how it affects the brightness of the lead pad. Cutting a finger connected to the main electrode will cause the lead pad to turn dark, since charge can no longer disperse via the grounded main electrode, visible in figure 3.7a. Using FIB metal deposition one can then deposit a strip of platinum across the cut, depicted in figure 3.7c, restoring electrical connection to the lead pad. By repeating the same approach on the side of the main electrode, turning the finger dark as shown in figure 3.7b, we can determine a single gap as containing the bridging element.

The fourth design fully exploited the PVC imaging method of localization, skipping the need of a probe station for connection finding. In this design depicted in figure 3.8a ten grounded main electrodes are interdigitated with ten ungrounded main electrodes. Between each pair of main electrodes is a row of 5 × 5 µm squares separated from the main electrodes by 500 nm as can be seen in figure 3.8b.

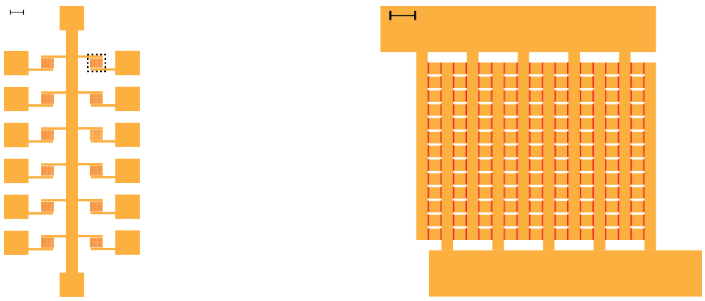

Figure 3.8: Schematic of chip design 4 employed for deposition and adsorption of wires resulting in an electrical connection that can be contacted by probes in a probe station. The overall device architecture (**a**) consists of an I-shaped area ('main lead') which ends in two squares ('main pads'), one of which is contacted by a mechanical probe. Each square on the side ('side pads') is then contacted in turn by another mechanical probe, applying a bias voltage in order to measure current between them. The current would be limited by any conductive elements bridging one or more of 338 short insulating gaps in an interdigitated potential contact area (dashed square, detail shown in **b**). Te potential contact area consists of 338 SiO_2 gaps of 5 µm long and 500 nm wide. The relatively large number of gaps is the result of 13 fingers, each almost connected by 13 gold squares of 5 × 5 µm ('spacers'), separated by a 500 nm gap above and below each spacer. One set of fingers is connected to a side pad, while the other set is connected to the main lead. Gold is depicted in yellow, scale bars are 100 µm and 10 µm for overall device architecture or potential contact area respectively, gap is indicated in red.

By imaging the center line of this row of squares one can immediately identify electrically connected squares since any small pad displaying a high intensity must be connected to a grounded main. The principle is illustrated in figure 3.9 where each of the bright squares is connected to the grounded main. The 0.5 × 5 µm gap is then rapidly imaged with AFM, and deposition of Pt can be used to connect a square of interest to an ungrounded main for I-V measurement.

CHIP DESIGN EVALUATION

Each of the four described devices takes a different approach towards locating a bridging wire and requires a different amount of effort, skills and techniques to be productive. Device 1 validated the effectiveness of the method and is easiest to fabricate, but the

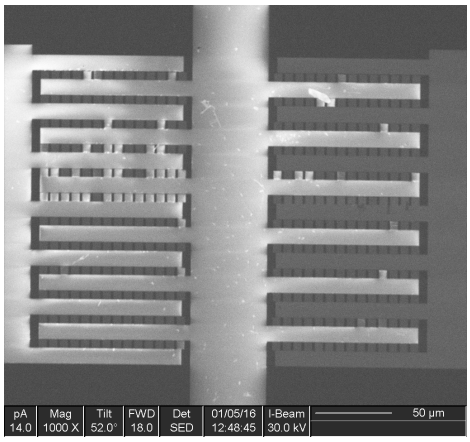

Figure 3.9: Focused Ion Beam micrograph of chip design 4, designed to employ exclusively Passive Voltage Contrast (PVC) imaging for finding a connecting element. Square spacers have large gaps between each-other, and a 5 µm long and 500 nm wide gap on their top and bottom side between them and the main or side fingers. The main fingers are grounded, and an electrical connection between one of the spacers and the main finger will result in a bright square when imaging with a Focused Ion Beam. Due to difficulties in fabrication here many spacers are connected, clearly demonstrating the effect. When a connected square is found, it can be connected to the side finger via platinum deposition on the opposite gap, after which the gap can be quickly imaged with Atomic Force Microscopy for connection identification, and the side and main pads connected to the side and main fingers can be contacted with a probe station.

probability of a connection and the speed of connection finding is lower than the other devices. Device 2 is an improvement in speed compared to device 1, but the large number of probe manipulations was slower than the process of PVC imaging used in Device 3. Device 4 was designed to capitalize on the speed advantage of PVC imaging but proved to be difficult to fabricate, and the precarious process of imaging the small squares without imaging their gaps limited its effectiveness in practice. As such, Device 3 has been chosen as the method for contacting and identifying nanowires between metallic electrodes.

SAMPLE PREPARATION

While chip design can improve workflow in handling and processing a sample, the content of that sample ultimately determines the probability of a connecting element being a wire. Due to the chip design only wires, debris and protein aggregates are able to bridge the gap. Debris tends to have poor conductivity thus limiting its negative effect to the PVC imaging step of connection finding. However, some aggregates bridging the gap were found to be able conduct currents high enough to be detected during the probe station step of connection finding. The conductivity of aggregates may be due to the aggregates containing cytochromes or wires. Preventing aggregation could increase the fraction of cases in which a large (>300 nm) particle is indeed a wire, here termed the "wire fraction". Additionally, fracturing wires by shearing can affect the number of wires able to bridge the gap, thus also increasing or decreasing the wire fraction. We explored various methods to affect average wire size and protein aggregation with the goal

of increasing the wire fraction.

SHEARING

In regards to wire size the main factor in our preparation method is a shearing step. Typically, the culture is sheared after vortexing in order to further detach wires from the cells before processing. In this step, the wires might also be fractured, thereby splitting a wire into smaller fragments. An initial shearing step may increase the number of wires long enough to bridge the gap, for example by fracturing one 5 µm wire into five wires of 1 µm), but a subsequent shearing step may then actually decrease that number, in this example by fracturing those 1 µm wires into five wires of 200 nm.

To assess the impact of shearing on the wire fraction we performed a deposition assay on sheared and unsheared wire extracts. This deposition assay consisted of depositing the wire extract on a chip after which a random 10 × 10 µm area was imaged with AFM and the number of particles larger than 300 nm were determined, as well as the fraction of those particles which that had filamentous topology ("wire fraction"). As can be seen in figure 3.10 the unsheared wire extracts actually resulted in a higher wire fraction than sheared wire extracts. As such, using unsheared samples is actually beneficial for achieving only-wire connections.

Second, we investigated various methods for reducing the number of aggregates. Aggregate formation may occur before or during deposition; to address both processes we explored the use of anti-aggregation compounds and variations in deposition and centrifugation time. We will first discuss the use of anti-aggregation compounds, which prevent protein aggregation or dissociate formed aggregates. Any addition of such compounds to the sample should be finely tuned, since too much of an anti-aggregation compound may cause the disassembly of wires into monomers, resulting in net fewer wires.

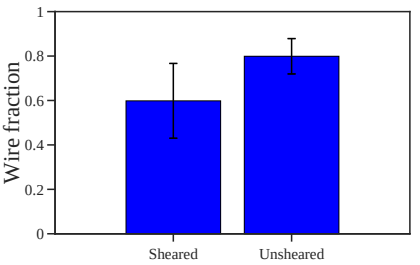

Figure 3.10: In the standard protocol for wire extraction and on-chip deposition the extracellular protein extract was exposed to a shearing step consisting of repeated passes through a 23G needle. The effect of shearing on the probability that a large (> 300 nm) particle is a wire was investigated. Wire fraction is defined as the fraction of large on-chip particles that have filamentous topology, as determined via Atomic Force Microscopy of three 10 × 10 µm surface areas of SiO_2. Unsheared samples had a larger wire fraction than sheared samples, thus standard protocol was adjusted to include no shearing.

ANTI-AGGREGATION COMPOUNDS

To prevent or reduce aggregation one can use a variety of compounds with different mechanisms, some of which remain poorly understood [12,13]. We performed a deposition

assay on one compound of five different mechanisms at three increasing concentrations that can be seen in figure 3.11 based on typical concentrations found in literature [14]. The compounds used were β-mercaptoethanol, Urea, NaCl, Glycerol and Tween, which affect disulfide bonds [15], hydration [16], ionic strength [17], protein stability [18] and hydrophobic/hydrophilic interactions [19] respectively. This deposition assay consisted of preparing an extracellular protein sample with the addition of the anti-aggregation compound in the final sample, followed by deposition on a chip. Following deposition, the wire fraction was determined as described for the shearing assay above. From the results of the initial exploration depicted in figures 3.11a and 3.11b we identified urea and β-mercapto-ethanol as promising candidates with which we repeated the deposition assay in triplicate (results of which are included in the data in figures 3.11a and 3.11b). Of these various treatments we determined that a concentration of 14.5 mM β-mercaptoethanol resulted in the highest wire fraction of 0.62 ± 0.05. However, that wire fraction is close to that of untreated samples, while β-mercaptoethanol can have significant effects on protein structure and influence interpretation of results.

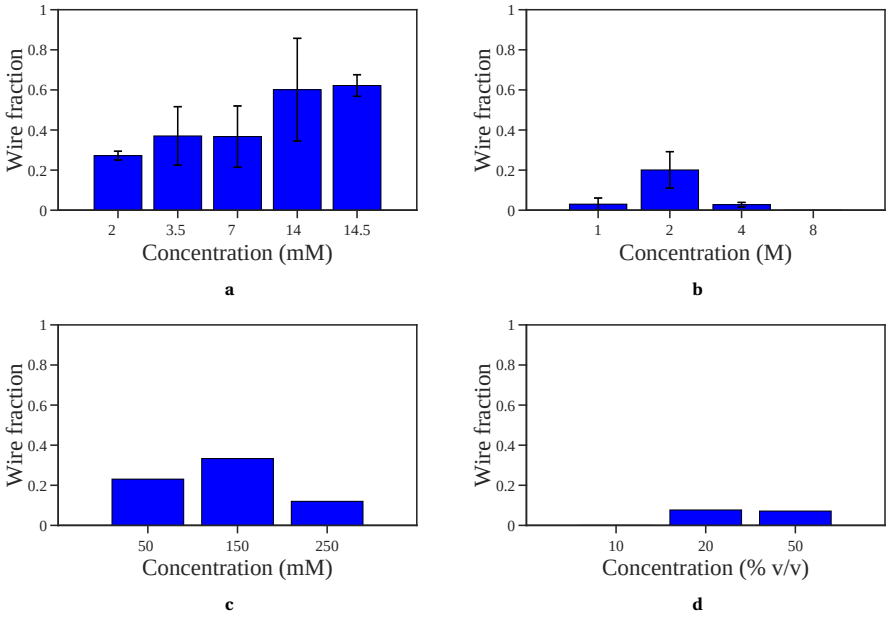

Figure 3.11: Upon on-chip deposition protein aggregates are visible as large (> 300 nm) particles which can cross the 500 nm gap used in measurements. To reduce the aggregate concentration or aggregate size various anti-aggregation compounds with differing anti-aggregation mechanisms were investigated. In a first exploration three different concentrations of (**a**) β-mercaptoethanol, (**b**) Urea, (**c**) NaCl and (**d**) Glycerol were added to the extracellular protein extract prior to deposition. After on-chip deposition their effect on the fraction of large particles that are wires ("wire fraction") was determined via Atomic Force Microscopy of three $10 \times 10 \mu m$ silicon areas. Promising candidates β-mercaptoethanol and Urea were investigated further in triplicate samples of various concentrations, as depicted with error bars of the standard error of the mean. No column means no wires were observed at that concentration. The anti-aggregation compound Tween was also explored at concentrations of 0.001, 0.002 and 0.005 v/v %, but no wires were observed in any of the imaged areas. β-mercaptoethanol showed the highest wire fraction.

CENTRIFUGATION AND DEPOSITION TIME

Besides adding anti-aggregation compounds it might be possible to reduce aggregation by varying deposition time. Formation of aggregates during deposition may occur via successive adsorption of proteins to other adsorbed proteins, perhaps even by preferential adsorption to a protein surface rather than to a gold or silicon-oxide surface. Reducing the deposition time may therefore limit the extent of aggregate formation. On the other hand, the number of adsorbed wires may also decrease with shorter deposition times if less wires have the chance to interact with and adsorb to the surface. Ultimately we tested four different deposition times (1, 5, 10 and 20 minutes). For each of these conditions the wire fraction was determined, and as can be seen in figure 3.12a the wire fraction for a 5 minute deposition was similar to that of a 20 minute deposition.

Finally, aggregation can occur due to interactions between single proteins, each of which is only up to a few nanometer in size, or polymers such as the wires themselves which can range up to micrometers in length. Before aggregation occurs there is a large difference between the dimensions of the wires and the dimensions of the single proteins that could aggregate. Separation of those small proteins from the relatively large wires could diminish later aggregation. Such separation can be achieved via ultracentrifugation followed by extraction of the wire-containing pellet. However, if the ultracentrifugation step is too short there will be few wires present in the pellet; if it is too long then the pellet will include small proteins, expected to sediment later than the polymers, which may result in increased aggregation.

We assessed a series of centrifugation steps in which samples underwent centrifugation steps of 0, 5, 20, 60 or 1080 minutes. Additionally, the effect of sequential centrifugation was investigated by first centrifuging a sample for 240 minutes, and then centrifuging its supernatant for another 1080 minutes, and comparing its wire fraction to only a 1080 minutes step. The sequential approach resulted in a higher wire fraction. Ultimately, as can be seen in figure 3.12b a centrifugation time of only 5 minutes resulted in the overall highest wire fraction. This suggests that even short ultracentrifugation is sufficient for separating wires from small proteins or aggregates.

In summary we showed that shearing, anti-aggregation compounds, deposition time and length of (subsequent) ultracentrifugation steps affect wire fraction. Ultimately, we chose to use unsheared samples, a deposition time of 5 minutes and a ultracentrifugation time of 5 minutes. Despite its positive effect on wire fraction, β-mercaptoethanol was not employed due to its potentially negative effect on wire structure. Having optimized the protocol to improve the probability of an only-wire connection that we can measure with the probe station we will now describe the details of those measurements.

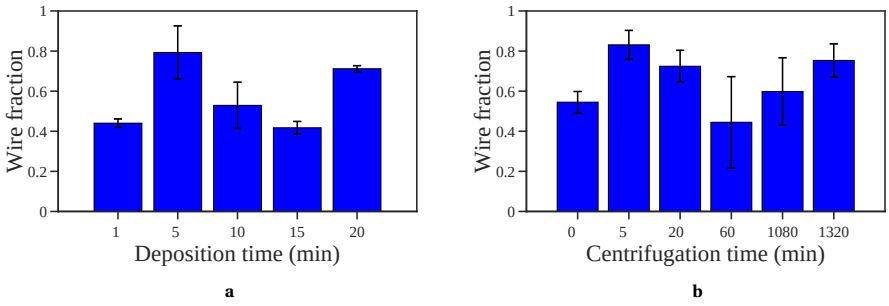

Figure 3.12: The effect of various deposition times (**a**) and of centrifugation steps (**b**) on the wire fraction (fraction of large particles present after on-chip deposition visually identified to be wires) was determined via Atomic Force Microscopy of four 10×10 µm silicon areas. **a**) Droplets were deposited on chips and left to adsorb for 1, 5, 10, 15 and 20 minutes before being blown dry. A deposition time of 5 minutes was shown to result in a similar wire fraction as 20 minutes. **b**) Samples were centrifuged for 0, 5, 20, 60, or 1080 minutes. Additionally, the effect of sequential centrifugation was investigated by first centrifuging a sample for 240 minutes, and then centrifuging its supernatant for another 1080 minutes, resulting in a total of 1320 minutes, depicted in red. A 5-minute centrifugation step was shown to result in the highest wire fraction, and the subsequent centrifugation approach also resulted in a higher wire fraction than one long centrifugation step.

MEASUREMENT SENSITIVITY

Once an only-wire connection has been made and identified there are still some practical considerations to take into account, predominately the limits of detection. Measurements consisted of a bias sweep sequence of an increase in applied bias voltage from 0 V to the target maximum bias (typically 2 V), a decrease to the negative of the target maximum bias (typically -2 V) and an increase back to 0 V (for example: $0V \rightarrow +2V \rightarrow -2V \rightarrow 0$ V). This sweep consists of a series of bias voltage steps, and at each step after a set delay (typically 100 ms) the average of 200 current measurements is determined. The maximum bias, number of measurements and delay time are set in a LabView interface connected to a Digital-to-Analog Converter (DAC) that converts the digital signal from the computer to the analog signal applied to a voltage amplification module integrated in an electronics rack custom made by Delft University of Technology. Due to the 16-bit signed integer nature of the DAC, the sweep is performed in steps of $\frac{V/V*20}{2^{16}-2}$ V, with V/V being the voltage gain set on the voltage amplification module. The electronics rack is connected to the probe station, ultimately resulting in the amplified voltage being applied to the sample.

The measured current is converted to a voltage signal through a voltage-current module integrated into the custom made electronics rack using amplifications from 10^6 to 10^9 Volt/Ampere. The resulting voltage signal is then read by the same computer interface mentioned before, this time functioning as an Analog-to-Digital Converter (ADC). Each amplification results in an upper limit of $\frac{1.25}{Amplification}$ A and a lower resolution limit of $\frac{1.25}{Amplification} * \frac{1}{2^{16}-2}$ A due to the 16-bit signed integer nature of the digital converted signal. Baseline noise in current measurements on gaps containing no bridging elements was around the resolution limit, and the current offset at 0 V was typically ten times the resolution limit. To distinguish signal from the baseline noise only values larger

than ten times the resolution limit were taken into account. The upper detection limit and the imposed lower limit of ten times the resolution limit results in an effective range of current measurements from 0.38pA to 1.25 μA.

We consider measurements up to 200 mV as 'low-bias', from 1 V as 'high-bias', and in between as 'intermediate'. For low-bias measurements to be informative the samples need to have a conductance of at least 2 pS to exceed the baseline noise at 200 mV. On the other hand, a sample with a conductance higher than 1.25 μS already reaches the maximum measurable current at 1 V, limiting information on the high-bias regime for samples with high conductance. Since the lower and upper limit of detection depend on the used amplification range it was often necessary to perform low-bias measurements with a different amplification than high-bias measurements.Taking these limitations into account, we will now discuss the processing of measured current-voltage curves.

DATA PROCESSING

The current measurement system tends to have an offset based on the electrical configuration of the setup (i.e. the amplification range set on the voltage-current gain module), resulting in a non-zero current at zero bias voltage ('current offset'). In addition, upon increasing the bias the equilibration of charge from the module to the electrode-wire contact point requires a certain amount of time dependent on resistance (R) and capacitance (C) of the system (the "RC time"). If the current is measured before equilibration, the applied bias will be overestimated or underestimated when increasing or decreasing bias respectively. This effect can largely be neglected at low sweep rates and high-bias, but it does have a significant effect on the current offset.

Therefore there are three different current offsets during one sweep: increasing from zero to maximum, decreasing from maximum to negative maximum, increasing from negative maximum to zero. In the case that multiple sweeps are performed sequentially, the last offset corresponds to the first offset of the subsequent sweep. We approximate each of these offsets by fitting a line on the region close to 0 V and taking the offset of the curve as the mean offset. We then subtract this offset from the correlated part of the sweep. In this manner all parts of the sweep align at 0 A at 0 V.

METHOD PERFORMANCE

With the optimized method, using device 3 with unsheared samples which were ultracentrifuged for 5 minutes and left to adsorb for 5 minutes, we were able to contact, localize and identify the connecting elements in 31 samples. In five cases the only bridging elements were wires while the other samples had both aggregates and wires or only aggregates. Three samples had a single wire bridging the gap, while the others had two or four wires. We can evaluate the performance of the measurement setup in the first proof-of-principle measurements of of sample C, visualized in AFM image figure 3.13 The associated single wire current-voltage (I-V) curve is depicted in figure 3.14.

Although specific features of the I-V curves will be further discussed in chapter 4, figure 3.14 already shows that we can distinguish empty gaps with currents at noise level and gaps in which current was conducted by a wire, showing that we are able to make electrical contact with single wires. Even though this wire (Sample C) had a conductance of only 4 pS, with a maximum current of 8 pA at 2 V, we can still observe features such

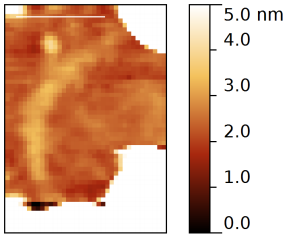

Figure 3.13: Atomic Force Microscopy image of the identified wire sample C discussed in chapter 3, Scale bar (white line) indicates 200 nm, color indicates height in a 5 nm range. Wires were deposited on chips containing gold electrodes separated by a 500 nm silicon-oxide gap. The wire is situated on a corner, thus the bottom section and top-right section are gold. Note that the image does not reflect proper relative height of gold sections, gold is 40 nm higher than silicon-oxide gap.

as a non-linear relationship between bias and current as well as symmetry in the I-V curve for negative and positive biases. As such, our method's sensitivity is sufficient for characterization of the electron transport mechanism of single wires. Characterization of non-linear relationships between bias and current requires measurements over a wide range of currents, which our setup can accommodate for.

Besides adjusting the range to improve sensitivity one can also use a low sweep rate, or a large number of steps, to provide more accurate measurements. However, a low sweep rate comes at the cost of measurement time, with any subsequent variation of measurement conditions multiplying the time required for measurements. As such, when performing accurate measurements across various conditions sample degradation on the chip may occur and impair the information gained from later measurements. We performed continually repeated overnight measurements to assess the sample's stability over time. Measurements performed a week after the sample preparation retained similar values and features to the initial measurements. In neither case the samples showed any sign of degradation over time, indicating that measurement at low sweep rates are likely unaffected by degradation as long as the measurement does not exceed 18 hours, and measurements could be repeated within a week when necessary. Besides accurate I-V curve measurements our setup allows for control of environmental conditions, which we will now discuss.

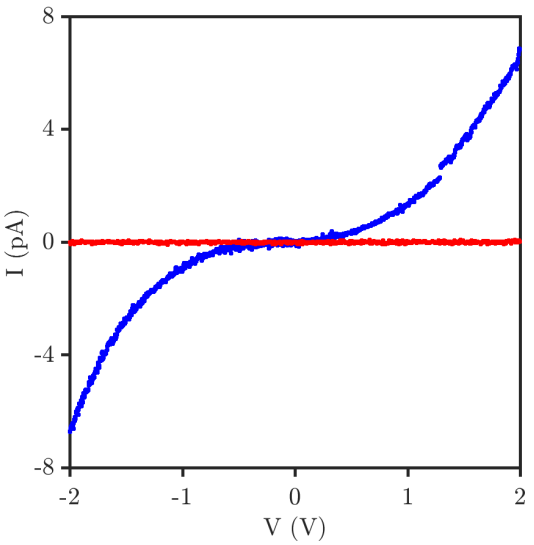

Figure 3.14: Current-voltage (I-V) characteristic of a single sweep of a single wire sample, Sample C, (depicted in blue) and an unbridged gap (depicted in red). One sweep goes from 0 V to 2 V, down to -2 V and back to 0 V. Depicted currents are the mean of current at each voltage for increasing and decreasing bias. I-V measurements were performed at room temperature in ambient conditions. Despite the low current magnitude of several pA, the current through the wire is clearly distinguishable from that of an empty gap.

ENVIRONMENTAL CONTROL

In characterizing electron transport mechanisms the temperature-dependence of conductivity is often a discriminating feature, especially when paired with bias-dependence of conductivity. In our setup the sample can be heated using a Peltier element, allowing quick characterization of temperature dependence. In a proof-of-principle measurement on an unidentified sample we performed low-bias sweeps at temperatures increasing from 308 K to 378 K in 10 K steps which can be seen in figure 3.16a, and high-bias sweeps at 308 K and 378 K depicted in figure 3.16b). An effect of temperature on current is clearly visible in figure 3.15 at low-bias as well as high-bias, proving that temperature effects on conductivity can be detected. Measurements of the effect of temperature on an identified sample are reported in chapter 4.

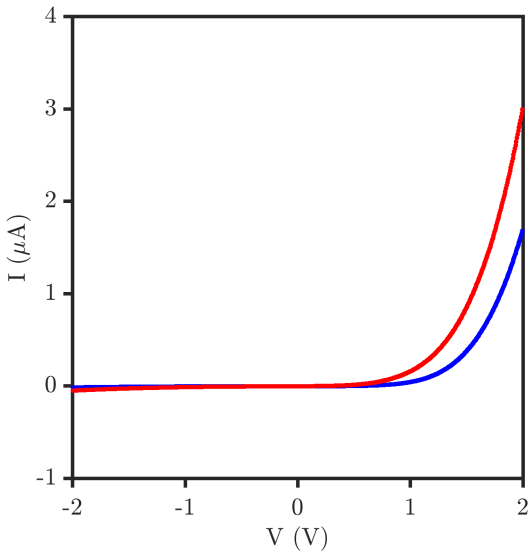

Figure 3.15: Current-voltage (I-V) characteristic of a single sweep of an unidentified sample at 378 K (depicted in red) and 308 K (depicted in blue). One sweep goes from 0 V to 2 V, down to -2 V and back to 0 V. Depicted currents are the mean of current at each voltage for increasing and decreasing bias. I-V measurements were performed in ambient conditions. An effect of temperature on current is clearly visible.

Besides variation in temperature the probe station also allows for variation in back-gate voltage. We applied a back-gate voltage by contacting the conductive non-oxidized silicon layer of the chip via a scratch through the insulating SiO_2 layer which was filled with silver paint. By contacting two such scratches with probes and measuring the current at a bias voltage of 0.01 V we confirmed the proper electrical contact with the silicon layer, visible in its high conductivity resulting in a measured current equal to the upper limit of measurement. We then applied a back-gate voltage varying from 0 to 90 V in 2 V steps. At each step we performed a bias sweep at $\pm$ 2 V, allowing investigation of the effect of a back-gate on conductivity. Again a clear effect can be observed in figure 3.17, this time varying from positive to negative depending on the particular applied back-gate.

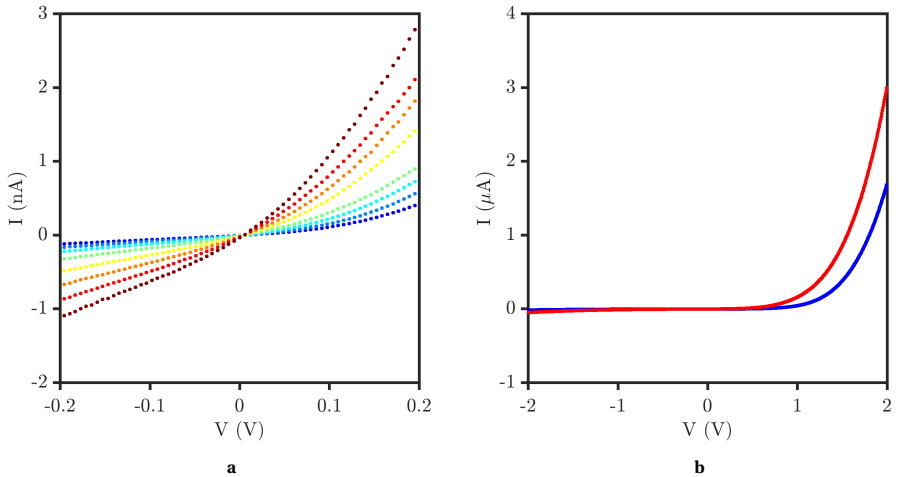

Figure 3.16: Current-voltage (I-V) characteristics of single sweep measurements of an unidentified sample at low-bias (figure 3.16a) at 308 K to 378 K in steps of 10 K (depicted in blue, dark red, and intermediate colors respectively), as well as high-bias (figure 3.16b) at 308 K and 378 K (depicted in blue and red respectively). One sweep goes from 0 V to 2 V, down to -2 V and back to 0 V. Depicted currents are the mean of current at each voltage for increasing and decreasing bias. I-V measurements were performed in ambient conditions. An effect of temperature on current is clearly visible in the form of an increase in current at higher temperatures.

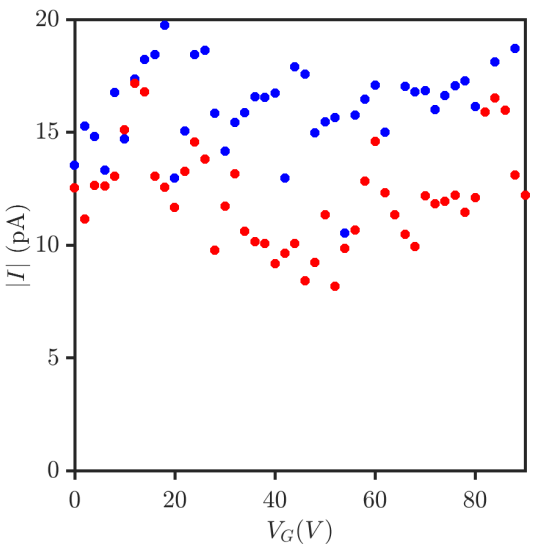

Figure 3.17: Absolute current at a bias of 2 V (depicted in blue) and -2 V (depicted in red) for an unidentified sample. Current measurements were performed at room temperature in ambient conditions. An effect of back-gate on current is visible, although there appears to be no clear relationship between back-gate voltage and current.

3.3 DISCUSSION

We have described a method for making electrical contact with single *Geobacter sulfurreducens* wires with the ability to control applied bias, temperature and back-gate bias using a stochastic approach supported by visual confirmation of the wires. The description of this method is intended to aid future investigations of the electron transport mechanism of the wires. Typical concerns in those investigations are the probability of contacting a wire, certainty of connecting element identity, and simultaneous variation of relevant parameters.

We first explored various approaches towards optimizing the probability of having an only-wire connection. The optimal chip design was found to be an interdigitated set of electrodes separated by a 500 nm gap. Combined with Passive Voltage Contrast imaging this chip design allows for rapid connection finding and identification.

The gap was crossed by wires through adsorption of wires and proteins contained in a droplet of extracellular protein extract. A complication of such a sample is the formation of aggregates, which were also shown to be conductive possibly due to high cytochrome content or containing a wire. To limit aggregate formation we investigated the effect of shearing, deposition and centrifugation time, and anti-aggregation compounds.

Shearing was shown to have a negative effect on the wire fraction of large particles, thus shearing was no longer incorporated in the standard protocol. Of a variety of anti-aggregation compounds β-mercaptoethanol was shown to be most effective in increasing wire fraction. β-mercaptoethanol was also used by Malvankar *et al.*[3] to denature cytochromes. As such, its effect on wire structure can be significant, and it depends on the research whether that effect is desired. In our case, we chose not to utilize β-mercaptoethanol in order to maintain wire structure as close to natural conditions as possible. Finally, deposition and centrifugation times of 5 minutes were both shown to result in the optimal wire fraction.

After this optimization of wire fraction, connection finding and connection identification we were able to perform the first proof-of-principle measurements. Current-voltage curves of single wires were distinguishable from empty gaps, and temperature and back-gate effects on aggregate conductivity were observed. As such, our method is able to make electrical contact with wires and characterize the dependence of conductivity on bias, temperature and back-gate. Finally, although they were not explored here, investigation of illumination effects are possible within the same setup.

Compared to previously described methods our method has the advantage of having visual confirmation of connecting element identity as well as control over a variety of environmental parameters. We used this method to characterize single wire conductivity as described in chapter 4, and to investigate conductivity of cable bacteria as described in chapter 5.

3.4 METHODS

SAMPLE PREPARATION

Geobacter sulfurreducens PCA cultures were grown statically at 25°C in 40 ml NBAFYE medium inoculated at an OD_{600} of 0.1. After 90 hours the culture was vortexed and centrifuged at 20.000×g for 20 minutes. The supernatant was removed and the cells resuspended in 40 ml ethanolamine buffer (150 mM, pH 10.5). When cells were sheared the suspension was passing through a 23G needle ten times. The cells were then vortexed for 2 minutes. In order to remove the cells the suspension was centrifuged again at 20.000×g for 20 minutes, and only the supernatant was kept. The supernatant contained the wires amongst other extracellular proteins ("wire extract"). To concentrate the wire extract it was then centrifuged at 100.000×g for 18 hours, unless mentioned otherwise, and the pellet resuspended in 1 ml ethanolamine buffer. In the optimized method the ultracentrifugation step was shortened to only 5 minutes. Aliquots of 10-50 µl were flash-frozen in liquid nitrogen and stored at -80 °C. Before deposition, aliquots were left to melt at room temperature and 1 µl of wire extract was dropped on a device on a chip (dvices are described in detail in the results section "Chip Design"). After 20 minutes the surface was washed with deionized water and blown dry using an air-gun. The chips were made using standard lithography methods on p-doped silicon wafers with a SiO_2 layer of 296 or 321 nm. Device architecture was outlined by applying and developing a resist layer. Devices were made by first sputtering an atomic layer of Al onto the chip followed by deposition of a 30 nm Au layer.

ATOMIC FORCE MICROSCOPY IMAGING

For imaging the silicon for determination of wire fraction and the gaps for identification of connecting elements we used the NanoScope V Atomic Force Microscope of Bruker. The type of cantilever used was "Cantilever B" from the "All-In-One-Al" probe made by BudgetSensors with a force constant of 2.7 N/m and resonance frequency of 80 kHz. The AFM was used in tapping mode starting with a drive amplitude typically in the range of 500 mV and amplitude set-point typically in the range of 300 mV. Subsequently, the amplitude set-point was increased up to the point where signal was lost, to be lowered again until proper tracing occurred. When image quality was poor different combinations of amplitude and set-point were used, each time setting the set-point close to where the signal was lost. This was done to minimize the force exerted on the wire while still providing a clear image.

DUAL-BEAM OPERATION

The electron beam was operated at 30 kV with a current of 43 pA and an aperture of 45 µm, while the ion beam was operated at a current of 10 pA. Due to the destructive nature of electron and ion beam imaging special care was taken to avoid imaging areas possibly containing bridging elements (i.e. gaps). Main electrodes were grounded by applying carbon paint from the main pad to the back of the chip. The back of the chip is then in electrical contact with the steel Dual-Beam chamber, effectively grounding the main.

I-V MEASUREMENTS

All I-V measurements were performed using a TTP4 Desert (LakeShore) Cryogenics probe station with mounted probes from Lakeshore ZN50R-CVT-25-BECU and ZN50R-25-BECU for varying or constant temperature measurements respectively. These probes were connected to a TU Delft IVVI rack containing custom electronics modules. Applied and measured voltages were set and read via a LabView interface controlling an Adwin II Gold Digital-Analog Converter. Before measuring across pads, a check for a proper connecting main electrode was performed by measuring the conductivity between two distant points along the lead (i.e. confirming a short circuit). Typical sweeps were performed up to ±2.0 V or ±4.0 V divided over $2^{16-1}/10$ points, at each point the current was determined as an average of 200 measurements taken within 5 ms. A delay of 400, 100 or 10 ms was used at each point before measuring for constant temperature, varying temperature and back-gate measurements respectively. In case clipping occurred, the gain was adjusted appropriately. The measured currents at 0 V were non-zero, with the magnitude of the current depending on the configuration of the setup, predominantly the range set on the voltage-current amplifier module. Data was corrected for this by fitting a linear curve through the 20 points surrounding 0 V, and then substracting the value of the fit at 0 V from all points.

BACK-GATE AND TEMPERATURE MEASUREMENTS

A back-gate was constructed by scratching the surface of the SiO_2, exposing the conductive silicon layer underneath. The scratch was then quickly covered by silver paint. This was done in two spots of a chip, and the proper electrical contact was checked by measuring the conductivity from one spot to another. The sample was heated by a Peltier element controlled by a LakeShore 331 Temperature Controller connected to a local silicon-diode temperature sensor. The sample stage and probe chamber were cooled by connecting the exhaust of a tank containing liquid nitrogen or helium to a chamber underneath the probe chamber. The gas content of the probe chamber could be controlled by flushing with nitrogen and the chamber can be put under vacuum through an exhaust connected to a vacuum pump.

REFERENCES

[1] Z. M. Summers, H. E. Fogarty, C. Leang, A. E. Franks, N. S. Malvankar, and D. R. Lovley, *Direct exchange of electrons within aggregates of an evolved syntrophic coculture of anaerobic bacteria.* Science (New York, N.Y.) **330**, 1413 (2010).

[2] D. R. Lovley, *Powering microbes with electricity: direct electron transfer from electrodes to microbes.* Environmental microbiology reports **3**, 27 (2011).

[3] N. S. Malvankar, M. Vargas, K. P. Nevin, A. E. Franks, C. Leang, B.-C. Kim, K. Inoue, T. Mester, S. F. Covalla, J. P. Johnson, V. M. Rotello, M. T. Tuominen, and D. R. Lovley, *Tunable metallic-like conductivity in microbial nanowire networks.* Nature nanotechnology **6**, 573 (2011).

[4] R. Y. Adhikari, N. S. Malvankar, M. T. Tuominen, and D. R. Lovley, *Conductivity of Individual Geobacter Pili,* Submitted **6**, 8354 (2015).

[5] S. Lampa-pastirk, J. P. Veazey, K. A. Walsh, G. T. Feliciano, R. J. Steidl, S. H. Tessmer, and G. Reguera, *Thermally activated charge transport in microbial protein nanowires,* Nature Publishing Group , 1 (2016).

[6] N. S. Malvankar, S. E. Yalcin, M. T. Tuominen, and D. R. Lovley, *Visualization of charge propagation along individual pili proteins using ambient electrostatic force microscopy,* Nature Nanotechnology **9**, 1012 (2014).

[7] T. Zoungrana, G. Findenegg, and W. Norde, *Structure, Stability, and Activity of Adsorbed Enzymes,* Journal of colloid and interface science **190**, 437 (1997).

[8] S. Hélaine, E. Carbonnelle, L. Prouvensier, J.-L. Beretti, X. Nassif, and V. Pelicic, *PilX, a pilus-associated protein essential for bacterial aggregation, is a key to pilus-facilitated attachment of Neisseria meningitidis to human cells.* Molecular microbiology **55**, 65 (2005).

[9] E. Roine, W. Wei, J. Yuan, E. L. Nurmiaho-Lassila, N. Kalkkinen, M. Romantschuk, and S. Y. He, *Hrp pilus: an hrp-dependent bacterial surface appendage produced by Pseudomonas syringae pv. tomato DC3000.* Proceedings of the National Academy of Sciences of the United States of America **94**, 3459 (1997).

[10] K. Xiao, N. S. Malvankar, C. Shu, E. Martz, D. R. Lovley, and X. Sun, *Low Energy Atomic Models Suggesting a Pilus Structure that could Account for Electrical Conductivity of Geobacter sulfurreducens Pili,* Nature Publishing Group , 1 (2016).

[11] R. Rosenkranz, *Failure localization with active and passive voltage contrast in FIB and SEM,* Journal of Materials Science: Materials in Electronics **22**, 1523 (2011).

[12] B. M. Baynes, D. I. C. Wang, and B. L. Trout, *Role of arginine in the stabilization of proteins against aggregation,* Biochemistry **44**, 4919 (2005).

[13] F. Wang, Y. Gu, J. P. O'Brien, S. M. Yi, S. E. Yalcin, V. Srikanth, C. Shen, D. Vu, N. L. Ing, A. I. Hochbaum, E. H. Egelman, and N. S. Malvankar, *Structure of Microbial*

Nanowires Reveals Stacked Hemes that Transport Electrons over Micrometers, Cell **177**, 361 (2019).

[14] W. Wang, *Protein aggregation and its inhibition in biopharmaceutics,* International Journal of Pharmaceutics **289**, 1 (2005).

[15] T. Li, J. Hu, R. Tian, K. Wang, J. Li, A. Qayum, A. Bilawal, M. A. Gantumur, Z. Jiang, and J. Hou, *Citric acid promotes disulfide bond formation of whey protein isolate in non-acidic aqueous system,* Food Chemistry **338**, 127819 (2021).

[16] P. Xavier and N. Galamba, *Effect of urea on the hydration and aggregation of hydrophobic and amphiphilic solute models: Implications to protein aggregation,* Journal of Chemical Physics **155** (2021), 10.1063/5.0064707.

[17] A. M. Kroetsch, E. Sahin, H. Y. Wang, S. Krizman, and C. J. Roberts, *Relating particle formation to salt- and pH-dependent phase separation of non-native aggregates of alpha-chymotrypsinogen A,* Journal of Pharmaceutical Sciences **101**, 3651 (2012).

[18] V. Vagenende, M. G. Yap, and B. L. Trout, *Mechanisms of protein stabilization and prevention of protein aggregation by glycerol,* Biochemistry **48**, 11084 (2009).

[19] B. A. Kerwin, *Polysorbates 20 and 80 used in the formulation of protein biotherapeutics: Structure and degradation pathways,* Journal of Pharmaceutical Sciences **97**, 2924 (2008).

4

BIONANOWIRE CONDUCTIVITY DEPENDENCE ON BIAS, TEMPERATURE, AND BACK-GATE VOLTAGE

We apply the method described in chapter 3 to characterize the conductive properties of single G. sulfurreducens*bionanowires. Current-voltage curves showed conductances in orders of magnitudes from* 10^{-13} *S up to* $10^{-}6$ *S. Measurements at varying temperatures identified activation energies from 0.36 eV to 0.41 eV. Arrhenius plots displayed features of both a simple model where electron transport rate was limited by injection barriers and a model where electron transport rate is limited by intramolecular hopping. Future modeling is required to fully describe the electron transport*

Chips manufactured by Nandini Muthusubramian and Jacqueline A. Labra Muñoz. Methods are reproduced from chapter 3.

4.1 INTRODUCTION

The first I-V curves measured along *G. sulfurreducens* wires were reported [1] to have a linear relationship between current and bias up to 0.5 V. In subsequent studies with Conductive Probe Atomic Force Microscopy (CP-AFM) the applied bias range was expanded up to 1 V, where a deviation from linearity at voltages larger than 0.5 V became apparent [2]. As such, conductivity appears to be constant at biases below 0.5 V but is positively correlated to bias above that threshold.

Besides an effect of bias on conductivity an effect of temperature was identified by Malvankar *et al.* [3]. They performed the early investigations into temperature dependence using biofilm mats and wire networks. Temperature was shown to have a positive effect from 200 K to 265 K, a negative effect above 270 K, and for wire networks again a slight positive effect above 290 K. The first inspection of the effect of temperature on single wire conductivity was performed by Lampa-pastirk *et al.* [2] who used Scanning Tunneling Microscopy to measure the differential conductance across the height of a pilum [2]. At a temperature of 77 K the differential conductance remained zero up to 0.1 or 0.2 V, while at room temperature the differential conductance was larger than zero at zero bias. This effect was stronger in some regions of the wires than others, with a periodic pattern of increased effect every 3 to 4 nm. This means that with increasing temperature the density of states at particular parts of the pilum is increased. The temperature investigations are limited, and to our knowledge no measurements of temperature dependence of conductivity along the length of single wires have been reported, while those are crucial to identifying distinctive features of electron transport.

Similarly, reports of back-gate measurements are scarce. Such measurements were, to the best of our knowledge, only performed via electrolytic gating of a live biofilm and wire networks by Ing *et al.* [4] and Snider [5]. In those studies the potential of source and drain electrode had a fixed offset while the source potential was then varied with respect to the reference electrode, creating an effective sweep in gate potential. The gate sweep measurements on biofilms showed a redox peak centered around -0.3 V with respect to a Ag/AGCl reference electrode. In contrast, the same measurements performed on wire networks did not have such a redox peak. This seems to indicate a role of redox sites in conductivity of biofilms, but not in wire networks. Still, thorough investigation of the main features of conductivity dependence on bias, temperature and back-gate is lacking. Such measurements, especially along the length of a single wire, are required for characterization of wire conductivity in order to describe a useful model for electron transport.

Temperature dependent conductivity measurements on a single wire in a large temperature range can provide a more complete picture of the charge transport properties of the wires. A larger temperature range can for example allow one to investigate the dependence of conductivity on the natural logarithm of temperature. If this dependence is linear, a fit can determine the activation energy associated with the charge transport mechanism. In chapter 3 we have described a method capable of measuring temperature dependence of conductivity. Additionally, our method allows for the application of a back-gate voltage. We report here the current-voltage curves determined at various biases, temperatures and back-gate voltages, informing on the linearity of conductivity, its associated activation energies and field effects on single wire conductivity.

4.2 METHODS

The methods used are identical to those described in chapter 3, except for the shearing step in sample preparation. After the optimization described in chapter 3 wire extracts were no longer sheared and ultracentrifugation time was reduced to 5 minutes, unless otherwise specified. Below the method section of chapter 3 is reproduced for ease of reading, Atomic Force Microscopy (AFM) images of the samples discussed in this chapter are included.

SAMPLE PREPARATION

Geobacter sulfurreducens PCA cultures were grown statically at 25°C in 40 ml NBAFYE medium inoculated at an OD_{600} of 0.1. After 90 hours the culture was vortexed and centrifuged at 20.000×g for 20 minutes. The supernatant was removed and the cells resuspended in 40 ml ethanolamine buffer (150 mM, pH 10.5). When cells were sheared the suspension was passing through a 23G needle ten times. The cells were then vortexed for 2 minutes. In order to remove the cells the suspension was centrifuged again at 20.000×g for 20 minutes, and only the supernatant was kept. The supernatant contained the wires amongst other extracellular proteins ("wire extract"). To concentrate the wire extract it was then centrifuged at 100.000×g for 18 hours, unless mentioned otherwise, and the pellet resuspended in 1 ml ethanolamine buffer. In the optimized method the ultracentrifugation step was shortened to only 5 minutes. Aliquots of 10-50 µl were flash-frozen in liquid nitrogen and stored at -80 °C. Before deposition, aliquots were left to melt at room temperature and 1 µl of wire extract was dropped on a device on a chip (dvices are described in detail in the results section "Chip Design"). After 20 minutes the surface was washed with deionized water and blown dry using an air-gun. The chips were made using standard lithography methods on p-doped silicon wafers with a SiO_2 layer of 296 or 321 nm. Device architecture was outlined by applying and developing a resist layer. Devices were made by first sputtering an atomic layer of Al onto the chip followed by deposition of a 30 nm Au layer.

ATOMIC FORCE MICROSCOPY IMAGING

For imaging the silicon for determination of wire fraction and the gaps for identification of connecting elements we used the NanoScope V Atomic Force Microscope of Bruker. The type of cantilever used was "Cantilever B" from the "All-In-One-Al" probe made by BudgetSensors with a force constant of 2.7 N/m and resonance frequency of 80 kHz. The AFM was used in tapping mode starting with a drive amplitude typically in the range of 500 mV and amplitude set-point typically in the range of 300 mV. Subsequently, the amplitude set-point was increased up to the point where signal was lost, to be lowered again until proper tracing occurred. When image quality was poor different combinations of amplitude and set-point were used, each time setting the set-point close to where the signal was lost. This was done to minimize the force exerted on the wire while still providing a clear image. AFM images of sample A to D are given in figure 4.1.

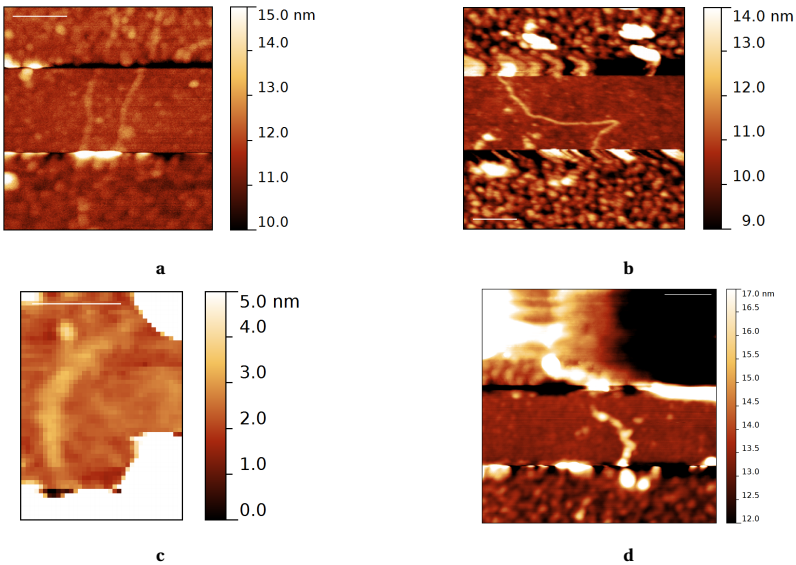

Figure 4.1: AFM images of the identified wire samples discussed in chapter 4, figure panels a to d correspond to samples A to D. Depicted samples are samples in which the only identified connecting elements were the wires shown in the image. Sample C was presented in chapter 3 but is reproduced here for overview. In **c** the wire is situated on a corner, thus the bottom section and top-right section are gold. Wires were deposited on chips containing gold electrodes separated by a 500 nm silicon-oxide gap. In **d** the apparent gap in the wire near the top gold is due to an AFM artifact near the gold walls. Scale bar (white line) indicates 200 nm, color indicates height, in a 5 nm range. Top and bottom sections are gold, middle section is a 500 nm silicon-oxide gap. Note that images do not reflect proper relative height of gold sections, gold is 40 nm higher than silicon-oxide gap.

DUAL-BEAM OPERATION

The electron beam was operated at 30 kV with a current of 43 pA and an aperture of 45 μm, while the ion beam was operated at a current of 10 pA. Due to the destructive nature of electron and ion beam imaging special care was taken to avoid imaging areas possibly containing bridging elements (i.e. gaps). Main electrodes were grounded by applying carbon paint from the main pad to the back of the chip. The back of the chip is then in electrical contact with the steel Dual-Beam chamber, effectively grounding the main.

I-V MEASUREMENTS

All I-V measurements were performed using a TTP4 Desert (LakeShore) Cryogenics probe station with mounted probes from Lakeshore ZN50R-CVT-25-BECU and ZN50R-25-BECU for varying or constant temperature measurements respectively. These probes were connected to a TU Delft IVVI rack containing custom electronics modules. Applied and measured voltages were set and read via a LabView interface controlling an Adwin II Gold Digital-Analog Converter. Before measuring across pads, a check for a proper connecting main electrode was performed by measuring the conductivity between two distant points along the lead (i.e. confirming a short circuit). Typical sweeps were performed up to ±2.0 V or ±4.0 V divided over $2^{16-1}/10$ points, at each point the current was determined as an average of 200 measurements taken within 5 ms. A delay of 400, 100 or 10 ms was used at each point before measuring for constant temperature, varying temperature and back-gate measurements respectively. In case clipping occurred, the gain was adjusted appropriately. The measured currents at 0 V were non-zero, with the magnitude of the current depending on the configuration of the setup, predominantly the range set on the voltage-current amplifier module. Data was corrected for this by fitting a linear curve through the 20 points surrounding 0 V, and then substracting the value of the fit at 0 V from all points.

BACK-GATE AND TEMPERATURE MEASUREMENTS

A back-gate was constructed by scratching the surface of the SiO_2, exposing the conductive silicon layer underneath. The scratch was then quickly covered by silver paint. This was done in two spots of a chip, and the proper electrical contact was checked by measuring the conductivity from one spot to another. The sample was heated by a Peltier element controlled by a LakeShore 331 Temperature Controller connected to a local silicon-diode temperature sensor. The sample stage and probe chamber were cooled by connecting the exhaust of a tank containing liquid nitrogen or helium to a chamber underneath the probe chamber. The gas content of the probe chamber could be controlled by flushing with nitrogen and the chamber can be put under vacuum through an exhaust connected to a vacuum pump.

4.3 RESULTS

In order to perform conductivity measurements the wires need to be electrically contacted. The method used to achieve this is outlined in detail in chapter 3. In summary, droplets of extracellular protein solutions containing the wires of *Geobacter sulfurreducens* were deposited onto microchips shown in figure 4.2 containing pre-patterned

gold electrodes separated by a 500 nm gap. Subsequently, electrically bridged gaps were

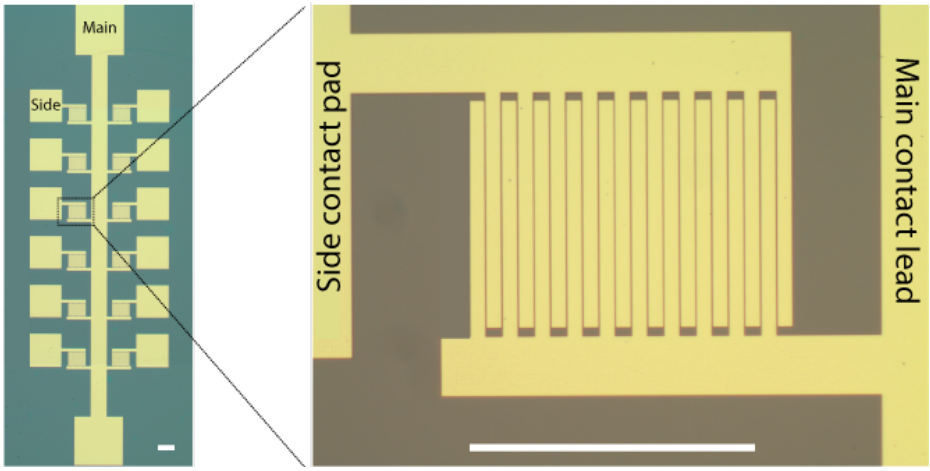

Figure 4.2: Device (left) used for wires deposition, and zoom-in (right) on a potential contact area, indicated by dashed lines. The potential contact area consisted of an interdigitated array of gold electrodes separated by a 500 nm gap. One half of the array was connected to the main contact pad (top and bottom squares, one of which is labelled "Main") via the main lead (vertical connection) while the other half was connected to a side contact pad (left and right squares, one of which is labelled "Side"). A droplet containing wires was deposited across the whole device, left to adsorb for 20 minutes and then washed and blown dry. Conductive wires that adsorbed in a potential contact area could create an electrical connection between the main pads and the side pads if they adsorbed across one of the 500 nm gaps.

located and the connecting element was visually identified via AFM. The connecting elements consisted either of aggregates (possibly containing wires) or wires. Current-voltage (I-V) curves were measured in 31 samples. In 5 samples wires were identified as the only component bridging the gap between electrodes (here referred to as 'identified samples'). In the 26 other cases there were wires as well as aggregates connecting the electrodes, or only aggregates (here referred to as 'unidentified samples'). Of the identified samples, some contained a single wire (sample B, C and D), while others had multiple wires (sample A had 2, sample E had 4). Note that it is unlikely that multiple wires are making electrical contact and as such the samples containing multiple wires are likely to still have only one conducting wire. We will comment on the distribution in behavior of all samples while highlighting some features in I-V curves of identified wire samples A, B and D.

I-V curves were measured in "sweeps", with each sweep starting with an increase in bias from 0 V up to a maximum bias (typically 2 or 4 V) in steps of 1 or 10 mV with 100 ms delay between each step, then decreasing the bias down to the negative maximum bias (typically -2 or -4 V) and finally increasing the bias back to 0 V. At each voltage the current was determined as the average of 200 repeated measurements. When depicting I-V curves consisting of multiple sweeps we instead depict the "mean I-V curve" where for each voltage we determine the mean of all measured currents at that voltage of all sweeps. A typical example of an I-V curve can be seen in figure 4.6, which will be discussed in more detail below. First we will discuss conductance at a biologically relevant

potential difference.

LOW-BIAS CONDUCTANCE

In the natural environment of *G. sulfurreducens* the redox potential difference between electron donor and acceptor does not exceed 1 V, and a typical[6] value is around 0.5 V. This difference is set along a length of a single wire up to a few micrometers, or a network of connected wires of tens of micrometers[3]. When considering a simple linear distance dependence of resistance, the maximum voltage drop of 1 V over a distance of 2 µm corresponds to a voltage drop of 0.25 V over the 0.5 µm gap used in this study. We therefore defined the range up to 0.2 V here as the "low-bias" range. Current-voltage curves in this range show a wide range in conductance. The distribution of conductances depicted in figure 4.3a for all samples (both identified an unidentified) shows that the conductance at 0.2 V ranges from pS up to µS, with most between 10 to 100 pS. At 0.2 V it was not possible to discriminate signal from noise when conductance was below 1 pS.

In previous work the low-bias I-V curves were shown to be linear. To determine whether our low-bias I-V curves were linear or non-linear a fit was performed to the data in the -0.2 V to 0.2 V range with $I \propto V^{\alpha}$ (a "power-law fit") . In such a power-law fit, an alpha of one indicates a linear relationship, two indicates quadratic, three cubic, and so on. The distribution of α found for samples with a significant fit in the low-bias range is shown in figure 4.3b, where it can be seen that it was close to one for every sample, confirming linearity at low bias. Having identified overall trends in identified and unidentified samples we will now discuss the features of an identified wire sample.

First we will discuss sample A, the sample with the highest measured currents, due to its excellent signal-to-noise ratio. In Sample A the only connecting elements across the gap were 2 wires. The I-V curve for low bias depicted in figure 4.6a shows that the current depends linearly on applied voltage bias, although it begins to deviate from linearity around 0.2 V . The current at 0.2 V equals 4.75 nA, corresponding to a conductance of 23,8 nS. If we use a simple model for conductivity and consider both wires to be in electrical contact, and each wire has a cylindrical shape with a diameter of 3 nm and length of 500 nm then these values correspond to a conductivity of 85 mS cm, similar to previously found values[1] and on-par with synthetic organic semi-conductors[7]. Through a significant power-law fit Sample A was determined to have an α exponent of 1.06, confirming that the behavior is close to linear. As such, this identified single-wire sample showed similar behavior as those identified in the overall analysis of both identified an unidentified samples. In summary, conductance varied from pS to µS, which for a single wire using a simple model would correspond to conductivities between 10 µS/cm to 10 S/cm, and at low-bias current and voltage have a linear relationship. In addition our setup allows investigation of high bias conductivity as well, which we will discuss next.

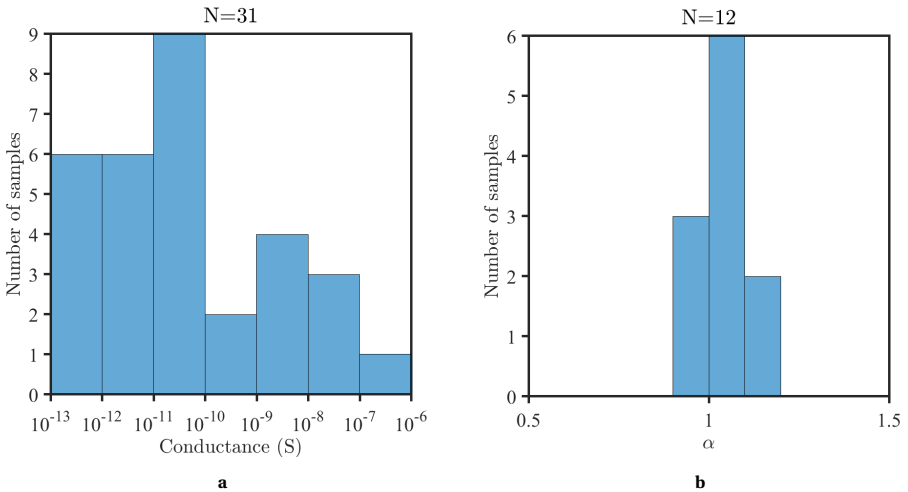

Figure 4.3: Distribution of conductance (**a**) at 0.2 V as measured for 31 samples of wildtype *G. sulfurreducens* wires deposited across a 500 nm gap between gold electrodes. In 7 samples wires were the only connecting element between the gold electrodes. In 24 samples the connecting element was either a combination of wires and aggregates, or only aggregates. The conductance varies from the lower detection limit of 0.38 pA up to 1.25 μA. For 12 samples the exponential coefficient of a significant power-law fit ($I \propto V^{\alpha}$) could be determined based on the current-voltage (I-V) measurements from -0.2 up to +0.2 V. The distribution of those exponential coefficients (**b**) shows that the exponent is close to 1 in each of those samples, corresponding to linear I-V characteristics.

HIGH-BIAS CONDUCTANCE

The use of electrodes for measurements allows investigation of high-bias conductivity. Although this bears little resemblance to typical biological environmental conditions, it can help to identify the underlying charge transport mechanism. Just as with low-bias a wide range of conductance is observed at high bias. A spread of conductances from pS up to µS is visible in figure 4.4a. At 2 V we can not identify a conductance higher than 1 µS due to the upper limit of the current detection. The numbers are comparable to the conductance at low bias but this should not be interpreted as a sign of linearity, when measuring beyond 0.2 V up to 2 V the deviation from linearity can increase.

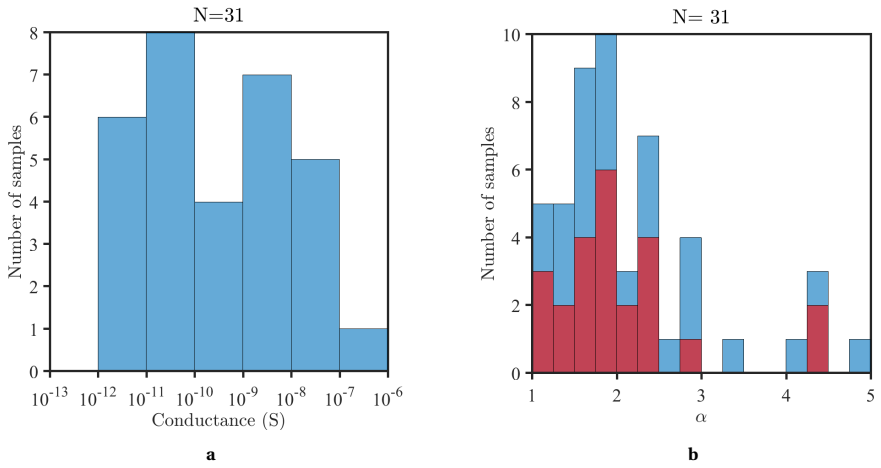

Figure 4.4: a) Distribution of conductance (I/V) at 2 V as measured for the same 31 samples of wildtype *G. sulfurreducens* wires as shown in figure 4.3a. The conductance varies from the lower current detection limit at 2 V of 0.38 pA up to the upper current detection limit at 2 V of 1.25 μA. **b)** For each sample the exponential coefficient α ($I \propto V^{\alpha}$) has been determined based on the current-voltage (I-V) measurements from 0.5 up to 2 V and/or from -0.5 down to -2 V. The combined distribution of both negative and positive bias coefficients are shown. The fraction of positive or negative bias coefficients is indicated in blue or red respectively. It is clear that the exponential coefficient is larger than 1 for each of those samples, indicating non-linear I-V characteristics. Although most coefficients fall between 1 and 2, the distribution does not appear to be centered around a particular value. Note that one sample can have different coefficients for positive and negative bias, reflecting asymmetry in the I-V curves.

We first note that some of the I-V characteristics at high-bias become highly asymmetric, to determine the α thus requires separate fits on I-V curves at positive or negative bias. From the distribution of the determined α depicted in figure 4.4 we found that at high bias the α varies from 1.08 to 4.62, with most below 2.5. It appears that from 0.2 V to 1 V there is a regime transition, with linear I-V dependence below 0.2 V, increasingly non-linear I-V dependence between 0.2 and 1 V, and finally constant non-linear I-V dependence above 1 V.

In samples where fits on low bias and high bias were both significant (with a coefficient of determination $R^2 > 0.95$) we can determine the voltage at which the high-bias non-linear fit more closely describes the I-V curve than the low-bias linear fit, here defined as the "cross-over voltage". We can calculate this voltage as the intersect of the

low-bias fit with the high-bias fit. As can be seen in its distribution in section 4.3 most cross-over voltages fall between 0.4 and 0.5 V, similar to the cross-over voltage of 0.5 reported by Lampa-pastirk *et al.*[2].

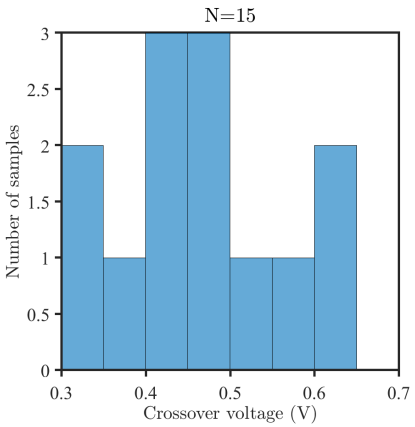

Figure 4.5: Distribution of crossover voltages for samples in which a significant power-law fit could be made on both low bias (from 0 to ±0.2 V) and high bias (from ± 1 to ± 2 V) voltages. The crossover voltage was calculated as the voltage at which the low bias fit and high bias fit intersect. For most samples the crossover voltage is between 0.4 and 0.5 V.

Just like at low bias the trends identified in all samples are reflected in the identified wire samples, of which we will again discuss sample A. As evident in figure 4.6a the sample displayed a current of 50 nA at 1 V resulting in a conductivity of 0.17 S/cm. However, at twice the voltage (2 V) it displayed a current nearly four times higher (192 nA), with a conductivity of 0.33 S/cm. It is clear that at least from 1 to 2 V, there is a non-linear dependence of current on the applied bias voltage. Plotting the curve on a log-log scale makes this behavior more apparent, as can be seen in figure 4.6b. A power-law fit on the high bias regions results in an α exponent of 1.83, close to a quadratic relationship. For sample A the crossover voltage is at 0.45 V, similar to the values for all samples.

The asymmetry at high bias observed in two unidentified samples also occurred in identified single wire sample B. In the I-V curve in section 4.3 the current for sample B at 2 V was 181 times larger than that at -2 V bias. It was not possible to determine the asymmetry at low bias since the currents did not exceed the noise level. However, a power-law fit was possible on high-bias data where the positive high-bias α was 4.13, while at negative high bias it was 1.80, as shown in figure 4.6b.

In summary, the identified wire samples share both low- and high-bias features seen in the overall analysis. I-V curves are linear at low bias and non-linear at high bias, with a crossover voltage around 0.45 V and occasional asymmetry at least at high-bias. The conductivity varies between wires over several orders of magnitude and the non-linearity at high-bias varies from linear to quintic, with most samples having an exponent between 1.5 and 2. Having identified the predominant features of bias dependence, we will now discuss temperature dependence of an identified single wire sample.

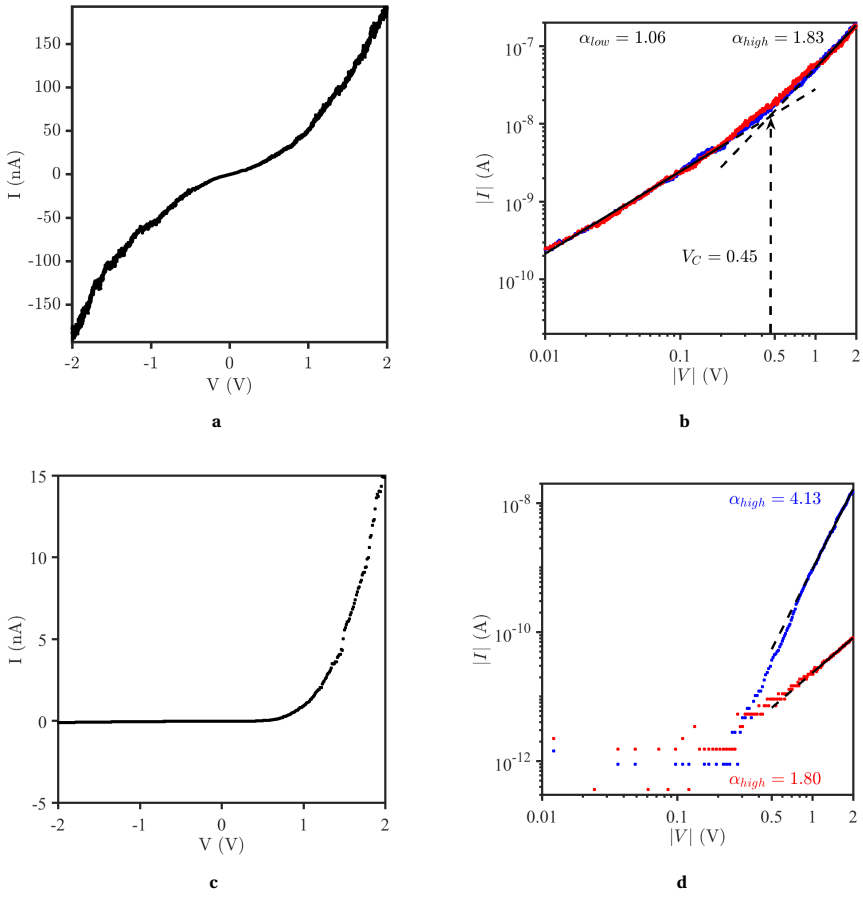

Figure 4.6: Mean current-voltage (I-V) curve of 3 subsequent sweeps of sample A plotted on a linear (**a**) and log-log (**b**) scale, and 1 sweep of sample B plotted on a linear (**c**) and log-log (**d**) scale. **a)** The conductivity at 1 V is 0.35 S/cm, while at 2 V the conductivity is 0.67 S/cm, showing that the I-V curve is non-linear at high bias. **b)** The exponential coefficient α of a power-law fit for low bias ($|V| < 0.2V$) is 1.06, showing that the I-V curve is close to linear ($\alpha = 1$) at low bias. In contrast, the same fit at high bias ($|V| > 1V$) results in an α of 1.83 confirming that the I-V curve is non-linear at high bias. The cross-over voltage is defined as the voltage from which the high bias fit more closely resembles the measurements than the low bias fit is defined as . This is indicated with the dashed arrow pointing to where the two fits intersect. The close overlap in blue and red curves implies no clear asymmetry in the I-V curve. **c)** The conductivity at -2 V is 0.28 mS/cm while the current at +2 V is 0.051 S/cm, showing strong asymmetry since the conductivity at positive bias is 181 times larger than the maximum current at negative bias. **d)** For low bias ($|V| < 0.2V$) no significant power-law fit could be obtained. For high bias ($> 1|V|$) the exponential coefficient α of a power-law fit for positive bias is 4.13, while the α for negative bias is 1.80. This more than two-fold difference in exponent readily results in a large absolute difference in current. The connecting elements in Sample A consisted of 2 wires, and B consisted only of 1 wire. One sweep goes from 0 V to 2 V, down to -2 V and back to 0 V. I-V measurements were performed at room temperature in ambient conditions. In **b** and **d** the blue curve is the mean of currents measured in all sweeps at each positive voltage only, and the red curve is same but for each absolute negative bias only. The solid black lines in **b** and **d** indicate the fit found on the low (0 to 0.2 V) and high (1 to 2V) bias range, while the dashed lines represent the prediction of each in between those ranges.

TEMPERATURE DEPENDENCE

Of sample D we measured the temperature dependence of conductivity. The connecting elements in sample D consisted of 1 wire. To measure at temperatures higher than room temperature a heating element was used to heat up to 340 K. Then we let the sample cool in increments of 10 K while continuously performing I-V sweeps. To cool below room temperature down to 220 K we used liquid helium in the cooling chamber of the probe station while continuously measuring I-V curves with sweeps from -2 to 2 V. Then we let the sample heat towards to room temperature in increments of 10 K while continuously performing I-V sweeps. We first performed these measurements in a vacuum to minimize water condensation, but later repeated them in ambient conditions which will be discussed after the vacuum measurements. We consider first the starting measurement at room temperature, and then the effect of temperature on the low bias conductivity, followed by high bias conductivity.

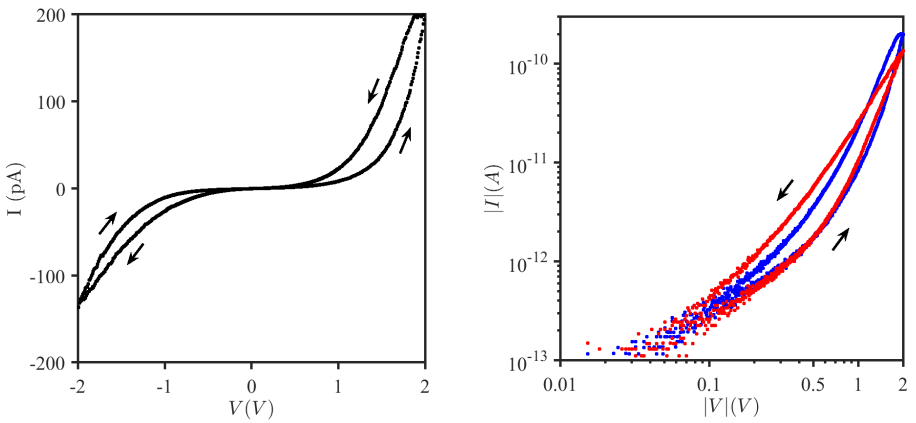

Figure 4.7: Mean current-voltage (I-V) curve of 1 sweep of sample D plotted on a linear (**a**) and log-log (**b**) scale. At the same voltage the measured absolute current is higher at decreasing bias than at increasing bias, an effect called hysteresis. Arrows indicate direction of curve, i.e. increasing or decreasing bias. In **b** blue and red indicate positive and negative bias respectively. The connecting elements in Sample D consisted of 2 wires. One sweep goes from 0 V to 2 V, down to -2 V and back to 0 V. I-V measurements were performed at room temperature in vacuum. Measurements were performed at steps of 1 mV, with 100 ms between each step.

At room temperature and low bias sample D exhibits currents close to the noise level, while at high bias the current goes up to 200 pA at 2 V (see figure 4.7 at a voltage below 0.2 V and at 2 V). There is slight asymmetry, with the maximum absolute current at -2 V being 135 pA, the absolute current at 2 V is 1.48 times higher than at -2 V. In addition, at the same voltage the measured absolute current is higher when decreasing bias than when increasing bias, an effect called hysteresis. To simplify further discussion of currents in this section the mean is taken of the currents measured for increasing and decreasing bias for each voltage, thus averaging out the hysteresis effect, unless otherwise specified. As with previous samples, the I-V curve in figure 4.7 is close to linear at low bias and

non-linear at high bias.

With the starting I-V curve identified, we can consider the effects of temperature on this curve, starting with effects on low-bias conductivity. As figure 4.8a shows, when increasing temperature the conductivity also increases while I-V curves remain linear up to ±0.2 V. Below 260K the conductivity is too low to distinguish measured currents from noise (see green to blue curves in figure 4.8a).

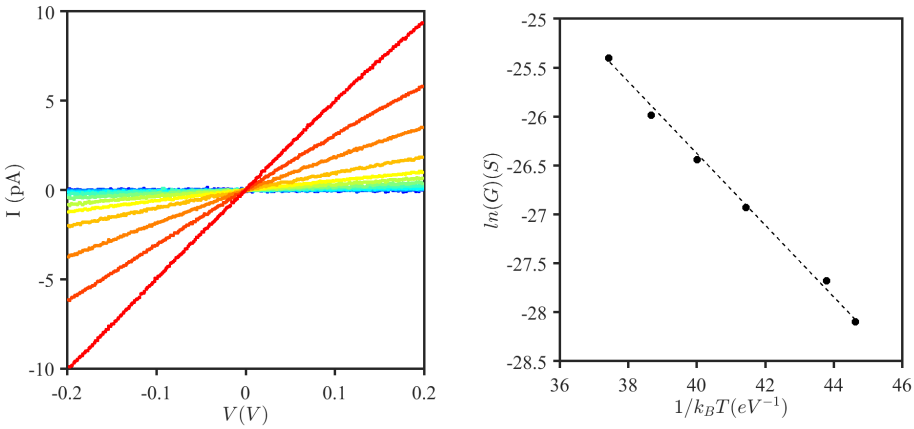

Figure 4.8: a) Mean current-voltage (I-V) curves in the low bias regime ($|V| < 0.2V$) of one sweep for sample D at various temperatures. Conductivity increases with temperature and I-V curves remain linear independent of temperature. **b)** Arrhenius plot of conductance measured in ambient conditions at 0.2 V for temperatures from 260 K up to 340 K. In an Arrhenius plot the slope of a linear fit on the measurements corresponds to the activation energy. The activation energy was determined to be 0.37 eV by a fit (dashed line) with a $R^2 > 0.99$. I-V curves were measured in vacuum with constant temperature per sweep. One sweep goes from 0 V to 2 V, down to -2 V and back to 0 V. The connecting elements in sample D consisted of 2 wires. From blue to red temperature goes from 220 K to 340 K in steps of 10 K (blue representing cold, red representing hot).

When plotting the natural log of conductance versus $1/k_BT$ in the Arrhenius plot in figure 4.8b a significant linear fit can be obtained. This means that temperature has an exponential effect on conductivity, and we can consider an activation energy of some underlying process. We can quantify the effect of temperature by determining the activation energy associated with the conductivity as described by $I \propto e^{\frac{-E_a}{k_BT}}$, where k_B is the Boltzmann constant, T is the temperature and E_a is the activation energy. It follows that $\ln(I) \propto -E_a \frac{1}{k_BT}$, so we can determine $-E_a$ by determining the coefficient of a significant linear fit on measured $\ln(I)$ and $\frac{1}{k_BT}$. Through a significant linear fit ($R^2 > 0.99$) on $ln(I)$ at 0.2 V versus $\frac{1}{k_BT}$ at temperatures from 260 K to 340 K the activation energy was determined to be 0.37 eV. We can investigate whether a similar activation energy is associated with the high-bias regime, indicating a similar thermally activated process at both low and high bias.

At high bias the conductivity also increases with temperature, except for a sudden decrease in conductivity near 290 K which is visible in figure 4.9 in the sudden drop be-

tween the green and orange curve representing 280 K and 290 K. From figure 4.9b it becomes clear that the linearity of the I-V curves is also dependent on temperature. Finally, the hysteresis observed at 290 K disappears with increasing temperature as can be seen in the I-V curves associated with 290 K, 300 K and 310 K depicted in figure 4.9c.

In order to compare the activation energy at high-bias to low-bias we first need to confirm that there is still an exponential effect of temperature on conductivity. figure 4.10 shows this to be the case, albeit with a different offset below or above 290 K due to the sudden shift in conductivity. This means that a linear fit on $\ln(I)$ at 2 V versus $\frac{1}{k_B T}$ for all temperatures would not be significant. However, below 280 K and above 300 K two separate significant linear fits can be made, determining the activation energy for low ($T < 280$) and high ($T > 300K$) temperatures. Through a linear fit ($R^2 > 0.99$) on $\ln(I)$ at 2 V versus $\frac{1}{k_B T}$ at temperatures from 220 K to 280 K the activation energy was determined to be 0.38 eV, while a linear fit ($R^2 > 0.99$) using $\frac{1}{k_B T}$ at temperatures from 300 K to 340 K yields an activation energy of 0.36 eV. These values are very similar to the activation energy of 0.36 eV at low bias. However, in addition to the asymmetry within one I-V curve, there appears to be asymmetry in the activation energies at positive and negative high bias, with the activation energies at negative bias being higher than those found at positive bias. Through a linear fit ($R^2 > 0.99$) on $\ln(I)$ at -2 V versus $\frac{1}{k_B T}$ at temperatures from 220 K to 280 K the activation energy was determined to be 0.395 eV, while a linear fit (R^2>0.99) using $\frac{1}{k_B T}$ at temperatures from 300 K to 340 K yields an activation energy of 0.40 eV. As such, the activation energy was slightly higher at negative bias, but still quite similar to the low-bias activation energy.

The effect of temperature on I-V curves discussed so far is based on currents measured in vacuum in order to limit condensation due to cooling. Still, the vacuum conditions may affect the wire and in turn the I-V curves. We therefore repeated temperature measurements in ambient conditions. When comparing the I-V curve in ambient conditions in figure 4.11 to that of vacuum conditions in figure 4.7 the shape of both curves seems similar, although the magnitude of currents is lower (maximum current of 65 pA instead of 200 pA), despite a higher maximum bias (4 V instead of 2 V). The asymmetry and hysteresis are still present, although the hysteresis is less pronounced. Therefore we will still use mean values of currents for increasing and decreasing bias, unless otherwise specified. In addition we will compare currents up to 2 V with the earlier measurements performed in vacuum, and focus on differences between ambient and vacuum conditions.

In terms of temperature dependence the I-V curves measured in ambient conditions lacked certain features of the I-V curves measured in vacuum conditions. The I-V curves in figure 4.12 show no clear shift in conductivity near 290 K, and focusing on the hysteris of curves near room temperature figure 4.12c shows an opposite effect of temperature on hysteresis. In contrast to the measurements in vacuum, hysteresis now increased with temperature near 290 K, resulting in almost no hysteresis below 290 K and large hysteresis at 310 K (figure 4.12c).

The effect of temperature on conductivity could still be quantified using the Arrhenius plot in figure 4.13. There was still a linear relationship between $\ln(I)$ at 2 V versus $\frac{1}{k_B T}$ at temperatures from 220 K to 310 K, but this time without the need for a separate fit since there was no sudden shift. Through a linear fit ($R^2 > 0.95$) on $ln(I)$ at 2 V versus $\frac{1}{k_B T}$

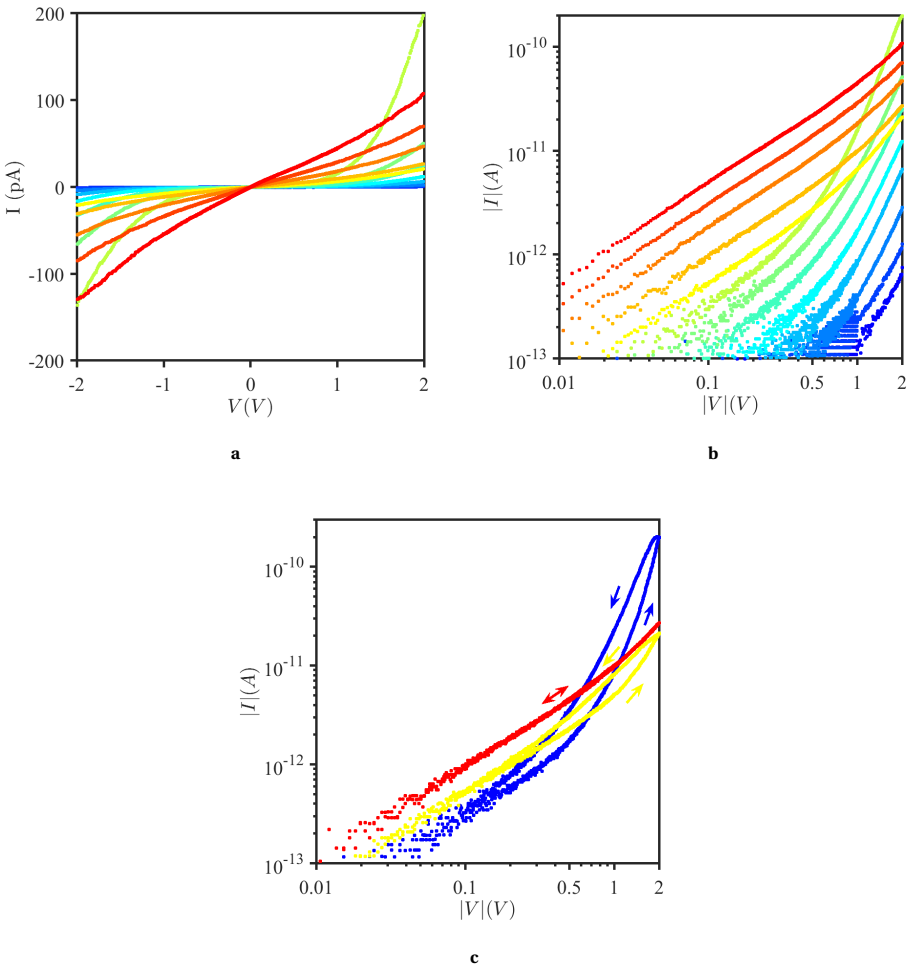

Figure 4.9: Mean current-voltage (I-V) curves of up to two sweeps per constant temperature for sample D for various temperatures on a linear scale (**a**) or log-log (**b**) scale. Measurements below 240 K and above 300 K consisted of one sweep, while other temperatures consisted of two sweeps. Conductivity increases with temperature up to 280 K and from 300 K, but there is a sudden decrease in conductivity near 290 K. The values reported in **b** only include values measured at positive bias. Linearity of I-V curves appears to be dependent on temperature. **c)** Mean current-voltage (I-V) curve of 1 sweep of sample D plotted on a log-log (**b**) scale for 290 K (blue) 300 K (yellow) and 310 K (red). Below 310 K at the same voltage the measured absolute current is higher at decreasing bias than at increasing bias, an effect called hysteresis. This hysteresis becomes less pronounced at 300 K, and disappears at 310 K. Arrows indicate direction of each color-associated curve, i.e. increasing or decreasing bias. A single two-headed arrow indicates that increasing and decreasing bias result in similar currents. I-V curves were measured in vacuum with constant temperature per sweep. One sweep goes from 0 V to 2 V, down to -2 V and back to 0 V. The connecting elements in sample D consisted of 2 wires. From blue to red temperature goes from 220 K to 340 K in steps of 10 K (blue representing cold, red representing hot).

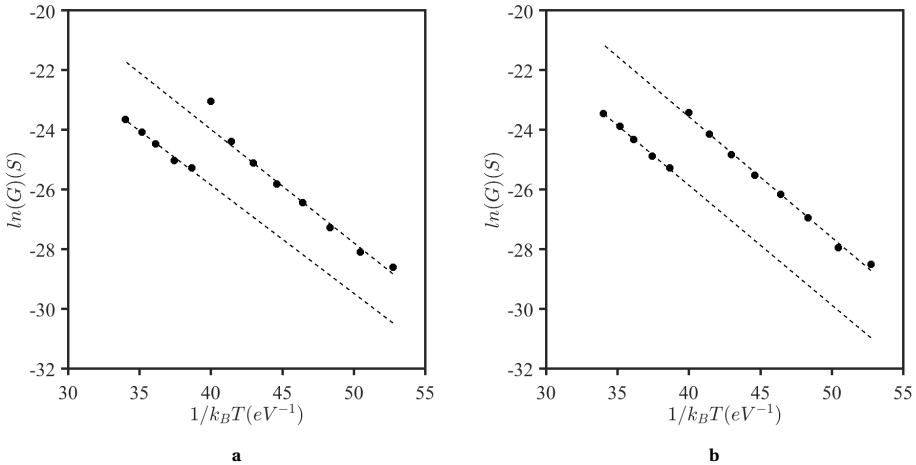

Figure 4.10: Arrhenius plot of conductance measured in vacuum at 2 V (**a** and -2 V (**b**) for temperatures from 220 K up to 340 K. In an Arrhenius plot the slope of a linear fit on the measurements corresponds to the activation energy. While there is a linear relationship both below 280 K and above 300 K, there is a sudden shift in conductance near 290 K. Fits were thus performed separately on the points below 280 K or above 300 K, i.e. above 41.3 eV^{-1} or below 38.8 eV^{-1}. At 2V (**a** above 300 K the activation energy was determined to be 0.36 eV, while below 280 K it was 0.38 eV. At -2V (**b**) above 300 K the activation energy was determined to be 0.40 eV, while below 280 K it was 0.39 eV. For all fits (dashed lines) $R^2 > 0.99$.

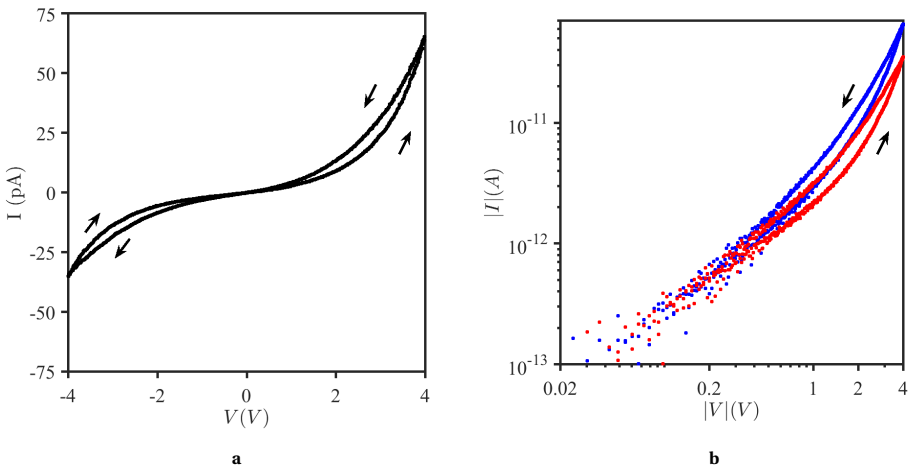

Figure 4.11: Mean current-voltage (I-V) curve of 1 sweep of sample D plotted on a linear (**a**) and log-log (**b**) scale. The connecting elements in Sample D consisted only of 1 wire. One sweep goes from 0 V to 4 V, down to -4 V and back to 0 V. I-V measurements were performed at room temperature in ambient conditions. At the same voltage the measured absolute current is higher at decreasing bias than at increasing bias, an effect called hysteresis. Arrows indicate direction of curve, i.e. increasing or decreasing bias. Measurements were performed at steps of 10 mV, with 100 ms between each step. In **b** blue and red indicate positive and negative bias respectively.

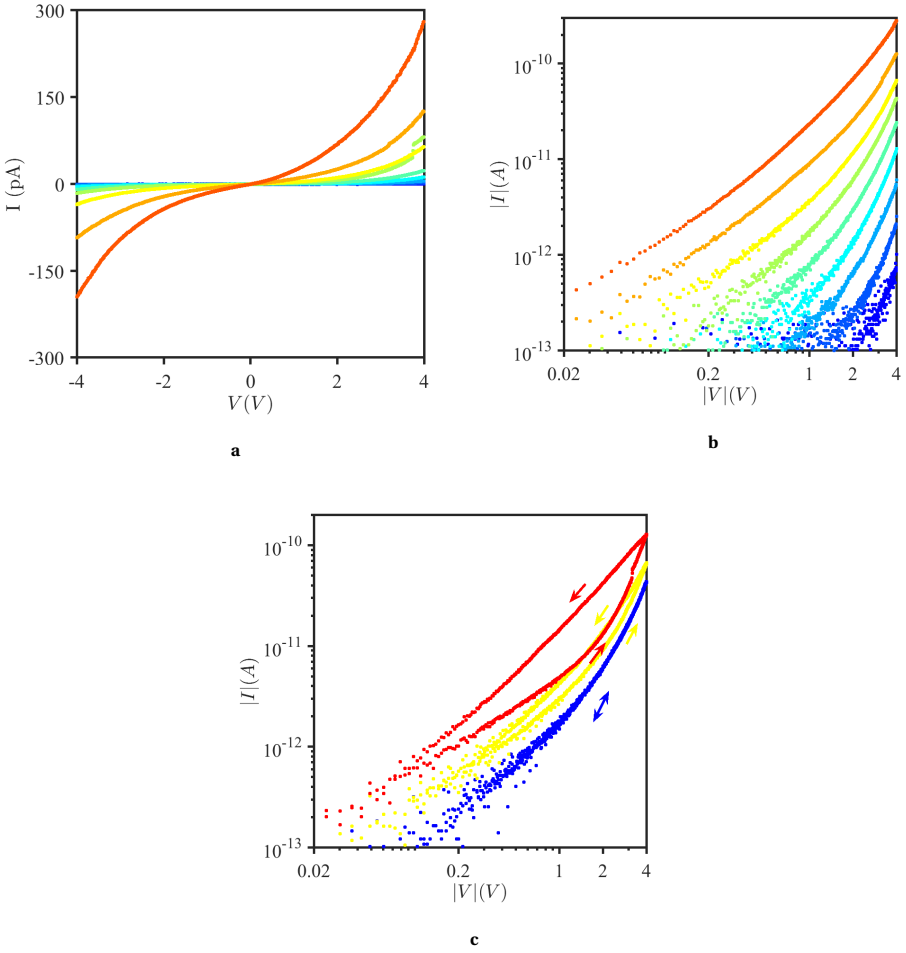

Figure 4.12: Mean current-voltage (I-V) curves of one or multiple sweeps per constant temperature for sample D for various temperatures plotted on a linear (**a**) or a log-log (**b**) scale. Conductivity increases with temperature. Measurements performed in ambient conditions lacked certain features of those performed under a vacuum: There is no sudden downward shift of conductivity near 290 K. I-V curves were similar for negative or positive bias (although for clarity the values reported in **b** only include values measured at positive bias). Linearity of I-V curves appears to be independent of temperature. **c)** Mean current-voltage (I-V) curve of 1 sweep of sample D plotted on a log-log (**b**) scale for 290 K (blue) 300 K (yellow) and 310 K (red). At 310 K at the same voltage the measured absolute current is higher at decreasing bias than at increasing bias, an effect called hysteresis. This hysteresis is much less pronounced at 290 K. Measurements at 220 K consisted of one sweep, while those above 230 K up to 290 K consisted of at least two sweeps, while other temperatures had more than two sweeps. I-V curves were measured in ambient conditions with constant temperature per sweep. One sweep goes from 0 V to 4 V, down to -4 V and back to 0 V. The connecting element in sample D consisted only of 1 connecting wire. From blue to red temperature goes from 220 K to 235 K to 250 K and then in steps of 10 K up to 310 K (blue representing cold, red representing hot). Arrows indicate direction of each color-associated curve, i.e. increasing or decreasing bias. A single two-headed arrow indicates that increasing and decreasing bias result in similar currents.

at temperatures from 220 K to 310 K the activation energy was determined to be 0.40 eV at 2 V, and 0.41 eV at -2 V. These values are similar to the negative high bias values found in vacuum.

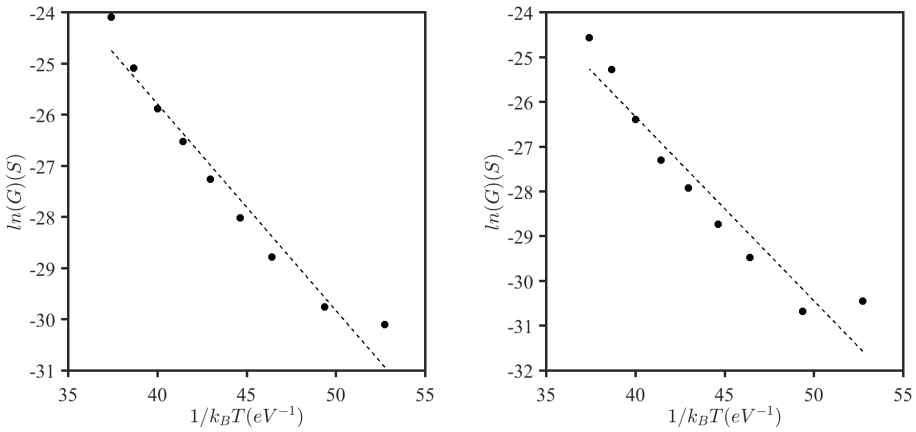

Figure 4.13: a) Arrhenius plot of conductance measured in ambient conditions at 2 V for temperatures from 220 K up to 310 K. In an Arrhenius plot the slope of a linear fit on the measurements corresponds to the activation energy. The activation energy was determined to be 0.40 eV, the fit (dashed line) had a $R^2 > 0.95$. At -2V (**b**) the activation energy was determined to be 0.41 eV, the fit (dashed line) had a $R^2 > 0.9$.

In summary, temperature was shown to have an exponential effect on conductivity. This effect was associated with activation energies from 0.36 up to 0.41, see table 4.1 for an overview. In vacuum, a sudden downward shift in conductivity occurs around room temperature, while in ambient conditions it does not. Additionally, increasing temperature above room temperature reduced hysteresis in vacuum, but increased it in ambient conditions. Having identified characteristic features of temperature dependence of conductivity, we then investigated field effects by applying a back-gate voltage.

Table 4.1: Activation energies as determined from Arrhenius plots of conductance at ±2 V of wire sample D at temperatures ranging from 220 K up to 340 K. Measurements were performed in vacuum or in ambient conditions. In vacuum a sudden shift in conductivity occurred near room temperature, therefore activation energies were determined below and above room temperature.

Activation energies (eV)			
	Vacuum		Ambient
	220 K < T < 290 K	300 K < T < 340 K	220 K < T < 310 K
+2 V	0.38	0.36	0.40
-2 V	0.39	0.40	0.41

BACK-GATE

The silicon chips used in this study contain a conductive inner layer which can be contacted as described in chapter 3. By applying a back-gate voltage we can investigate the effect of shifting the potential inside the wire with respect to the potential of the electrodes, and inspect whether the wires can be gated. We measured I-V curves of sample D while applying various back-gate voltages. figure 4.14a shows that with increasing absolute back-gate voltage in general the absolute current also increases, with the exceptions between 0 to -20 V for positive bias and 0 to 20 V for negative bias. The extent of this increase in current depends on whether the back-gate voltage has the same sign as the current. At positive bias applying a positive back-gate voltage has a stronger positive effect than applying a negative back-gate voltage and vice versa. The differing effects on positive and negative bias conductivity result in a change in asymmetry depending on back-gate voltage. This effect can be seen in figure 4.14a when the absolute current at 2 V (blue) are significantly different from those at -2 V (red). After performing power-law fits on positive and negative bias at various back-gate voltages it became clear that back-gate voltage also affects the linearity of I-V curves as depicted in figure 4.14b. At positive bias the exponential coefficient at a back-gate voltage of -60 V is close to 1, while a back-gate voltage of 60 V results in an exponential coefficient close to 2. For negative bias the opposite effect occurs, although the difference in exponential coefficient is less pronounced, with a coefficient close to 1.5 at a back-gate voltage of -60 V and close to 1 at a back-gate voltage of 60 V. In summary, applying a back-gate voltage increases current, and the effect is stronger if the bias is of equal sign. Additionally, or perhaps causally, the exponent of the power-law governing the I-V curves is affected by back-gate voltage.

Overall, we have identified that I-V curves are linear at low bias and non-linear at high bias, with conductivity and non-linearity varying between samples. Temperature has a positive effect on conductivity, except near room temperature in vacuum conditions. The effect of temperature is exponential and is associated with activation energies between 0.36 and 0.41 eV. Finally, back-gate voltage increases absolute current and non-linearity at equal-sign bias.

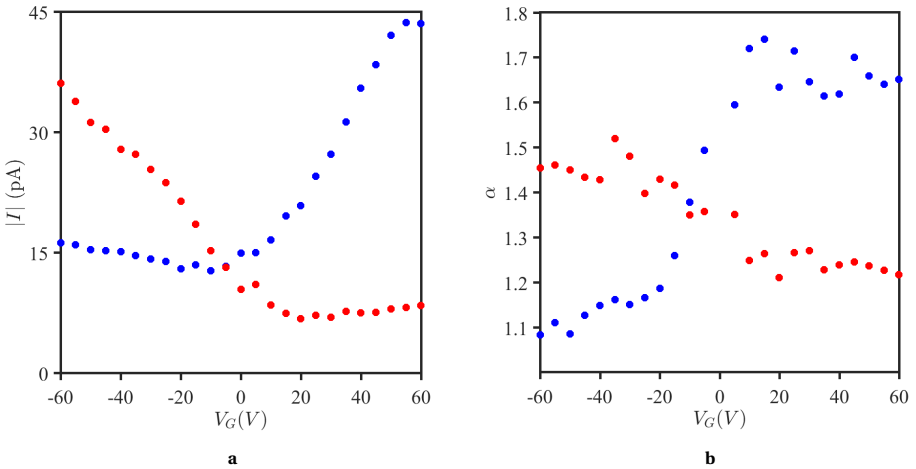

Figure 4.14: a) Absolute current through sample D at 2 V (blue) or -2 V (red) determined from the mean of one current-voltage sweep at various back-gate voltages measured in ambient conditions. Measurements were performed in sweeps starting at a back-gate voltage of 0 V and increasing in steps of 5 V up to 60 V, or decreasing from 0 V in steps of 5 V to -60 V. The connecting element in sample D consisted only of 1 connecting wire. With increasing absolute back-gate voltage the absolute current also increases, except between 0 to -20 V for positive bias and 0 to 20 V for negative bias. The extent of this increase depends on whether the back-gate voltage has the same sign as the current. **b**) The exponential coefficients for various back-gate voltages determined by a significant power-law fit at a bias of 2 V (blue) and -2 V (red). With increasing back-gate voltage the exponential coefficient increases, i.e. the current-voltage curves become increasingly non-linear.

4.4 DISCUSSION

We have investigated features of wire conductivity using direct contact measurements of single wires across a 500 nm gap. The first noticeable feature is that the magnitude of conductivity varies orders of magnitudes from sample to sample. This variation can be due to several factors, such as contact resistance, protein degradation, conformation of the wire, or different composition of the wires. In regards to the composition of the wires Filman *et al.*[8] recently showed that *G. sulfurreducens* produces two types of wires of similar dimensions. The first type are the pili (~3 nm wide), and the other type is a wire consisting of stacked cytochromes (~4 nm wide). We are unable to distinguish between these two types using our existing AFM images. This finding makes the protein structure context of existing studies on the charge transfer mechanism ambiguous. The varying magnitudes could thus also be due to a mixture of pili and cytochrome wires. Purification, or a closer look with non-invasive high-resolution microscopy techniques would be required to distinguish the two types of wires.

Furthermore we found that the overall shape of I-V curves are similar between wires. At low bias a linear bias dependency holds which then transitions to a non-linear dependency, with a typical cross-over voltage around 0.4 to 0.5 V, similar to the findings of Lampa-pastirk *et al.*[2].

The non-linear dependency follows a power-law with an exponent varying between 1.2 and 2.2. Lampa-Pastirk reported values of 1.9 and 2.45, leading to the conclusion of a quadratic dependency caused by a space-charge limited current (SCLC), with an exponent larger than 2 caused by more trap states. These values fall within the variation of our observations, though half of our values are below 1.8. Additionally, we observed various cases of asymmetrical charge transport. As such, SCLC seems insufficient to properly describe the electron transport. Either an expansion of the model, or an alternative model should be pursued.

TEMPERATURE DEPENDENCE

To aid in those pursuits we have identified some key features by measuring I-V curves at various temperatures. Most notably there is a positive correlation between conductivity and temperature, except in vacuum for a small region from 290 K to 300 K where the two have a strong negative correlation. The correlation between conductivity and temperature was also shown to be exponential, except for the sudden shift around 290 to 300 K.

This positive correlation is opposite to that determined by Ing *et al.*[4] using bipotentiostat measurements on spin-coated filaments in liquid, although it does correspond to the findings of Yates *et al.*[9] using live biofilms. One similarity is a change in conductivity near room temperature, although the nature of the change is quite different. Ing *et al.*[4] found a lower activation energy above room temperature, while we found a sudden drop in conductivity near room temperature in vacuum. Additionally, the shift in conductivity was absent in measurements under ambient conditions. The cause of this shift was not further investigated, but to speculate it might be that it is caused by a conformational shift of the wire correlated with temperature. In ambient conditions this shift may be allowed to occur gradually with negligible effects on conductivity rather than the sudden switch in conformation when in vacuum with drastic effects on conductivity.

The conductivity depends on temperature via an exponential relationship. Fits of Arrhenius plots result in activation energies at a bias of ±2 V from 0.36 eV up to 0.41 eV depending on measurements in vacuum or ambient conditions, positive or negative bias and above or below room temperature in vacuum (see table table 4.1 for an overview). This is quite different from the activation energy of 0.13 eV identified by Yates *et al.*[9] using biofilms. Due to the complex nature of biofilms compared to single wires it is difficult to speculate on the cause of this difference. A comparison to a similarly well-defined system as a single wire would be more appropriate.

CHARGE TRANSPORT MECHANISM

The positive exponential correlation with temperature helps to identify the charge transport mechanism. In the review by Creasey *et al.*[7] several current models for charge transport through protein nanowires are described. The models described are those for band transport in metals and semi-conductors, tunneling, superexchange, and multi-step hopping. Of those models only the semi-conductor and hopping models predict a positive exponential correlation between conductivity and temperature.

A semi-conductor model involves a valence and conduction band separated by a gap, with a band consisting of a number of states in which the wave function is spread across molecular orbitals along the wire. An electron in such a state is delocalized along the wire. It has been proposed that the helical configuration of aromatic amino acids inside of the pili provides the opportunity for delocalization along the wire. The probability of such a delocalization occuring along the aromatic amino acids is strongly dependent on aromatic amino acid distance. Depending on the model used for pilum structure the probability of this mode of transport varies from possible to extremely unlikely[7].

A discriminating feature of a semi-conductor is a large effect of back-gate voltage on conductivity. In our measurements the maximum effect of back-gate voltage was a near-tripling of current (from 15 pA to 42 pA) when increasing the back-gate ten-fold (from 5 to 50 V). In addition, the I-V curves became increasingly non-linear with increasing back-gate, if the sign of applied back-gate was the same as the current. To what extent this effect is due to changes in injection barrier (also addressed in the hopping model below) or due to changes in internal potentials of the wire would require further (theoretical) investigation. An alternative model is the hopping model, which we will explore here further.

ELECTRON TRANSPORT MODEL

To facilitate a qualitative discussion on our results we will first describe a simple electron transport model. In this model there are two key processes resulting in an exponential temperature dependence. We will discuss this model in the context of two limiting cases highlighting those key processes, each resulting in exponential temperature dependence as well as addressing certain features of our observations.

We consider a series of sites with no inherent potential differences between sites to represent the wire. The first and last site (contact sites) are in contact with electrodes. We will describe the electron transport in terms of rates, with current being proportional to the overall rate.

INJECTION BARRIERS

We consider the first case where the following holds: The sites maintain zero potential difference, i.e. they are always in resonance with each-other. For the electron transfer rate from site to site we take some constant value which is depicted in figure 4.15a as straight purple arrows. In the second case we will expand upon this with a more realistic rate. Additionally, the first and last site (contact sites) are separated from the electrodes by equal potential barriers that are higher in potential than the potential corresponding to the typical bias used in this study. Finally, there is a potential difference between the electrodes and contact sites, the injection barrier, depicted in figure 4.15a as ΔE_{inj}.

Electrons can tunnel through the potential barrier if they are in a state with chemical potential equal to the chemical potential of the contact site. The rate of electrons tunneling through this barrier is proportional to the probability of this state being occupied. The probability of this state being occupied by an electron in the electrode is in turn determined by the injection barrier and is proportional to $e^{-\frac{\Delta E_{\text{inj}}}{k_B T}}$.

Upon application of a negative bias the probability of that state being occupied by an electron will exponentially increase due to a shift in the Fermi distribution depicted in figure 4.15b. At the same time the introduction of a potential gradient will require that the gradient is divided amongst the contacts and the sites. Since in this case we assume that there is no change in potential between sites, the potential gradient must be divided amongst each of the contacts resulting in an upwards shift of the first site potential by half the applied bias. The probability of the state at the left electrode with equal potential as the first site being occupied by an electron is then proportional to $e^{-\frac{\Delta E_{\text{inj}} - \frac{eV}{2}}{k_B T}}$, resulting in exponential dependence of conductivity on bias and temperature.

Once the applied bias equals twice the injection barrier the electrode will be on resonance with the first contact site (see figure 4.15c). At that point conductivity will become independent of bias, and will no longer have an exponential dependence on temperature. As such, a regime change in conductivity dependence on bias and temperature is expected when the bias $eV \geqslant 2\Delta E_{\text{inj}}$. Above this injection barrier the effects of bias and temperature on conductivity are predominantly determined by the transfer process within the wire. In this case, that process does not have an exponential dependence on temperature or bias. Additionally, in this first case an asymmetry can be addressed via unequal injection barriers.

Applying a back-gate voltage will slightly heighten or lower the potential of sites within the wire with respect to the electrodes, based on the charge carriers (electrons or holes) and sign of the applied back-gate voltage. Applying a positive back-gate voltage will reduce the potential of electrons at each site, including those next to the electrodes, effectively lowering the barrier (see figure 4.16a). In the presence of an injection barrier, applying a back-gate voltage should then also increase conductivity exponentially.

HOPPING

In the second case we now assume that there are no potential or injection barriers between the electrodes and contact sites. On the other hand, the sites initially have equal energies but they are no longer necessarily in resonance with each-other. Rather, we consider the sites as redox sites, and now the rate for electron transfer within the wire is

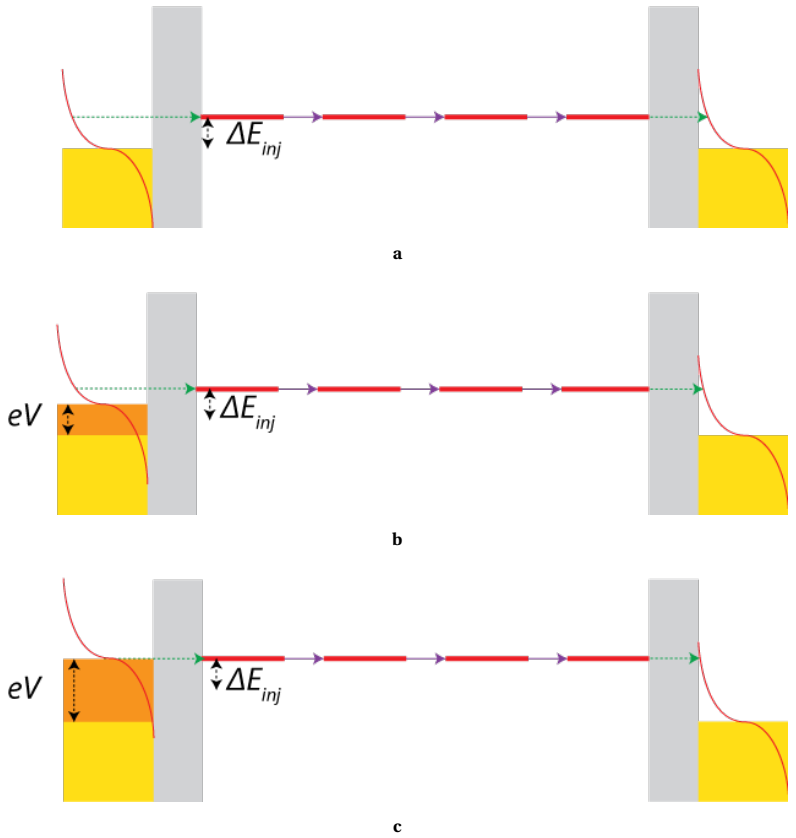

Figure 4.15: Schematic representation of a model in which injection barriers result in an exponential temperature dependence of conductivity. Height denotes chemical potential, width denotes distance, red horizontal lines are sites, gold/orange rectangles represent electrodes, right electrode chemical potential is fixed, illustration is not to scale. Solid arrows represents movement of electrons, dashed arrows represent tunneling through contact barrier or characteristic energy changes. Red line in electrode indicates the probability of a state with that potential being occupied by an electron (Fermi distribution). **a)** We consider a number of sites in resonance with each other, with potential barriers between electrodes and contact sites and an injection barrier to the first site (ΔE_{inj}). Electron transfer rate from site to site is considered constant, indicated by straight purple arrows. The potential barriers have a potential much larger than ΔE_{inj}. The probability of a state with equal potential as the first site being occupied by an electron is then proportional to $e^{-\frac{\Delta E_{\text{inj}}}{k_B T}}$. **b)** Upon application of a negative bias (eV) the potential of electrons in the left electrode will increase, shifting the Fermi distribution up and thus increasing the probability of a state with equal potential to the first site being occupied. Note that the gradient in potential will result in an upwards shift of site energy levels of eV/2. Electron transfer is proportional to $e^{-\frac{\Delta E_{\text{inj}}-\frac{eV}{2}}{k_B T}}$, thus resulting in an exponential dependence of conductivity on bias as well as temperature. Once across the barrier electrons move from site to site in a temperature and bias independent manner, until reaching the right barrier and subsequently the lower chemical potential in the right electrode. **c)** At a bias eV of twice the injection barrier the conductivity no longer depends exponentially on temperature, and the conductivity will depend linearly on bias. This is apparent as a regime change when $eV > 2\Delta E_{\text{inj}}$.

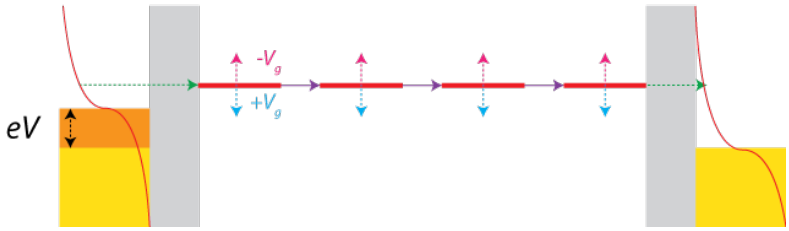

a

Figure 4.16: Schematic representation of the effect of back-gate voltage on the injection barrier described in figure 4.15. Height denotes chemical potential, width denotes distance, red horizontal lines are sites, gold/orange rectangles represent electrodes, right electrode chemical potential is fixed, illustration is not to scale. Solid arrows represents movement of electrons, dashed arrows represent characteristic changes in chemical potential. A back-gate voltage applies an electrical field within the wire with a positive or negative sign, shifting the chemical potential for electrons in the sites up or down. This shift in potential can increase or decrease the injection barrier, resulting in an exponential effect on conductivity. If there initially is no injection barrier, it can be introduced by the shift in energy levels.

determined by Marcus theory. When charge is transferred to a site, changes in atom organization due to the electric field of the charge will occur at and around the site where it transferred from and the site it transferred to. This change in organization is associated with a reorganization energy, depicted in figure 4.17a by ‡. In order for a charge to transfer from site to site it must therefore first be in a state with high enough potential to provide this reorganization energy upon transfer. The probability of an electron being in a state with that potential and hopping to the next site is proportional to $e^{-\frac{\Delta E_{\text{hop}}}{k_B T}}$, where $\Delta E_{\text{hop}} = \frac{(\lambda - \Delta E_n)^2}{4\lambda}$ and λ is the reorganization energy of the sites and ΔE_n is the potential difference between the sites. The rate of hopping $k_h op$, depicted in figure 4.17a as a curved purple arrow, is proportional to that probability. With no applied bias there is no potential difference between sites and then this relation simplifies to $\Delta E_{\text{hop}} = \frac{\lambda}{4}$.

Applying a bias will induce a gradient in potential, which in this second case will be divided across the sites rather than the contacts. This results in an energy difference between sites ΔE_n equal to $\frac{eV}{N-1}$ (see figure 4.17b), with N being the number of sites. This has two effects on the electron transfer rates within the wire. The first is that at thermal equilibrium, lower potential sites have a higher probability of being occupied than high potential sites. This difference in probability results in a net transfer rate which, when ΔE_n is much smaller than $k_B T$, depends linearly on applied bias. Note that this effect occurs regardless of a change in hopping rate. The second effect of the potential gradient is on the hopping rate itself, the $\frac{eV}{N-1}$ makes $\Delta E_{\text{hop}} = \frac{(\lambda - \frac{eV}{N-1})^2}{4\lambda}$ However, depending on the reorganization energy the effect of bias on the hopping rate can be negligible. The reorganization energy of stacked cytochromes was calculated to be around 1.2 eV. Taking into account a similar value, a low number of sites (500 sites, 1 every 1 nm) and our maximum bias (4 V), the effect of bias lowers ΔE_{hop} from 0.300 to 0.296 eV, a negligible effect. As such, the activation energy determined by Arrhenius plot will then still be approximately $\frac{\lambda}{4}$. At the same time, the rate is still proportional to $e^{-\frac{\Delta E_{\text{hop}}}{k_B T}}$, maintaining

an exponential dependence on temperature. Applying a back-gate voltage in this case would introduce an injection barrier similar to the one discussed in the first case.

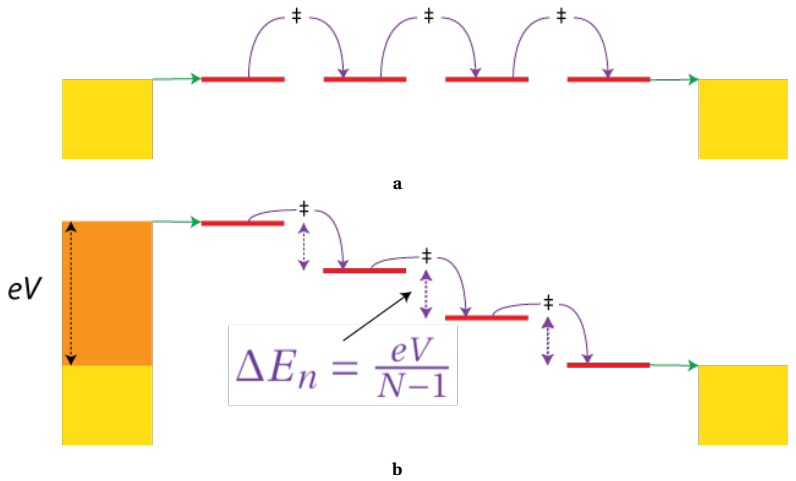

Figure 4.17: Schematic representation of a hopping model in which hopping rates as described by Marcus theory result in exponential temperature dependence of conductivity. Height denotes chemical potential, width denotes distance, red horizontal lines are redox sites, gold/orange rectangles represent electrodes, right electrode chemical potential is fixed, illustration is not to scale. Solid arrows represents movement of electrons, dashed arrows represent characteristic changes in chemical potential, ‡ represents transition state and associated reorganization energy. **a)** We consider a number of redox sites at resonance with the electrodes at the first and last site, and hopping only occurs between nearest-neighbor sites. According to Marcus theory for nearest-neighbor hopping the probability of an electron moving from redox site to redox site is proportional to $e^{-\frac{\Delta E_{\text{hop}}}{k_B T}}$, where $\Delta E_{\text{hop}} = \frac{\lambda}{4}$ with λ the reorganization energy of the site and its surroundings as a result from charge transfer. **b)** Upon application of a bias (eV) the potential of electrons in the left electrode will increase, imposing a gradient in chemical potential across the wire to the right electrode. This gradient is divided over each site. Electron transfer is still proportional to $e^{-\frac{\Delta E_{\text{hop}}}{k_B T}}$, but now $\Delta E_{\text{hop}} = \frac{(\lambda - \Delta E_n)^2}{4\lambda}$ with $\Delta E_n = \frac{eV}{N-1}$ where N is the number of sites. With large enough N the reorganization energy is dominant, thus resulting in an exponential dependence of hopping rate on temperature but negligible dependence on bias.

Qualitatively the first case addresses two features of our measurements: a regime change when the applied bias overcomes the injection barrier ($eV \geqslant 2\Delta E_{\text{inj}}$) and asymmetry due to differences in potential barrier at each contact. The second case addresses our observations at high bias where conductivity still depends exponentially on temperature.

Quantitatively in the first case the activation energy determined by Arrhenius plot should equal the injection barrier, and a regime change should occur at a bias of twice the injection barrier. The injection barrier determined via Arrhenius plot is around 0.4 eV. We see a regime change at a cross-over voltage around 0.45 eV, which would result in an injection barrier of 0.22 eV, nearly half of what was determined through the Arrhenius

plot. If we take the activation energy to be equal to the injection barrier, the applied bias would exceed the injection barrier in this first case at 0.8 V, i.e. in the high-bias regime. In the limits of the first case, where the exponential temperature dependence is solely due to an injection barrier, we should then not have been able to measure an activation energy at the high-bias regime, showing that this case does not fully hold.

In the second case the activation energy should be equal to a quarter of the reorganization energy. Since we find an activation energy around 0.4 eV, the reorganization energy would then be 1.6 eV. Such a high reorganization energy would mean that bias has a negligible effect on the hopping rate, and in this second limiting case the dependence on bias should then be linear throughout the measured bias range, which is not the case. As such, the second limiting case also does not fully hold.

However, each limit provides signature features of our measurements. A more realistic model in between these two limits combining the features of each could describe the observed features, depending on the injection barriers, contact barriers and reorganization energy. In future work a quantitative model should be employed to determine each of these parameters. Still, the model may also require further expansion to, for example, include disorder in site potentials.

PROTEIN STRUCTURE

Given the descriptive power of the hopping model we should consider the structural support for the presence of a series of redox sites. Electron transfer proteins typically use heme groups containing metal ions as redox sites. Pili lack these heme groups, and heme-containing cytochromes associated with the pili were shown to be too far apart to facilitate hopping[10]. However, Cordes *et al.*[11] showed that aromatic amino acids can function as "stepping stones", and Morita *et al.*[12] demonstrated hopping along the backbone of a peptide consisting of L-alanine and α-aminoisobutyric acid. Whether the associated electron transfer rates could facilitate efficient electron transfer across 500 nm remains to be investigated.

Notably, the cytochrome wires consist of stacked cytochromes that contain heme groups which would be the same kind of redox sites used in typical electron transfer proteins, and the stacked pattern of the heme groups could facilitate multi-step hopping. In such a cytochrome wire a hopping mechanism along the heme groups would seem more likely than a delocalization of electrons along the length of the wire. The activation energy of hopping along closely-packed cytochromes in *Shewanella oneidensis* structures was simulated to be around 0.3 eV by Breuer *et al.*[13]. This is close to our range of activation energies from 0.36 to 0.41 eV. These closely packed cytochromes were shown to be able to transfer electrons across long distances[13]. Since the measurements are consistent with hopping, with activation energies similar to other closely packed cytochromes and those cytochromes were shown to be capable of efficient long-distance electron transfer, it seems probable that the measured wires are in fact the cytochrome wires. However, upon deposition and inspection by AFM of samples of ΔpilA we did not see any filamentous structures. Since these mutants would still be expected to produce cytochrome wires, we would still expect to see filamentous structures. Further inspection of the identity of the wires via higher resolution imaging would be required for elucidation of wire identity, and the associated structural support for a hopping model.

BIOLOGICAL IMPLICATIONS

In biological context the low bias regime is most relevant. In this regime we have observed conductance up to 10^{-6} S, this corresponds to current of 200 nA at a bias of 0.2 V. A single cell produces [14] a current of 100 fA, three orders of magnitude lower. As such the conductivity of the wires is higher than required for a single cell. If the wire's conductivity is the result of adaptation, then the ability to conduct more than a single cell's current could imply a role in facilitating growth of multiple cells, i.e. the biofilm, as investigated in chapter 2. Alternatively, if cells are only in transient contact with electron acceptors, the high conductivity could facilitate immediate oxidation of all reduced cytochromes, where the cytochromes then serve as a "battery" [15].

Besides the magnitude of conductivity we observed effects of temperature and back-gate voltage on conductivity. The measurements of environmental effects were all performed at high bias, and as such its applicability to the biologically relevant low bias range remains to be investigated. We will base our discussion on an extrapolation of the observed effects to low bias.

We observed a positive dependence of conductivity on temperature, except when measuring in vacuum in a small temperature range where there was a strong negative temperature dependence. Notably, the temperature range for negative temperature dependence was around room temperature, a typical temperature for *G. sulfurreducens* growth [16]. If this effect is present in biological conditions a slight increase in temperature could severely limit charge transport in biofilms. Although this effect was not apparent in ambient conditions, it has been reported previously in conductivity measurements of wire networks by Malvankar *et al.* [3]. A strong negative temperature dependence of wire conductivity could be apparent in cell physiology in a strong temperature dependence of growth or regulation of genes related to metabolism and wire production. Indeed, *G. sulfurreducens* is known [17] to express wires even in the absence of iron-oxides when grown at 25° C but not at 30° C. Due to the broad effects of temperature on many aspects of microbial life, close investigation of this effect would be required to determine whether this regulation is due to the temperature dependence of conductivity, or another temperature-dependent process. If the single-wire conductivity in natural conditions lacks the negative temperature dependence, as seen in our measurements in ambient conditions, the reported negative temperature dependence in wire networks might be a consequence of wire-to-wire electron transport required for biofilm charge transport, an interaction between wire-to-wire transport and single-wire transport, or some other temperature-dependent process.

Finally, we saw a positive effect of back-gate voltage on conductivity, the extent of which depended on the sign of back-gate voltage and current. In a biological context variations in "back-gate voltage" are present in the form of changes in local electrochemical potential, for example due to the diffusion of a cation. The fluctuating local electrochemical potential could locally introduce or reduce disorder in the electrochemical potential of the sites inside the wire, in addition to the effects of temperature. In the cell's liquid environment filled with disorder due to Brownian motion and chemical and thermal interactions, a system tuned to use this disorder for a positive effect on conductivity would be beneficial, if high conductivity indeed has a positive effect on fitness. One could imagine a system where hopping rates are at times locally enhanced by the ran-

dom influx of a cation (decreasing local potential) and thermal variation, perhaps even resulting in short-distance delocalization as described in a "flickering resonance" model by Zhang *et al.*[18]. A positive effect of environmental coupling on particle transfer has theoretically been shown by Mohseni *et al.*[19] in the enhancement of exciton transfer by chromophoric complexes used in photosynthesis.

FUTURE WORK

We have provided characterization of a number of key features to be used in construction of a suited model for charge transport through bionanowires. Combining our data with that already published, especially the temperature-dependent density-of-states reported by Lampa-Pastirk, should allow for a deeper understanding of this fascinating new class of electron-transport proteins. In the future, confirmation of wire identity and combined measurements of back-gate and temperature variation, already within the capabilities of our current method, should allow for further specification of those models.

REFERENCES

[1] R. Y. Adhikari, N. S. Malvankar, M. T. Tuominen, and D. R. Lovley, *Conductivity of Individual Geobacter Pili,* Submitted **6**, 8354 (2015).

[2] S. Lampa-pastirk, J. P. Veazey, K. A. Walsh, G. T. Feliciano, R. J. Steidl, S. H. Tessmer, and G. Reguera, *Thermally activated charge transport in microbial protein nanowires,* Nature Publishing Group , 1 (2016).

[3] N. S. Malvankar, M. Vargas, K. P. Nevin, A. E. Franks, C. Leang, B.-C. Kim, K. Inoue, T. Mester, S. F. Covalla, J. P. Johnson, V. M. Rotello, M. T. Tuominen, and D. R. Lovley, *Tunable metallic-like conductivity in microbial nanowire networks.* Nature nanotechnology **6**, 573 (2011).

[4] N. L. Ing, T. D. Nusca, and A. I. Hochbaum, *Geobacter sulfurreducens pili support ohmic electronic conduction in aqueous solution,* Physical Chemistry Chemical Physics **19**, 21791 (2017).

[5] Snider, *Long-range electron transport in Geobacter sulfurreducens biofilms is redox gradient-driven Supporting Information,* Proceedings of the National Academy of Sciences of the United States of America **1**, 1 (2012).

[6] L. Robuschi, J. P. Tomba, G. D. Schrott, P. S. Bonanni, P. M. Desimone, and J. P. Busalmen, *Spectroscopic slicing to reveal internal redox gradients in electricity-producing biofilms.* Angewandte Chemie (International ed. in English) **52**, 925 (2013).

[7] R. C. Creasey, A. B. Mostert, T. A. Nguyen, B. Virdis, S. Freguia, and B. Laycock, *Microbial nanowires – Electron transport and the role of synthetic analogues,* Acta Biomaterialia (2018), 10.1016/j.actbio.2018.01.007.

[8] D. Filman, S. Marino, J. Ward, L. Yang, Z. Mester, E. Bullitt, D. Lovley, and M. Strauss, *Structure of a cytochrome-based bacterial nanowire,* bioRxiv , 492645 (2018).

[9] M. D. Yates, J. Golden, J. Roy, S. M. Strycharz-Glaven, S. Tsoi, J. Erickson, M. Y. El-Naggar, S. Calabrese Barton, and L. Tender, *Thermally Activated Long Range Electron Transport in Living Biofilms,* Phys. Chem. Chem. Phys. **17**, 32564 (2015).

[10] C. Leang, X. Qian, T. Mester, and D. R. Lovley, *Alignment of the c-type cytochrome OmcS along pili of Geobacter sulfurreducens.* Applied and environmental microbiology **76**, 4080 (2010).

[11] M. Cordes, A. Köttgen, C. Jasper, O. Jacques, H. Boudebous, and B. Giese, *Influence of amino acid side chains on long-distance electron transfer in peptides: Electron hopping via "stepping stones",* Angewandte Chemie - International Edition **47**, 3461 (2008).

[12] T. Morita, Y. Arikuma, H. Nakayama, and S. Kimura, *A helical peptide can mediate electron over 120 Å by hopping mechanism,* Technical Proceedings of the 2011 NSTI Nanotechnology Conference and Expo, NSTI-Nanotech 2011 **3**, 143 (2011).

[13] M. Breuer, K. M. Rosso, J. Blumberger, and J. N. Butt, *Multi-haem cytochromes in Shewanella oneidensis MR-1: Structures, functions and opportunities,* Journal of the Royal Society Interface **12** (2015), 10.1098/rsif.2014.1117.

[14] X. Jiang, J. Hu, E. R. Petersen, L. a. Fitzgerald, C. S. Jackan, A. M. Lieber, B. R. Ringeisen, C. M. Lieber, and J. C. Biffinger, *Probing single- to multi-cell level charge transport in Geobacter sulfurreducens DL-1.* Nature communications **4**, 2751 (2013).

[15] A. Esteve-Núñez, J. Sosnik, P. Visconti, and D. R. Lovley, *Fluorescent properties of c-type cytochromes reveal their potential role as an extracytoplasmic electron sink in Geobacter sulfurreducens.* Environmental microbiology **10**, 497 (2008).

[16] D. R. Lovley and E. J. Phillips, *Novel mode of microbial energy metabolism: organic carbon oxidation coupled to dissimilatory reduction of iron or manganese.* Applied and environmental microbiology **54**, 1472 (1988).

[17] G. Reguera, K. D. McCarthy, T. Mehta, J. S. Nicoll, M. T. Tuominen, and D. R. Lovley, *Extracellular electron transfer via microbial nanowires.* Nature **435**, 1098 (2005).

[18] Y. Zhang, C. Liu, A. Balaeff, S. S. Skourtis, and D. N. Beratan, *Biological charge transfer via flickering resonance,* Proceedings of the National Academy of Sciences **111**, 10049 (2014).

[19] M. Mohseni, P. Rebentrost, S. Lloyd, and A. Aspuru-Guzik, *Environment-assisted quantum walks in photosynthetic energy transfer,* Journal of Chemical Physics **129** (2008), 10.1063/1.3002335, arXiv:0805.2741 .

5

CONDUCTANCE OF CABLE BACTERIA

We demonstrate the flexibility of the wire deposition method by measuring a different type of conductive biological wire. Cable bacteria are able to facilitate electron transport along their cell membranes across several millimeters. We image successful deposition of cable bacteria bundles and measure their conductance. Current-voltage curves showed conductance in the orders of magnitude from 10^{-10} *S to* 10^{-7} *S.*

Chips manufactured by Jacqueline A. Labra Muñoz, cable bacteria samples provided by Filip Meysman and prepared by Silvia Hidalgo Martinez. Methods are reproduced from "A highly conductive fibre network enables centimetre-scale electron transport in multicellular cable bacteria." by F. Meysman, R. Cornelissen, S. Trashin, R. Bonné, S. Hidalgo Martinez, J. van der Veen, **C.J. Blom**, C. Karman, J. Hou, R.T. Eachambadi, J.S. Geelhoed, K. de Wael, H.J.E. Beaumont, B. Cleuren, R. Valcke, H.S.J. van der Zant, H.T.S. Boschker, J.V. Manca from 2019.

5.1 INTRODUCTION

With the discovery of conductive protein wires in *Geobacter sulfurreducens*[1], other systems known to employ long-range electron transport were reevaluated. The model organism *Shewanella oneidensis*[2] was shown to possess conductive cytochrome-packed membrane protrusions. *G. sulfurreducens* affiliated species such as *Geobacter metallireducens* and *Geobacter uraniireducens* also appear to possess conductive nanowires[3].

Of particular interest from an intercellular cooperation point of view are bacteria of the *Desulfobulbaceae* species, the so-called "cable bacteria". Bacteria of the *Desulfobulbaceae* species form centimeter-long filaments of cells, each connected at the poles to another cell. Their long filamentous assembly allows the cable bacteria to be exposed to aerobic environments on one end, and an anaerobic environment on the other. In marine sediments with *Desulfobulbaceae* species the reduction and oxidation of oxygen and sulfides was shown to be linked, while the oxygen is separated by several centimeters from the sulfides[4]. At the anaerobic end the cells facilitate the oxidation of dihydrogensulfide to sulfate, with no apparent terminal electron acceptor at that location in the sediment. On the other end of the filament oxygen is reduced to water, with no apparent electron donor.

The connection between oxygen reduction and sulfide oxidaton was ruled out to occur via diffusion of molecules[5] due to the rapid change in hydrogen sulfide concentration upon a sudden change in oxygen concentration, and instead there must then be some mechanism for transporting electrons through the filamentous bacteria across centimeter distances. Upon close inspection of cable morphology, cells were shown to possess membrane ridges. Electron micrographs showed fibres in each of the ridges, coalescing at the cell pole connection before seemingly crossing that barrier and continuing in the ridges of the next cell. The fibrous protein material was found to be conductive, although the protein structure is a topic of ongoing investigation. These cells appear to produce networks of conductive fibres crossing hundreds of cells to allow the growth of the entire cable. The hypothesized presence of an intra- and transcellular conductor lead the bacteria colloquially being termed 'cable bacteria'[6].

A direct measurement of conductance through these structures would provide conclusive evidence, but requires making direct electrical contact with the cable bacteria, or the fibrous structures within their membrane. Subsequent investigation of the electron transport mechanism through these structures would require the manipulation of bias, temperature, and back-gate voltage. Our method described in chapter 3 was shown to be able to make electrical contact with biological wires, and control environmental conditions. Although that method was developed for measuring nanoscopic wires across a 0.5 micron gap, it can also be used for measuring larger structures since the gap between pads is 100 micron. Cable bacteria spanning this gap can then be measured from pad to pad.

Here we describe the application of our method for measuring conductance of biological wires on these cable bacteria as a first step towards direct measurements of the fibrous material. At the same time we can use the Passive Voltage Contrast imaging (PVC) to investigate the ability of cells to dissipate charge and to image the location of conductive structures on or in the cell. Using these techniques we provided the first direct measurements of charge transport through cable bacteria. From these first measurements

a more detailed study by Meysman *et al.*[7] followed investigating the role of the fibrous structures in conductance. Here, we discuss the application of our method for the first conductivity measurements to highlight the wide applicability of the method for future exploration of direct long range charge transport in biology, including its Passive Voltage Contrast imaging.

5.2 METHODS

The methods for sample preparation and Passive Voltage Contrast Imaging were described earlier in Meysman *et al.*[7], and the method for current-voltage measurements was earlier described in chapter 3. Each are reproduced here from the original text for reference.

SAMPLE PREPARATION

Cable bacteria were enriched from surface marine sediment collected from a creek bed within the Rattekaai salt marsh, The Netherlands (51°26'21"N, 04°10'11"E). Sediment was sieved, homogenized, repacked into PVC core liner tubes (diameter 40 mm, height 100 mm), and incubated with overlying aerated artificial seawater (salinity 30, temperature 16 °C). When the sediment showed the distinct geochemical fingerprint of electrogenic sulfur oxidation, it was used for the retrieval of cable bacteria bundles. Bundles were gently pulled from the top sediment layer with a custom-made glass hook. Thiofilum flexile EJ2M-BT was obtained from the German Collection of Microorganisms and Cell cultures (DSMZ, Braunschweig, Germany) and cultured on agar-solidified nutrient-rich medium. After transfer to a drop of purified water (ISO 3696 Grade 1, MilliQ) on a glass microscope the cable bacteria or *T. flexile* were then deposited on the chip with predefined electrodes.

PASSIVE VOLTAGE CONTRAST IMAGING

In Passive Voltage Contrast (PVC) imaging with a positive ion beam causes the surface to be positively charged except for areas where an electron sink can remove that charge (i.e., a grounded area). As a result, the build-up of charge on the surface is inversely correlated to brightness when imaging with a Focused Ion Beam-Scanning Electron Microscope (FIB-SEM). The electron beam was operated at 30 kV with a current of 43 pA and an aperture of 45 µm, while the ion beam was operated at a current of 10 pA. Electrodes were grounded by applying carbon paint from the main pad to the back of the chip. The back of the chip is then in electrical contact with the steel Dual-Beam chamber, effectively grounding the main.

CURRENT-VOLTAGE MEASUREMENTS

All current-voltage (I-V) measurements were performed using a TTP4 Desert (LakeShore) Cryogenics probe station with mounted probes from Lakeshore ZN50R-CVT-25-BECU and ZN50R-25-BECU for varying or constant temperature measurements respectively. These probes were connected to a TU Delft IVVI rack containing custom electronics modules. Applied and measured voltages were set and read via a LabView interface controlling an Adwin II Gold Digital-Analog Converter. Before measuring across pads, a check for a proper connecting main electrode was performed by measuring the conductivity between two distant points along the lead (i.e., confirming a short circuit). Typical sweeps were performed up to ±2.0 V divided over $2^{16}-2$ points, at each point the current was determined as an average of 200 measurements. A delay of 400, 100 or 10 ms was used at each point before measuring for constant temperature, varying temperature and back-gate measurements respectively. In case clipping occurred, the gain was adjusted

appropriately. The measured currents display an offset in current at 0 V, i.e. the current is not zero at zero volts. Data was corrected for this by fitting a linear curve through the 20 points surrounding 0 V, and then substracting the value of the fit at 0 V from all points.

CONTRIBUTION

Filip J.R. Meysman supplied cable bacteria samples and Silvia Hidalgo Martinez washed and deposited the cable bacteria onto chips.

5.3 RESULTS

ELECTRICAL CONTACT

Upon initial investigation the order of magnitude of conductivity of cable bacteria was unknown. Therefore we used a chip design facilitating current measurements for both poorly and highly conductive organic materials. For deposition of the cable bacteria we used two chip designs consisting of gold probe contact platforms ("main pads") connected to a gold rectangular section (the "lead") flanked by another series of gold probe contact platforms ("side pads") each separated from another by 100 μm, a schematic depiction can be seen in figure 5.1. Depending on chip design the space between the side pads and the lead consists of a single 500 nm gap (termed "Design 1" in chapter 3), or a set of interdigitated electrodes (termed "Design 3" in chapter 3) each separated by a gap of 500 nm with one set connected to the side pad (the "side fingers") and the other connected to the main pad via the lead (the "main fingers"). The combination of a single large gap between side pads, and the small gap(s) on a single chip allows investigation of conductivity across several orders of magnitude.

Cable bacteria can be deposited both across the small gap between main and side pads, or across several side pads. Deposition across the small gap is best suited in case cable bacteria had a low conductivity, due to the potential for short distance connections increasing overall conductance. Especially when employing the interdigitated electrodes, deposition across the small gap allows for numerous short distance connections. Deposition across the side pads is best suited in case cable bacteria had a high conductivity, due to the large single gap resulting in a lower overall conductance. In case of deposition across the side pads the distance across which the conductance is measured can be adjusted by measuring across non-neighbouring side pads, i.e, when a single cable is crossing three pads and thus two gaps, one can measure conductance from the outer pads, effectively measuring across a distance of two gaps.

Finally, deposition across the side-to-main gap allows for easier investigation of the ability to dissipate charge using Passive Voltage Contrast (PVC) imaging. A detailed explanation of PVC imaging is described in chapter 3, in short one can visualize the ability to dissipate charge to a grounded main pad using a Focused Ion Beam where higher intensity indicates higher ability to dissipate charge. In practice it is easier to ground the main pad than the side pads, thus deposition resulting in a connection with the main pad (i.e. a deposition from side to main pad, crossing the gap) is desired for PVC imaging.

We first investigated whether an electrical connection was made upon deposition of cable bacteria. We carefully placed a bundle of cable bacteria across the set of electrodes

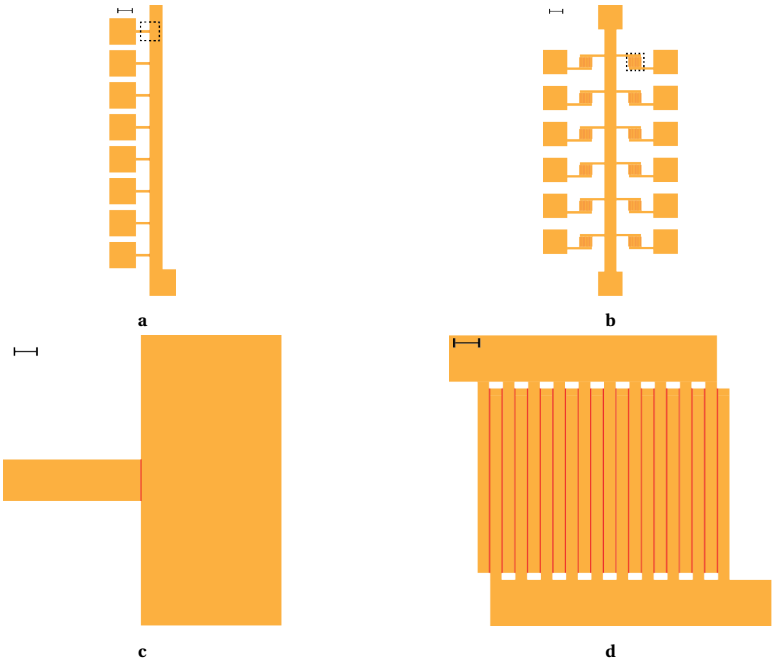

Figure 5.1: Schematics of chip designs employed for deposition of cable bacteria resulting in an electrical connection that can be contacted by probes in a probe station. Overall device architecture is depicted in **a** and **b** with gold depicted in yellow and the scale bars representing 100 μm. The design is identical to "Design 1" and "Design 3" in chapter 3. The areas indicated by the dashed squares is shown in more detail in **c** and **d** and contains a potential contact area consisting of a 500 nm gap indicated in red, with the scale bar representing 10 μm. When applying these designs for measuring cable bacteria the larger gap between pads can also be used as a potential contact area. In case the cable bacteria are highly conductive the larger distance will result in lower overall conductance, thus maintaining current levels within the detectable range at high bias (> 1 V).

comprising the main pad and side pads, as can be seen in figure 5.2. It was difficult to control the exact curve of the cables once dried, on occassion resulting in no cable-bridged gap. In the cases where a gap was crossed by the cable bacteria we used Scanning Electron Microscopy (SEM) to investigate how many cables were crossing gap. As a typical micrographs shown in figure 5.3b illustrates, it was possible to clearly see the cells bridging the gap, and to count the number of cables comprising the gap-crossing bundle, except for any cables intertwined at the bottom. The number of cables bridging the gap directly (i.e. near to the shortest path between pads) varied from 5 to 17, with some having an additional bundle of 2 to 6 cables crossing the same gap through an indirect route.

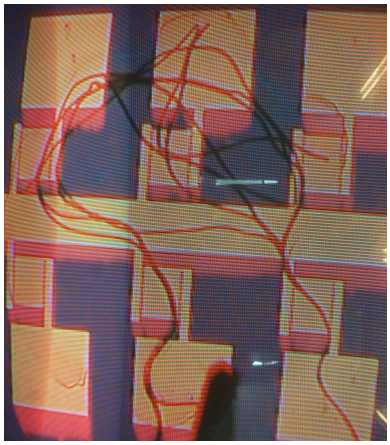

Figure 5.2: View of microscope output installed in probe station showing cable bacteria deposited on chips of Design 3 (see figure 5.1). Gold squares are contact pads connected to interdigitated electrodes which in turn are connected with the main gold lead in the middle. One gold pad is 200 by 200 µm and cable bacteria are several millimeters to centimeters long easily bridging the 100 µm gap between pads and one multicellular filament often crosses multiple pads. Conductivity was measured across neighboring pads resulting in measurements of the section of the cable bridging that particular gap. When one cable crossed several gaps, conductivity was measured for each, resulting in conductivity measurements for multiple sections of a single cable.

To check whether the cable bacteria deposition resulted in an electrical connection, without requiring above-noise current levels for probe station measurements, we investigated whether charge built-up through exposure to an ion beam was dissipated along the cables. The electrical connection was checked by depositing the cable bacteria across pads connected to a ground lead. As a control we used a different filamentous bacterium (*Thiofilum flexile*), not known to possess the ridges or fibrous material like the cable bacteria. When observing cable bacteria and the controls with PVC imaging we see a clear difference in charge dissipation in figure 5.4. The cable bacteria remain bright (i.e., do not accumulate charge) while *T. flexile* remain dark (i.e., do not dissipate charge). When imaging cells lying besides the pads, but still connected to them, we can see a repeating lining pattern of high brightness on the cells. The lining fits the typical distribution of the fibrous material, the high intensity could be due to the possibly conductive nature of the material. However, the ridges associated with the fibrous ma-

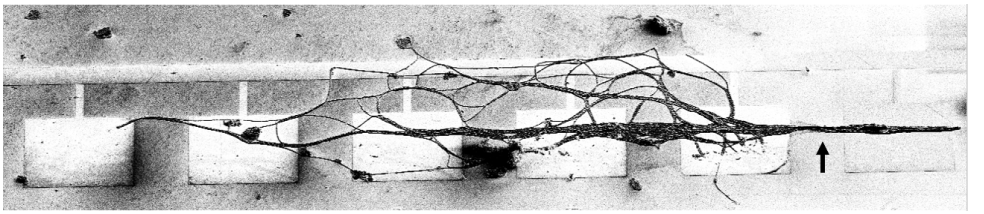

a

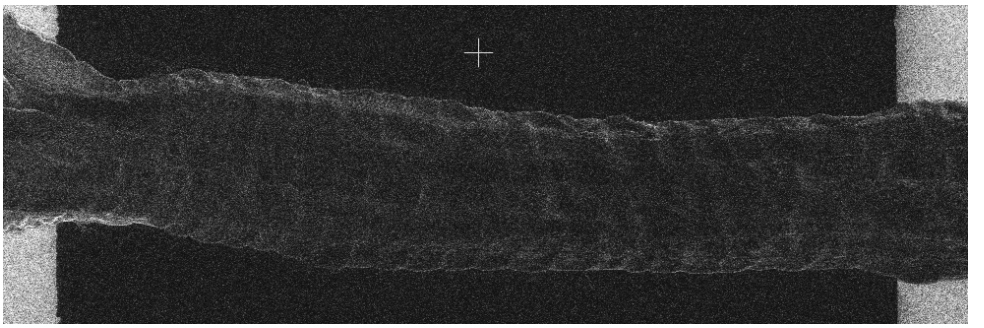

b

Figure 5.3: a Scanning Electron Micrograph of cable bacteria deposited across a set of pads (bright squares) of chip Design 1 (see figure 5.1). Image was taken at 45 °angle; general surface material is silicon-oxide while patterned bright areas are gold, pads are 200 by 200 µm and the gap between pads is 100 µm. Upon drying on the chip the multi-cellular filaments ("cables") tend to bundle together, at times resulting in multiple direct (shortest path between pads) or indirect connections between pads, with bundles splitting and joining between pads while some cables may bridge each of the gaps from leftmost to rightmost pad. Darkened area in center gap is due to intensive repeated Focused Ion Beam imaging of that particular area. **b** Bundle of cable bacteria crossing 100 µm gap indicated by arrow. Bright areas on the sides are gold, dark area is non-conductive silicon-oxide. The crossing bundle consists of multiple cables there appear to be 11 intertwining cables each with around 30 cells between gold pads. Conductivity measurements were performed on cable sections connecting neighboring pads.

terial may be due to topological artifacts typical for PVC which could also result in high intensity.

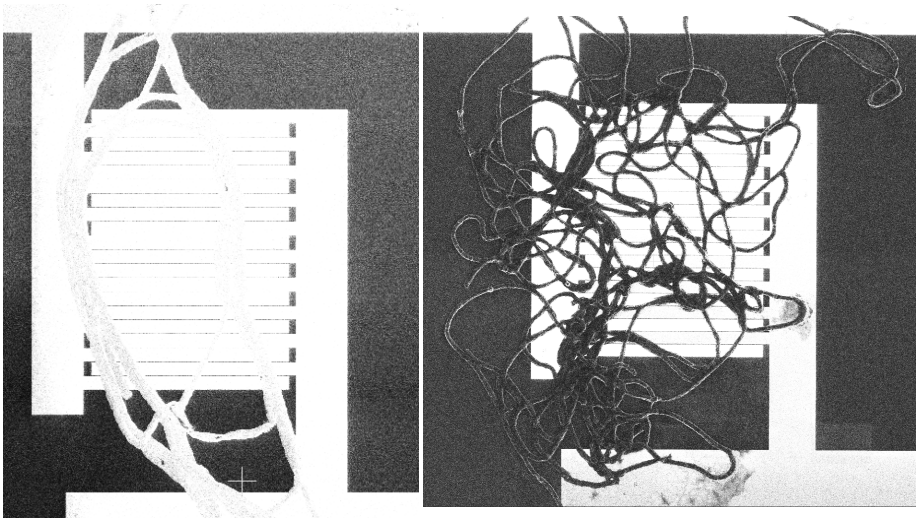

a b

Figure 5.4: Focused Ion Beam (FIB) Micrograph employing Passive Voltage Contrast (PVC) imaging of cable bacteria (**a**) and *Thiofilum flexile* (**b**) deposited on interdigitated electrodes connected to a main lead (top bright section) and contact pad (bottom bright section). One "finger" of the interdigitated electrodes is 80 µm long. In PVC imaging buildup of charge is visible as reduced intensity. The main lead is connected to a ground, allowing charge to rapidly dissipate. Material that is able to rapidly dissipate charge to the main lead will be brighter than material that slowly dissipates charge to the main lead. The cable bacteria possessing structural features hypothesized to contain conductive material are able to dissipate charge faster than *T. flexile* which does not have such structures.

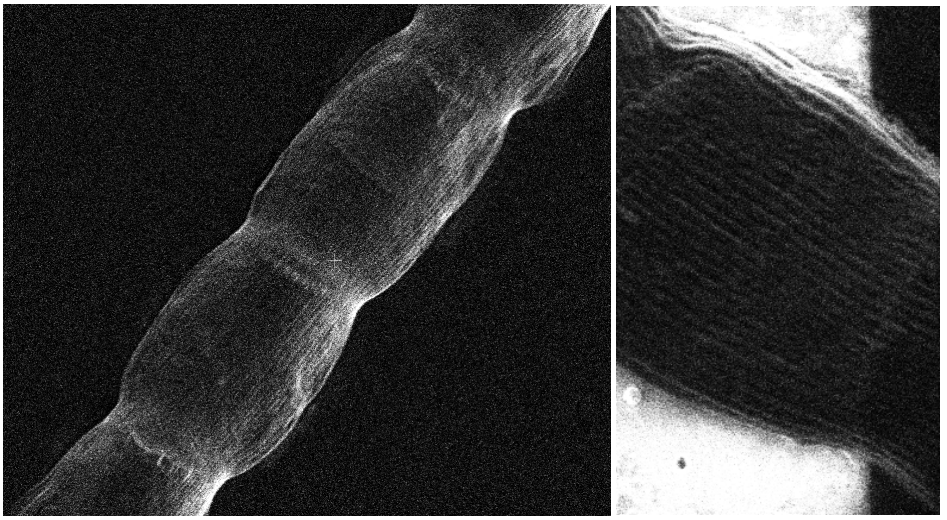

a b

Figure 5.5: a Focused Ion Beam (FIB) Micrograph employing Passive Voltage Contrast (PVC) imaging of cable bacteria cells connected to a grounded gold lead (out of view, general material surface is silicon-oxide). In PVC imaging buildup of charge is visible as reduced intensity. The lead is connected to a ground, allowing charge to rapidly dissipate. Material that is able to rapidly dissipate charge to the main lead will be brighter than material that slowly dissipates charge to the main lead. A lined pattern inside the cells as well as a dense pattern near the cell poles appears brighter than the rest of the cell. **b** A close-up of a cell in contact with gold (bright section) clearly showing the regular lined pattern. The lined pattern has similar spacing as the membrane ridges present in cable bacteria suspected to contain conductive material. However, the higher intensity could also be due to topological effects of the ridges, with protruding sections generally appearing brighter in PVC imaging.

CURRENT MEASUREMENTS

Given that the cable bacteria are at least capable of dissipating charge, we attempted to measure currents directly through the cable bacteria and *T. flexile*. Through use of a custom-made glass hook cable bacteria were extracted from soil samples, quickly washed, and immediately deposited on the chip. While rapidly drying the separate cables tended to bundle together. Upon drying, typically several minutes, we placed probes on each of the side pads connected by the bacteria and applied a bias sweep of ±2 V while measuring the current. For cables connecting multiple pads we measured each of the neighbouring pads connections.

Six pad-to-pad connections of cable bacteria were measured, three of which belonged to one deposited sample of cable bacteria (these connections were termed A1, A2 and A3), two to another (termed B1 and B2), and one to a third (termed C1). Of the controls, seven pad-pad connections were measured, belonging to three samples. At a bias of 2 V the cable bacteria conducted currents up to 375 nA while for controls the currents did not exceed noise levels.

Table 5.1: Overview of cable bacteria measurements. Each sample consists of cable bacteria filaments deposited across pads. Upon drying on the chip the multi-cellular filaments ("cables") tend to bundle together, at times resulting in multiple direct (shortest path between neighboring pads) or indirect connections between pads, with bundles splitting and joining between pads while some cables may bridge each of the gaps from leftmost to rightmost pad. The part of each bundle spanning two neighboring pads is termed a "section", and each crosses a 100 μm gap. E.g. in sample A the filaments crossed three gaps, and the first gap ("Section 1") was crossed directly via 12 cables and indirectly via 2 cables. Conductance was defined as the current divided by bias, at 2 Volt.

Sample	Section	Cables		Conductance at 2 Volt
		Direct	Indirect	(nS)
A	1	12	2	187
A	2	17	6	53
A	3	11	0	0.35
B	1	5	0	3.4
B	2	6	0	4.1
C	1	13	0	96

As is clear from table 5.1 we saw a large range in conductance of the various cable bacteria, ranging from 0.35 to 187 nS. Even within a single bundle the conductance could vary, with one pad-to-pad connection having a conductance two to three orders of magnitude higher than another (187 nS versus 0.35 nS for A1 and A3 respectively). In section 5.3 there appears to be no clear relationship between the conductance and the number of crossing cables. In contrast, the bias dependence was similar for each measured current-voltage (I-V) curve. In figure 5.7 a close-to-linear relationship between voltage and current can be seen for each of the cable bacteria, with little to no distinction between a low (<0.5 V) or high (>1 V) bias regime and no asymmetry.

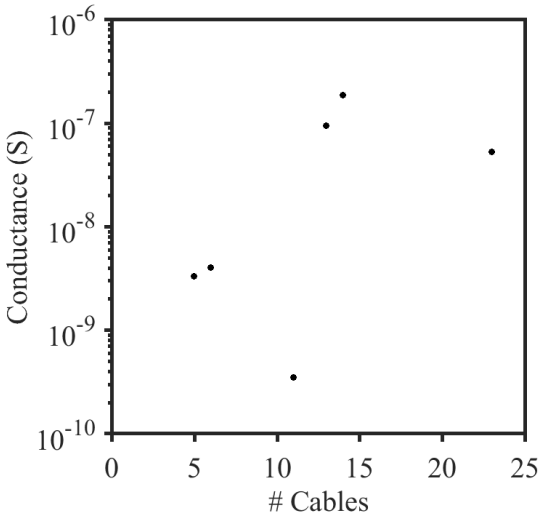

Figure 5.6: Relationship between the number of cables connecting neighboring pads and the measured conductance. One sample can result in multiple pairs of pads being connected, with a particular section of the cable bacteria crossing a particular gap (see figure 5.3). Of three samples (Sample A to C) the conductance for each section was measured. For sample A the sections consisted of 11, 14 or 23 cables respectively, sample B sections consisted of 5 or 6 cables respectively, and sample C had one section with 13 cables, resulting in six measurements. There does not appear to be a direct relationship between the number of cables in a section and its conductance. Conductance can vary between cable sections of the same sample, with the highest and lowest conductance both measured in sample A.

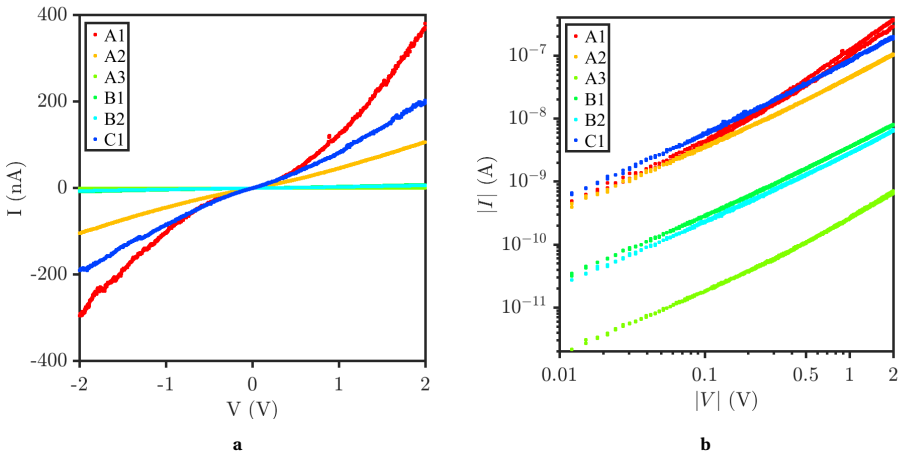

Figure 5.7: Current-Voltage (I-V) characteristics of cable bacteria measured across 100 µm gaps shown on a linear (**a**) or log-log (**b**, includes positive and negative bias measurements) scale. One sample can result in multiple pairs of pads being connected, with a particular section of the cable bacteria crossing a particular gap (see figure 5.3), with a sample indicated by letter and section indicated by number (A1 is section 1 of sample A). Although varying in magnitude, the I-V curve shape appears similar between samples and sections, i.e. the bias-dependence of conductivity appears consistent between measurements and seems close to linear and symmetrical.

5.4 DISCUSSION

We have shown that the method described in chapter 3 of this thesis can be applied to cable bacteria in order to measure conductance as well as identify charge dissipation. Using Passive Voltage Contrast (PVC) imaging we were able to show that cable bacteria were capable of faster charge dissipation than *T. flexile*. Upon imaging with PVC the cable bacteria deposited across electrodes remained bright, while *T. flexile* turned dark, indicating charge build-up on the cells. In addition, bright linear structures were visible within the cable bacteria cells, which seem to coincide with the ridges where the fibrous material is inside the cell, converging near the cell poles. Whether these ridges are bright due to artifacts of PVC or due to conductivity can not yet be determined. To the best of our knowledge, this is the first published application of this established semiconductor industry technique[8] in a biological context. For non-destructive in-depth characterization of charge dissipation other techniques such as Conductive Probe Atomic Force Microscopy (CP-AFM) or Scanning Tunneling Microscopy (STM) are powerful[9,10], but PVC imaging can provide quick qualitative differentiation. Any future investigation of a large number of filamentous bacteria for the presence of fast (relative to *T. flexile*) charge dissipation could start with a PVC imaging approach, before investigating each with CP-AFM or STM.

After confirmation of charge dissipation the cable bacteria were further investigated by measuring the electrical conductance between gold patches connected solely by cable bacteria and non-conductive SiO_2. The chips used for these measurements are the same as described in chapter 3, albeit applied in a different manner. From these measurements it became clear that the cable bacteria are conductive, with conductances up to 187 nS over length scales o 100 µm. Considering the typical cross-area of the fibrous material as imaged by[11] and using Òhm's law for conductivity ($\sigma = \frac{I}{V}\frac{L}{A}$, with I as current, V as applied bias, L the length of the gap, and A the cross-sectional surface area of the fibrous material) conductivities up to 8.8 mS/cm are found. However, there is a wide range in conductance, even within one bundle of cable bacteria. It is possible that the complex nature of the sample is responsible for this variation. The electrodes are in contact with the outside of the cell, and the material hypothesized to be responsible for conductance is in the periplasmic space. Charges would have to translocate through any extracellular material and the cell wall, twice, which may result in large variation in contact resistance. Additionally, the sample is drying while measuring, degradation or changes in conformation could also affect the conductance or contact resistance.

The presented measurements are a crucial first step towards characterization of the conductive structures in cable bacteria. Further steps involve the purification of the fibrous material, measuring the conductance through those fibres, and characterizing the conductance in a similar manner as the *G. sulfurreducens* wires in order to determine the electron transport mechanism. The method as applied here to cable bacteria can also be applied to the pure fibrous material. If the fibrous material consists of nanowires even its individual wires can be measured as described in chapter 3, showing the method's adaptability in scale useful for biological investigations. In fact, using the adapted method the fibres were shown to be conductive in Meysman *et al.*[7] with conductivities up to 79 S/cm.

With more and more types of electrically conductive biological wires being reported

ranging from membrane protrusions with high density of cytochromes [10], wires consisting of stacked cytochromes [12], pili without cytochromes [13] and trans-cellular fibrous material [7], the relevance of bionanoelectronics outside of neurology can be expected to increase in the future. The required combination of exact physical measurements with the variation inherent to biological investigations requires adaptable techniques. The method reported here has been shown to be adaptable for use with FIB, SEM, PVC imaging, allows for investigations using probe station measurements and can be expanded to use CP-AFM or STM and four-probe measurements, all on one sample. With the findings reported here, we have also shown it to be applicable across various length scales and biological structures, e.g. investigating a single polymer or a multiple cell filament. As such, this method provides a solid basis for future exploration of biological filamentous conductive materials.

REFERENCES

[1] N. S. Malvankar, M. Vargas, K. P. Nevin, A. E. Franks, C. Leang, B.-C. Kim, K. Inoue, T. Mester, S. F. Covalla, J. P. Johnson, V. M. Rotello, M. T. Tuominen, and D. R. Lovley, *Tunable metallic-like conductivity in microbial nanowire networks.* Nature nanotechnology **6**, 573 (2011).

[2] M. Y. El-Naggar, G. Wanger, K. M. Leung, T. D. Yuzvinsky, G. Southam, J. Yang, W. M. Lau, K. H. Nealson, and Y. a. Gorby, *Electrical transport along bacterial nanowires from Shewanella oneidensis MR-1.* Proceedings of the National Academy of Sciences of the United States of America **107**, 18127 (2010).

[3] Y. Tan, R. Y. Adhikari, N. S. Malvankar, J. E. Ward, K. P. Nevin, T. L. Woodard, J. A. Smith, O. L. Snoeyenbos-West, A. E. Franks, M. T. Tuominen, and D. R. Lovley, *The low conductivity of Geobacter uraniireducens pili suggests a diversity of extracellular electron transfer mechanisms in the genus geobacter,* Frontiers in Microbiology **7**, 1 (2016).

[4] L. P. Nielsen and N. Risgaard-Petersen, *Rethinking sediment biogeochemistry after the discovery of electric currents,* Annual Review of Marine Science **7**, 425 (2015).

[5] L. P. Nielsen, N. Risgaard-Petersen, H. Fossing, P. B. Christensen, and M. Sayama, *Electric currents couple spatially separated biogeochemical processes in marine sediment,* Nature **463**, 1071 (2010).

[6] C. Pfeffer, S. Larsen, J. Song, M. Dong, F. Besenbacher, R. L. Meyer, K. U. Kjeldsen, L. Schreiber, Y. a. Gorby, M. Y. El-Naggar, K. M. Leung, A. Schramm, N. Risgaard-Petersen, and L. P. Nielsen, *Filamentous bacteria transport electrons over centimetre distances.* Nature **491**, 218 (2012).

[7] F. J. Meysman, R. Cornelissen, S. Trashin, R. Bonné, S. H. Martinez, J. van der Veen, C. J. Blom, C. Karman, J. L. Hou, R. T. Eachambadi, J. S. Geelhoed, K. D. Wael, H. J. Beaumont, B. Cleuren, R. Valcke, H. S. van der Zant, H. T. Boschker, and J. V. Manca, *A highly conductive fibre network enables centimetre-scale electron transport in multicellular cable bacteria,* Nature Communications **10**, 1 (2019).

[8] R. Rosenkranz, *Failure localization with active and passive voltage contrast in FIB and SEM,* Journal of Materials Science: Materials in Electronics **22**, 1523 (2011).

[9] H. Tanaka and T. Kawai, *High-resolution scanning tunneling microscopy and dI/dV map studies of peptidenucleic acid and fluorescein isothiocyanate,* Applied Surface Science **252**, 5474 (2006).

[10] K. M. Leung, G. Wanger, M. Y. El-Naggar, Y. Gorby, G. Southam, W. M. Lau, and J. Yang, *Shewanella oneidensis MR-1 bacterial nanowires exhibit p-type, tunable electronic behavior.* Nano letters **13**, 2407 (2013).

[11] R. Cornelissen, A. Bøggild, R. Thiruvallur Eachambadi, R. I. Koning, A. Kremer, S. Hidalgo-Martinez, E.-M. Zetsche, L. R. Damgaard, R. Bonné, J. Drijkoningen, J. S. Geelhoed, T. Boesen, H. T. S. Boschker, R. Valcke, L. P. Nielsen, J. D'Haen, J. V. Manca,

and F. J. R. Meysman, *The Cell Envelope Structure of Cable Bacteria,* Frontiers in Microbiology **9** (2018), 10.3389/fmicb.2018.03044.

[12] D. R. Lovley and D. J. Walker, *Geobacter Protein Nanowires,* Frontiers in Microbiology **10** (2019), 10.3389/fmicb.2019.02078.

[13] N. S. Malvankar, M. Vargas, K. P. Nevin, A. E. Franks, C. Leang, B.-c. Kim, K. Inoue, T. Mester, S. F. Covalla, J. P. Johnson, M. Rotello, M. T. Tuominen, and D. R. Lovley, *Tunable metallic-like conductivity in microbial nanowire networks Supplementary figures,* Nature nanotechnology , 1 (2011).

6

Outlook

We have described methods for characterizing *G. sulfurreducens* microcolonies as well as *G. sulfurreducens* nanowire conductivity. Upon discovery of the nanowires the main focus lay on the mechanism of electron transport, possibly spurred by speculations of conductivity requiring a quantummechanical description. Lovley[1] even described the mechanism as similar to "metallic-like conductivity", i.e. delocalization of electrons along the entire length of the material. Maintaining identical energy levels and coherence along the entire length of a micrometer long flexible wire in an aqueous environment at room temperature is incredibly unlikely, if not impossible. In response, a superexchange model based on cytochromes[2] was proposed, ignoring evidence to the contrary[3]. This started a back-and-forth[4] with little middle ground between the predominant research groups Lovley and Tender.

In this thesis we have tried to provide an independent experimental characterization of nanowire conductivity. When compared to a simple model it seems hopping is a likely explanation, a phenomenon that can be described sufficiently by classical mechanics. Still, to explain observations of all literature, including conductivity in cytochrome denaturing conditions, requires a dedicated in-depth modelling approach by theoretical physicists. Such models may require combinations of classical and quantummechanical descriptions for a system with energy distributions varying in time. Biological systems are disordered and often ill-defined, applying quantummechanical models of well-defined ordered systems are unlikely to result in a fitting description but that does not disprove the relevance of quantummechanical phenomena in biology. Rebentrost *et al.*[5] has shown that environment induced decoherence can actually assist quantum transport, as seems to be the case in the photosynthesis protein chlorophyll. For electron transport Zhang *et al.*[6] have described a model incorporating varying energy distributions in a process called flickering resonance. Additionally, Ru *et al.*[7] have described a model of incoherent hopping between delocalized "islands" of closely stacked aromatic islands. Unfortunately both models do not seem sufficient to describe electron transport in *G. sulfurreducens* nanowires, but it is the type of modelling approach that is required to gain a deeper understanding of bionanophysics.

A deeper understanding of bionanophysics can then in turn provide deeper understanding of cells. Cells routinely mass-produce nanomachines (proteins) outperforming our most advanced synthetic nanomachines[8]. For their inner nanoscopic world quantummechanical phenomena should be as relevant as pressure, action potentials, and gravity are to our blood, nerves and bones. Especially when their survival depends on it.

To discover whether *G. sulfurreducens* survival indeed depends on the properties of its wires We have described a method for visualizing microcolony growth of strains with and without (poorly) conductive wires. In our exploratory investigation we tried to show microecological effects of conductive properties. Unfortunately definitive conclusions are limited due to problems in reproducibility. Future work may still describe to what extent a link exists between electrical contact with the wire network, the conductivity of wires, and survival. Such a connection would provide crucial context for understanding the relationship between nanowire protein structure and its conductivity. It may be that much higher conductivities are accessible to us in genetically modified wires, like reported by Tan *et al.*[9], but not to *G. sulfurreducens* due to limitations in the genotype-phenotype space. Their genotype-phenotype space may be so rugged that any single

mutation results in no conductivity at all. Especially if conductivity depends on electron delocalization any single change in energy level distribution within the protein structure may result in catastrophic failure of electron transport. Such a rugged genotype-phenotype space may also explain the higher-than-required conductivity, with a single all-or-nothing mutation resulting in high conductivity but without any possibility for tuning. Alternatively, conductivity may be tunable and the high conductivity is actually an evolved trait to support peripheral cells. According to evolutionary theory maintaining such an altruistic trait resulting in a public good (the wire network) would be no small feat. Processes such as kin or group selection are necessary to prevent loss of public goods traits to evolved cheaters that use but do not contribute to the public good[10]. Perhaps those processes have driven the evolution of an electron transport mechanism which is difficult to cheat, for example if hopping from cytochromes to the network is less efficient than wire-to-wire contact, benefiting mostly wire-producing cells. Regardless of speculation, it is clear that there are numerous outlying questions regarding nanowires and their role in biology. Some of the answers may require us to re-evaluate our understanding of biology in a broader scope, as evidenced in the discoveries of biological conductive filaments amongst other species[9,11,12].

Ultimately, the physics of the electron transport mechanism is likely to affect the *G. sulfurreducens* lifecycle, which affects its evolution. In turn, evolution would affect the protein structure which affects the electron transport mechanism. Future work on biological nanowires should thus not divorce their physics from their biological context, either for gaining understanding or for engineering. Biological nanowires hold promise for nano-electronics in a bio-based economy. Engineering efforts will be required to optimize them for such use, where biotechnology can provide tried-and-true approaches for engineering. Understanding of the biological context, such as provided by a future optimized method of the microcolony growth method described here, shall be required for such biotechnological approaches. The biological methods shall then have to be paired with the physical methods for quantification of the conductive properties of modified nanowires, such as the other method described in this thesis. Although for these methods the time of publication lies a decade after the start of their development, we hope and believe that they may still be useful in answering the many questions that remain.

REFERENCES

[1] D. R. Lovley, *Powering microbes with electricity: direct electron transfer from electrodes to microbes.* Environmental microbiology reports **3**, 27 (2011).

[2] D. R. Bond, S. M. Strycharz-Glaven, L. M. Tender, and C. I. Torres, *On electron transport through geobacter biofilms,* ChemSusChem **5**, 1099 (2012).

[3] N. S. Malvankar, M. T. Tuominen, and D. R. Lovley, *Biofilm conductivity is a decisive variable for high-current-density Geobacter sulfurreducens microbial fuel cells,* Energy & Environmental Science **5**, 5790 (2012).

[4] N. S. Malvankar, M. T. Tuominen, and D. R. Lovley, *Lack of cytochrome involvement in long-range electron transport through conductive biofilms and nanowires of Geobacter sulfurreducens,* Energy & Environmental Science **5**, 8651 (2012).

[5] P. Rebentrost, M. Mohseni, I. Kassal, S. Lloyd, and A. Aspuru-Guzik, *Environment-assisted quantum transport,* New Journal of Physics **11** (2009), 10.1088/1367-2630/11/3/033003, arXiv:0807.0929 .

[6] Y. Zhang, C. Liu, A. Balaeff, S. S. Skourtis, and D. N. Beratan, *Biological charge transfer via flickering resonance,* Proceedings of the National Academy of Sciences **111**, 10049 (2014).

[7] X. Ru, P. Zhang, and D. N. Beratan, *Assessing Possible Mechanisms of Micrometer-Scale Electron Transfer in Heme-Free Geobacter sulfurreducens Pili,* Journal of Physical Chemistry B **123**, 5035 (2019).

[8] H. Y. Wang and F. Dong, *A method for bubble volume calculating in vertical two-phase flow,* Journal of Physics: Conference Series **147**, 012018 (2009).

[9] Y. Tan, R. Y. Adhikari, N. S. Malvankar, J. E. Ward, K. P. Nevin, T. L. Woodard, J. A. Smith, O. L. Snoeyenbos-West, A. E. Franks, M. T. Tuominen, and D. R. Lovley, *The low conductivity of Geobacter uraniireducens pili suggests a diversity of extracellular electron transfer mechanisms in the genus geobacter,* Frontiers in Microbiology **7**, 1 (2016).

[10] S. A. Frank, *Microbial secretor-cheater dynamics,* Philosophical Transactions of the Royal Society B: Biological Sciences **365**, 2515 (2010).

[11] S. Pirbadian, S. E. Barchinger, K. M. Leung, H. S. Byun, Y. Jangir, R. a. Bouhenni, S. B. Reed, M. F. Romine, D. a. Saffarini, L. Shi, Y. a. Gorby, J. H. Golbeck, and M. Y. El-Naggar, *Shewanella oneidensis MR-1 nanowires are outer membrane and periplasmic extensions of the extracellular electron transport components,* Proceedings of the National Academy of Sciences , 1 (2014).

[12] F. J. Meysman, R. Cornelissen, S. Trashin, R. Bonné, S. H. Martinez, J. van der Veen, C. J. Blom, C. Karman, J. L. Hou, R. T. Eachambadi, J. S. Geelhoed, K. D. Wael, H. J. Beaumont, B. Cleuren, R. Valcke, H. S. van der Zant, H. T. Boschker, and J. V. Manca, *A highly conductive fibre network enables centimetre-scale electron transport in multicellular cable bacteria,* Nature Communications **10**, 1 (2019).

7

Acknowledgments

It is hard to believe that I am writing these final words of my PhD thesis. The journey here has made these words particularly hard to find. I will try to keep it short, and trust your own experiences to fill in the gaps.

Ferdinand, Yaroslav, Filip, and Martin, thank you for reading my thesis and independently approving my graduation. Up to the last moment I feared that for some reason it would not go through. Thank you for proving the fear false and acknowledging the worth of my work.

I would like to thank Nanofront for funding this research, and Bertus, Herre and Liedewij for supervising it. Bertus, my Master thesis work and the starting years of my PhD were the best years of my professional life, thanks in large part to you. We think very much alike, "we hebben dezelfde kronkel in ons brein", a rare occurrence for me. It was a delight to be understood and stimulated in a way that maximized my potential. I will cherish those times, and look forward to drink a beer together without the weight of professional context.

Herre, you have been there the whole way. Even after countless periods of radio silence you always welcomed me back with the same "Of course you can do this!" attitude. You opened your own office for me to work in where we discussed frequently about science and education. Your advice is consistent: "Keep it small, keep it simple, and just do [...]". A mantra counter to my nature and therefore especially important for me to return to. Without you, this thesis would never have been finished. Thank you for your support.

Liedewij, you joined at an opportune time. Your willingness to help provide clear feedback and set goals helped me return to a flow in writing. It gave me hope that I could finish the thesis and I found intrinsic motivation to write, two things I had thought long gone. Thank you for helping me with *de laatste loodjes*, they were a bit lighter now.

Cees, Marileen and Martin, thank you for chairing the department where I have greatly enjoyed working. The department is well run, thanks in no small part due to an especially good secretariat able to combine tip-top organization with flexibility.

All help is appreciated, but without some of you my work would have been physically impossible. Nandini Muthusubramanian and Jacqueline A. Labra Muñoz produced the microchips without which this work could not exist. Allard Katan, Anastasia Holovchenko and Johanna Miro have shown me the ropes regarding the AFM's, the probe station, and the SEM/FIB respectively, and Daniel helped me with work in the clean room. Erwin, you were the technician I hope my students become. Jochem, José, Niek, and Daan, thank you for your help and helping me realize that my future lies in education. Thank you all for your instructions, help, and patience.

I always felt at home in the Beaumont Lab though it was unfortunately a bit small. Thank you Luke, Thijs, Mike, Nicole, Alicia, Becca, Jochem and many others for adopting me into your labs and making me feel at home everywhere in BN.

Benjamin, Pauline, Magda and Wouter, in our self-proclaimed Executive Office we were best friends on the workfloor. Thank you so much for sharing your joy, sadness, fitness routines and gossip with me. Mathia, you hold a special place in our memories as such a unique inspiring force of good, I strive to be as you were.

Lisa. The nervous girl on a job application appearing in the doorframe of my FIB cellar room, suffering through my annoyance at the unexpected interruption. Knowing you now, how nerve-wracking that must have been for you. In The Executive Office we

drew closer during a difficult time in life. On our runs together, the single sport where I could actually beat you, you brightened my days with your unbridled joy at seeing a tiny lizard, goat, or bee. Your inexorable push forward is inspiring, your calm helps me come back down to earth, and your smile makes it all worth it. You are truly one-of-a-kind, and I am so lucky to have you.

Joost, from high school to study to PhD to returning to our home towns, you were always there. Always positive, always understanding, always supporting. I could stand by you at your PhD graduation, and now we can stand together once again. I am blessed to have you by my side.

Ab, Bart, Bart, Edgar, Iain, Jasper, Joris, Klaas, Lars, Rob en Vincent, a colorful group of friends turned second family. By now we have lived longer with than without eachother, our club itself can already drink, drive and vote. The 21-diners have been replaced with joint family walks, but the *lol* and *gezelligheid* remains the same. Thank you for all the good times all these years.

Esmee, samen zijn wij altijd weer grote zus en kleine broertje, bedankt voor het aarden. Dat gezegd hebbende, ik verwacht nu natuurlijk wel aangesproken te worden met *Dr.* ir. Blom junior.

Mama en Papa, jullie hebben mij hier naartoe gebracht. Met alle uitdagingen van dien, hebben jullie mij in staat gesteld om uitdagingen te overkomen. Jullie staan *altijd* achter mij. Ik heb zo'n geluk gehad om jullie als ouders te hebben. Dankje.